UNIVERSITÉ DE STRASBOURG

N° d'ordre :

École Doctorale Mathématiques, Sciences de l'Information et de l'Ingénieur

UdS – INSA – ENGEES

THÈSE

présentée pour obtenir le grade de

Docteur de l'Université de Strasbourg
Discipline : Électronique, Électrotechnique, Automatique
Spécialité Photonique

par

Mathieu GUILHEM

Conception et optimisation d'un capteur piezo-optique de pression, application à la mesure de hautes pressions hydrostatiques

Soutenue publiquement le 29 septembre 2010

Membres du jury

Directeur de thèse :	M. Patrick Meyrueis, Professeur, Université de Strasbourg
Rapporteur externe :	M. Alain Brun, Professeur, Institut d'Optique
Rapporteur externe :	M. Laurent Bigué, Professeur, Université de Haute Alsace

Laboratoire des Systèmes Photoniques **EA3426**

Conception and optimization of a piezo-optic pressure transducer
Application to high hydrostatic pressures sensing

Mathieu Guilhem

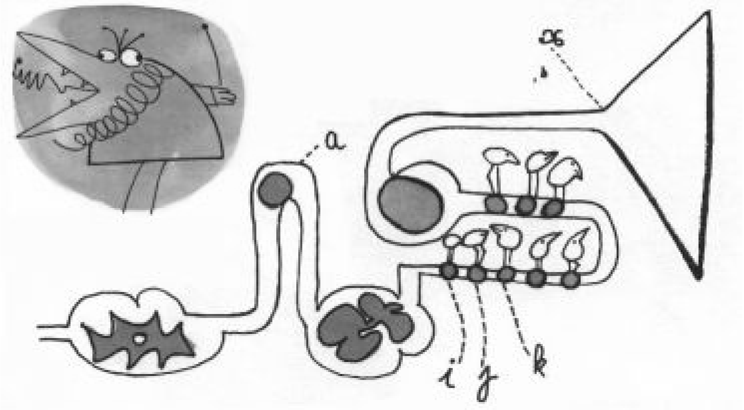

«Et pendant ce temps-là, les Shadoks pompaient. Et ils pompaient...»

... car il vaut mieux pomper d'arrache pied même s'il ne se passe rien que de risquer qu'il se passe quelque chose de pire en ne pompant pas.

Jacques Rouxel

Remerciements

Je remercie vivement Monsieur le Professeur Laurent Bigué de l'Université de Haute Alsace d'avoir accepté la double tache de président du jury et de rapporteur de cette thèse.

Je remercie Monsieur le Professeur Alain Brun de l'Institut d'Optique, également rapporteur, pour ses remarques pertinentes et ses conseils avisés.

Ces recherches ont été dirigées par Monsieur Ayoub Chakari qui a su me transmettre une partie de sa très grande expérience dans le domaine de la conception de capteurs optiques et de sa profonde connaissance des fibres optiques et de leurs applications. Je le remercie également pour ses conseils, ses encouragements et sa disponibilité.

Ce travail a été initié par Monsieur le Professeur Patrick Meyrueis, que je remercie pour son aide précieuse tout particulièrement lors de la phase finale de rédaction de ce mémoire.

Ce travail a été réalisé dans le cadre d'une collaboration CIFRE entre la société HYDAC GmbH et le Laboratoire des Systèmes Photoniques (LSP) de l'Université de Strasbourg. Je remercie ces deux entités ainsi que tout leur personnel pour le cadre de travail qu'elles m'ont fourni. Plus particulièrement, pour la société HYDAC, je remercie Messieurs Dan Curticapean et Horst Mannebach qui ont suivi mon travail avec attention.

Je remercie tous les membres du LSP qui ont contribués à une excellente ambiance de travail, et plus particulièrement Sylvain Lecler qui a partagé non seulement son bureau, mais surtout son tableau blanc avec moi.

Pour finir, je remercie tout particulièrement Patrice Twardowski et Yoshitate Takakura pour nos très nombreuses discussions, toujours stimulantes, dans des domaines aussi divers que variés, autour du thé de l'après-midi. Merci d'avoir partagé avec moi non seulement vos connaissances scientifiques mais également votre vision du monde.

Abstract

The measurement of pressure is a field that has been studied for centuries due to its important technological implications. Our goal is to propose an original method to measure high hydrostatic pressures using a low cost optical sensor.

A number of pressure sensors have been developed over the years, and the first part of this work presents an overview of the main ones. We then focus on optical pressure sensors, discuss the advantages and inconveniences of each method with regards to our constraints, and decide to develop the concept of a sensor based on the piezo-optic effect, i.e. the stress-induced birefringence in a transparent dielectric subjected to a force.

We presents the tools that will be used to modelize the piezo-optic pressure sensor: we first review the theory of polarization of light, from its physical origin to the Mueller-Stokes formalism; we then focus on the interaction of polarized light with matter: we discuss the theory of the piezo-optic effect and the polarization effects of total and partial reflections at an interface. Both effects are modelized in terms of their Mueller matrices.

We then propose an original concept for a pressure sensor, using an approach different from the one usually seen in polarimetric sensors. First the concept of a piezo-optic pressure sensor is presented where polarized light interacts with a dielectric material subjected to a pressure; the resulting state of polarization is analyzed by a second polarizer and a photodetector. Some aspects of the sensor are optimized while its shortcomings are listed. In light of this analysis we propose a revised concept to addresses these issues. The new proposal uses carefully oriented reflections to replace all polarizing elements, enabling simpler and cheaper production. We modelize this device, analyze its optical behavior, and then present the different sources of measurement error. Most of them are negligible, and we present methods to mitigate the influence of these that are not.

Part IV focuses on the experimental validation of the concepts presented so far. We describe the conception, calibration and validation of a Fourier Transform Mueller polarimeter that we intend to use to study the temperature dependence of the piezo-optic effect. We build a prototype based on the initial concept of the piezo-optic pressure sensor presented in Part III, and test its response to pressure. Its behaviour is found to be coherent with theoretical predictions, and these measurement serve to validate the concept of the sensor that was developed during this work.

Résumé

La mesure de pression est un domaine vieux de plusieurs siècles, dont le développement a été motivé par l'importance de ses applications technologiques. Le but de ce travail est de proposer une technique de mesure de fortes pression hydrostatiques par capteur optique à bas coût.

De nombreux types de capteurs de pression ont été développés au cours du temps, et la première partie de ce document présente une vue d'ensemble du domaine. Nous nous concentrons ensuite sur les techniques optiques et présentons leurs avantages et inconvénients. Au vu de notre cahier des charges, nous choisissons de développer un capteur de pression basé sur l'effet piezo-optique, c'est à dire l'apparition d'une biréfringence dans un matériau diélectrique soumis à une force extérieure.

La Partie II du mémoire présente les différents outils qui seront par la suite utilisés pour modéliser le capteur proposé : tout d'abord nous rappelons les détails de la théorie de la polarisation, son origine physique ainsi que le formalisme de Mueller-Stokes. Nous nous intéressons ensuite aux interactions entre une lumière polarisée et un milieu diélectrique, en présentant l'effet piezo-optique ainsi que les effets polarisant des réflexions à une interface. Les effets présentés sont modélisés par leur matrice de Mueller afin de simplifier l'étude à suivre.

Dans la Partie III nous proposons un concept original de capteur de pression, utilisant une approche novatrice par rapport à celle usuellement mise en oeuvre. Le capteur proposé est basé sur l'analyse d'une lumière dont la polarisation est modifiée par la traversée d'un milieu diélectrique rendu biréfringent par la pression à mesurer. Certains aspects du capteur sont optimisés, et ses inconvénients discutés. Cette étude aboutit à la proposition d'un capteur dans lequel les éléments polarisant discrets ont été remplacés par des réflexions successives. Ce nouveau concept est modélisé, puis nous présentons les différentes sources potentielles d'erreur de mesure et proposons des solutions pour compenser celles qui prédominent.

La Partie IV présente la validation expérimentale des concepts précédents. Nous décrivons la conception, la calibration et la validation d'un polarimètre de Mueller par Transformée de Fourier, conçu dans le but d'étudier la dépendance de l'effet piezo-optique à la température. Ensuite nous présentons la réalisation d'un démonstrateur de capteur piezo-optique de pression. Les essais effectués sont en accord avec les prédictions théoriques et valident donc le principe du capteur développé au cours de ce travail.

Contents

List of Figures

General Introduction

Optical sensors have enjoyed an increased success in the industry for the past years, mainly due to the newfound popularity and availability of compact, reliable and affordable light sources: Light Emitting Diodes (LEDs), Laser Diodes and more recently Vertical Cavity Surface Emission Lasers (VCSELs). Optical technologies are now heavily in use in various fields such as data transfer (from a simple infrared TV remote control to optical fibers, the backbone of modern telecommunications), information storage (CD-ROM, DVD-ROM, etc) or high-end metrology systems, but much less so in low-cost mass-produced measurement systems. For these applications, their electronic counterparts are usually preferred as they are based on well known and tried technologies that have been in use for many years. As a result these components are cheaper, the production techniques are well tuned and the initial research and development cost very low. The mass production of optical measurement devices is a younger field, and as a result the components are often more expensive and the initial R&D time and cost more important. Optical techniques are also usually harder to mass produce for base performances often similar to these of electronic sensors. On the other hand they do have all the advantages usually associated with optics: they are insensitive to electric and magnetic fields, which makes them particularly suited for harsh environments, and they have the potential to reach precisions and sensitivity far beyond what is accessible to conventional electronic sensors. Keeping these facts in mind, it is important for a company that aims to be at the vanguard of its field of competence to acquire knowledge and know-how in optical sensing methods, methods that will no doubt take an important place in sensor technologies in the years to come.

It is in this global context that HYDAC, an international company specialized in fluid technology, is looking into the technical and commercial feasibility of optical techniques to measure hydraulic pressures. With this goal in mind HYDAC has come to be in contact with the Photonics Systems Laboratory (Laboratoire des Systèmes Photoniques : LSP) and its years-long know-how in optical sensor, and in particular in optical fiber sensors and other integrated devices to optically measure pressure, temperature, electric and magnetic fields or acoustic and seismic vibrations [1, 2, 3, 4, 5, 6, 7, 8, 9, 10, 11]. The LSP takes particular care in its numerous collaborations with its industrial partners to respond to the usual preconceptions that optical sensors are more fragile, more expensive and overall harder to use outside of research laboratories. It is this base of knowledge and know-how that has been the foundations on top of which the following work has been conducted.

Part I of this thesis presents the state of the art in the field of high quasi-static pressure sensing. The different technologies commercially used in the measurement of hydraulic pressures are described and their performances are assessed in Chapter 1. Chapter 2 focuses on the optical methods suitable to measure hydraulic pressures. The main methods found in the scientific literature are presented and compared. Finally, in Chapter 3, after listing the more specific characteristics of sensors as required by HYDAC, we analyze the different existing possibilities and come to the conclusion that none is exactly suitable to fulfill the required specifications. Based on the imposed constraints we propose a novel concept for a piezo-optic pressure sensor.

The sensor technology that we propose to develop is a polarimetric sensor based on the piezo-optic effect[1]: when an uniform and isotropic dielectric is subjected to pressure, its index of refraction changes. If the pressure is anisotropic, the refractive index in the material will in general also be anisotropic.

As polarized light passes through a transparent material, its state of polarization can change depending on the distribution of the index of refraction in the material. If the index is uniformly distributed as well as isotropic, the polarization state remains unchanged; if it is not uniform, light will not in general propagate in straight lines (this case is not considered here); finally if the material presents an uniform but anisotropic index

---

[1] also known as the *elasto-optic* or the *photoelastic* effect

of refraction a ray of light will propagate in different ways depending on its initial state of polarization, and this state can evolve during propagation.

Based on this effect, the sensing method that we propose is implemented as follows: light in a known state of polarization is sent through a transparent material subjected to the pressure to be measured; the resulting state of polarization is measured at the output, and from its evolution the pressure applied to the material is determined. Over the course of this document, we will expand on this basic idea and we will study every aspects of the resulting setup in detail.

In Part II of this document, we present the theoretical tools that are useful to understand and modelize the proposed piezo-optic sensor. In Chapter 4 we review the classical theory of polarization as well as the usual theoretical tools used in the literature: we present the polarization ellipse as a graphical representation of polarization, then the Stokes polarization parameters and the Mueller matrices as useful tools to perform polarization calculations.

Chapter 5 focuses on the interaction of polarized light with transparent dielectrics. We discuss the piezo-optic effect, and the special case of the evolution of polarization when light is reflected and refracted at an interface is studied in details.

Part III focuses on the conception of the piezo-optic sensor. Chapter 6 presents the basic concepts and methods behind the sensor as well as the constraints it will be subjected to. With each of these constraints the concept is refined and we reach a final design that addresses all of them in an unified concept.

In Chapter 7 the proposed design is modelized and analyzed using the tools presented in Part II. Particular care is taken to study the potential sources errors and their effect on the measured pressure. All the identified sources of measurement uncertainties are combined and an estimation of the performances of the sensor is given.

Part IV presents the experimental verification of the models developed in Part III and validates the concept of a piezo-optic pressure sensor. We begin by a detailed explanation of the principle, building methods and calibration procedures of the tool used to measure the response to polarized light of various experimental setups: a Fourier-Transform Mueller Polarimeter.

The polarimeter it is tested on a well-known sample to validate its performances.

Finally a prototype version of the sensor is put together and tested, its readings matched against the predicted theoretical performances.

Part I

Pressure sensing: an overview

Introduction

The first application of pressure measurement devices has historically been atmospheric pressure sensing, with the development in 1643 of the mercury level barometer by Evangelista Torricelli [12, 13, 14]. This device has also been used in the study of gases from a purely scientific perspective, leading to the well known perfect gases relationship between pressure and temperature [15]. From these two developments are derived the main modern uses of pressure sensors: meteorology and control. Pressure sensor are widely present in the industrial world as monitoring devices: they provide a simple readable value that allows one to know if for instance a tank is filling properly, or if a fluid is correctly flowing inside a pipe. They also serve as warning and diagnostic devices: a sudden drop in pressure can indicate a serious problem with an hydraulic system, such as a leak, or a dangerous build up in gas pressure that may result in an explosion. After being purely passive control devices for years, pressure sensors have now become active parts of wider automated systems. These transducers provide a necessary feedback for automated processes that are regulated in real time[2].

Pressure sensors consist in one or several *transducers*, elements that transform one physical quantity into another. In the case of pressure sensors the primary transducers are of course pressure or force transducer: they transform a pressure or a force into a different physical quantity such as a mechanical, optical, or electrical signal that can be read at the output of the sensor.

There are several technologies used in industrial settings, the most common being based on the piezo-resistive effect. This technology allows for low-cost compact sensors with a typical accuracy around one percent of the full measurement scale. Other methods to measure pressure exist, most of them based on either electrical or mechanical effects. In this first part of the

---

[2] A common example is the pressure control in automotive fuel injection.

report we present a state of the art of the pressure sensing techniques used in commercial devices, before focusing on the purely optical methods that exist mainly in the scientific literature. We then describe the technological and industrial constraints imposed by the market on the sensor Hydac aims to develop, and conclude on the validity of the different existing technologies. We then propose a concept for a new optical pressure sensor that fits within the scope of the problem statement.

Chapter 1

Background : commercial pressure sensors

In this chapter we present the few technologies used by the vast majority of commercially available pressure sensors. For each of them we give a brief description of its principle, advantages, drawbacks, typical performances and finally fields of application.

1.1 Hydrostatic transducers

Hydrostatic transducers find the mechanical equilibrium between the force due to the pressure being measured and a known force, itself usually created by either a known pressure reference or by a known weight.

1.1.1 Liquid column

The liquid column manometer is likely to be the first pressure measurement device ever invented. In its simplest form it consists of a vertical column containing a liquid, both ends of the column being exposed to two different pressures; the liquid will move inside the tube until its weight is in equilibrium with the differential pressure to be measured [16, pp. 5-25][17, pp. 4.01-04]. A well known liquid column manometer, invented by Christian Huygens in 1661 is the U-tube [18].

The higher the column of fluid the more pressure it exerts, and so the liquid will reach a stable position that depends on the difference of the pressures:

$$H = \frac{P - P_{ref}}{\rho g}$$

with ρ the density of the fluid and g the gravitational acceleration.

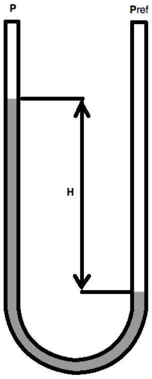

Figure 1.1: U-tube

This type of manometer is mainly used to measure small pressure variations for instance in air conditioning systems or atmospheric pressure monitoring devices. The density of the liquid and the available height of the column severely limit the range of pressure differences they can measure: for instance an U-tube 20 centimeters high filled with mercury ($\rho = 13579.04\, kg/m^3$) will at most indicate a pressure differential of roughly 0.27 bar. Liquid column manometers usually have an accuracy around ±1%, for a temperature of operation in the standard industrial range of -40/+60°C[1]. They can not be easily used in automated systems as they require an extra device to read the fluid levels, though this is still used in some instances [17, p. 4-03].

1.1.2 Piston

In a piston manometer the pressure acts to displace an air-tight piston and the user seeks an equilibrium by adding weights on that same piston. When the piston "floats" the forces are equalized; the pressure is then determined

---

[1] See for instance the various manometers by HK Instruments at www.hkinstruments.fi

through the simple relation $P = mg/S$ with m the mass of the weights, g the gravitational acceleration and S the surface area of the piston.

This method is mostly used in “dead weight testers” that serve as the standard instruments for the measurement of accuracy and the calibration of other pressure sensors [19][16, p. 26]. With precisely machined mechanical parts, dead weight testers can measure thousands of bars, attaining accuracies of up to 0.008%[2].

They are of course too big and impractical as automated control sensors but are nonetheless very important and widely used as test and calibration devices.

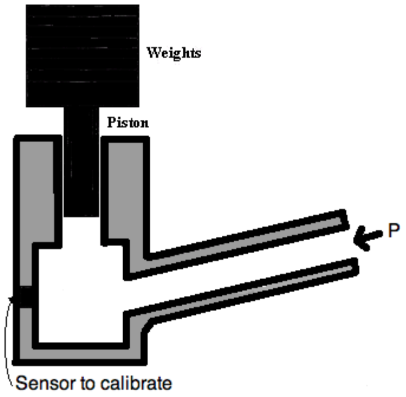

Figure 1.2: Dead-weight tester

1.2 Mechanical transducers

In mechanical transducers the pressure to be measured causes an elastic physical deformation of the sensing element. This deformation is then read through the displacement of a needle or through a secondary transducer. The particular case of electronic secondary transducers is detailed in section 1.3.

---

[2] See for instance Mensor (www.mensor.com) and Fluke DH Instruments Division (www.dhinstruments.com)

1.2.1 Bourdon Tube

A Bourdon Tube, named after Eugene Bourdon who invented the device in 1849, is a coiled tube, usually metallic, with its open end connected to the pressure to be measured. The tube will uncoil as the pressure increases and the rotation thus induced can be read directly by connecting it to a rotating needle pointing at a calibrated panel [16, pp. 35-40][17, p. 4.04].

They usually achieve accuracy around 1-0.5% for wide ranges of pressure measurement, typically up to 700 bar.

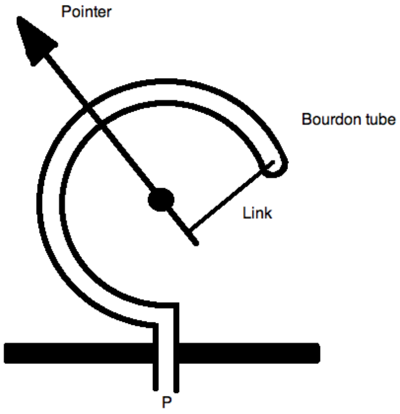

Figure 1.3: Bourdon Tube

A Bourdon tube manometer can be integrated in a control chain by adding an electronic deformation transducer on the tube itself or an angular position reader on the needle. This allows a single sensor to be used for quick visual checks in-situ as well as remote automated control. Additionally, even in the occurrence of a power failure, pressure can still be read manually making that kind of manometer a valuable security device.

1.2.2 Diaphragm

Other than Bourdon tubes, needle manometers can use a diaphragm system where a calibrated membrane is deflected by a difference of pressure on its two faces. The deflection of the membrane is then read from a panel as before, or a secondary device can be used to measure the displacement.

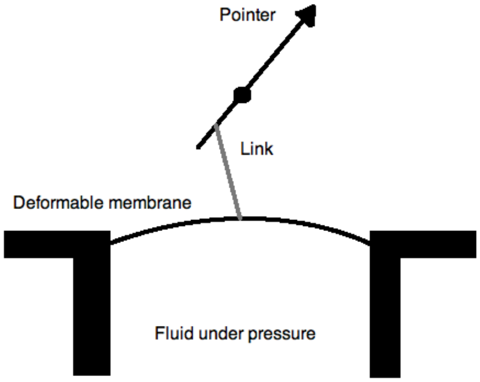

Figure 1.4: Diaphragm manometer

This type of device is very common in applications where high accuracy isn't important as it is usually around a few percents. On the other hand they are very simple and cheap to manufacture and are a good choice for specific applications. Compared to the Bourdon tube they also have the added advantage of providing chemical isolation between the fluid and the sensing element. The range of pressures they can measure is comparable to that of the Bourdon tubes and depends on the reference pressure applied to one side of the membrane.

As with the Bourdon tubes, the deflection value can be read from a secondary electronic transducer and integrated in a control chain.

1.3 Electronic transducers

Modern control sensors use electronic transducers as they permit an easy integration in a wider control chain. Most electronic pressure sensors do not directly transduce pressure to electricity; rather a calibrated diaphragm is deformed by the pressure and a strain gauge transforms the deformation into an electrical signal. Most of these transducers can of course be applied to not only diaphragms but also the other mechanical methods seen before though they are less common as they are bulkier.

1.3.1 Piezoresistive strain gauge

The piezoresistive effect is the variation of the electrical resistance of a conductor as its shape changes. In a piezoresistive strain gauge a metallic foil or a thin film is bonded to an insulating diaphragm, or alternatively the diaphragm is itself conductive. As the diaphragm is deformed by the applied pressure its resistance changes and this change is measured usually through a Wheatstone bridge that can measure minute resistance changes. Piezoresistive strain gages can be designed to measure a wide range of pressures, from a few millibars to hundred of bars [20][17, pp. 4.06-09].

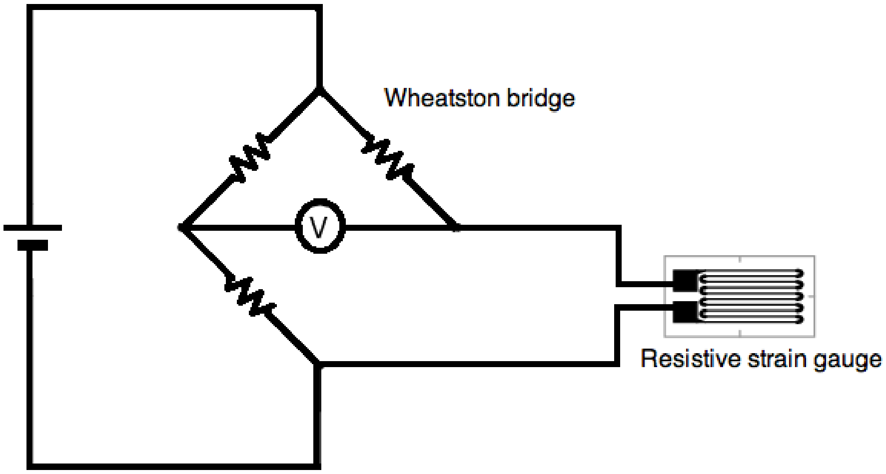

Figure 1.5: Typical resistive strain gauge arrangement

A modern form of piezoresistive sensor is the silicon strain gauge. The electrical resistance of silicon changes not only with a change in its geometry but also with the internal stress on the material. In this sense the silicon strain gauges, unlike the types presented before, is a direct pressure to electrical signal transducer. This effect is orders of magnitude greater than the piezoresistive response seen in metals and is now commonly used to create small and accurate pressure sensors that can be directly produced using the wide-spread microelectronics technologies. This is the most wide-spread technology for compact low cost pressure sensors [20, chp. 7], their main inconvenient being a high temperature dependence.

1.3.2 Capacitive strain gauge

A capacitive strain gauge is physically close to a piezoresistive gauge. The difference is that there is a second "plate" below the diaphragm, not physically in contact with it. The ensemble forms a capacitive cell in which the capacitance depends on the space between the two plates: as the pressure increases the top plate bonded to the diaphragm presses closer to the bottom plate and the capacity increases. A measure of this capacity is then linked to the pressure and values as low as a few hundred Pascals can be measured [20, chp. 8][17, chp. 9].

1.3.3 Magnetic strain gauge

A magnetic strain gauge uses one of a variety of magnetic effects to measure the deformation of a diaphragm. Examples include variation of the inductance of a deformed coil, through the displacement of the core of a fixed coil, variation in the magnetic field emitted by a fixed magnet through the Hall effect, and many others variations of the same principle [17, pp. 4-11].

Depending on the method used the accuracy and sensibility ranges can vary widely, but magnetic strain gauge have in common that they are usually bulkier than other types of sensors.

1.3.4 Other pressure sensing technologies

Many other less common methods exist, we can cite a few of them for reference.

Piezoelectric strain gauges use the piezoelectric properties of certain materials that generate an electric voltage when physically deformed. Their main advantage being their fast response time, they are mainly used to measure transient pressures[17, pp. 4-10]. Somewhat similar with magnetic strain gauges, potentiometric gauges can be designed where a potentiometer is acted upon by a deformed diaphragm resulting in a varying electrical resistance. A last class of interesting pressure sensor are resonant devices where the change in the geometry of a physical mechanism will modify its resonance frequency[20, chp. 9]. Finally, optical pressure sensors exist. They are mainly based on the properties of optical fibers. We describe these more in details in the next chapter.

Chapter 2

Optical pressure sensors in the scientific literature

This chapter focuses on optical pressure sensors that can be found in the scientific literature. The majority are based on waveguides, most of them optical fibers. When used as primary pressure transducers, waveguide sensors are referred to as *intrinsic* pressure sensors; when used as secondary transducers they are called *extrinsic* pressure sensors.

The basic principle of a waveguide transducer is simple: an external physical phenomenon modifies one of several parameters of the light that propagates within the guide; this change is then studied at the output of the guide. The properties of light on which these sensors are based are: intensity, guided modes, spectrum, phase (through interferometric detection) and finally state of polarization ([21]).

The challenge is, most of the time, to have *one specific* external perturbation act on *only one* parameter. Various designs have been proposed to answer this problem.

2.1 Phase modulation transducers

In phase modulation transducers, the phase of an optical signal is modulated in response to the applied pressure. The sensing beam is then compared to a reference beam through interferometry.

A Mach-Zender interferometer consists of two optical arms, one being the reference arm and the other one the measurement arm. The measurement beam sees its phase modulated by an external pressure before being recombined with the reference beam; the phase difference will result in interference fringes or a variation of intensity ([22, 23, 24]). A good example of implementation is the optical fiber Mach-Zender interferometer described in figure 2.1.

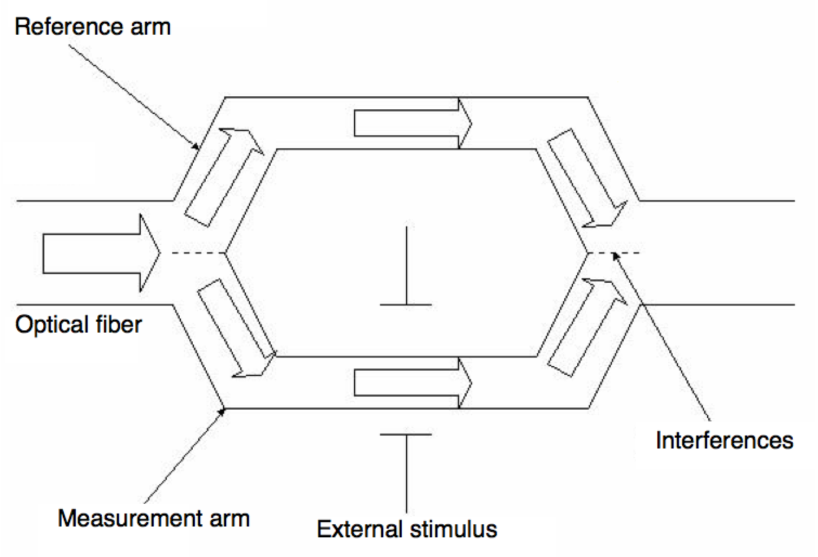

Figure 2.1: Fiber Mach-Zender interferometer

The fiber is split and then recombined through two Y-couplers. The phase in the measurement arm will depend on the pressure applied on the fiber and the intensity of the light at the exit port or the fiber will vary.

Integrated waveguides transducers work on the same principles as their fibered counterparts. They have the added advantage that they can be mass-produced using the usual tools developed for microelectronic components. On the other hand, the coupling of light in and out of these integrated waveguides poses several problems of packaging, limiting their applications.

Fiber-tip fabry-perot are an interesting class of interferometric sensors where the tip of a singlemode fiber is modified so that a small fabry-perot cavity exists [25]. This kind of sensor is punctual but occupies a very precise and small spot, making it ideal for precise measurements in difficult situations such as endoscopy or any application where the sensor has to travel through a narrow conduit.

Phase modulation transducers are generally very sensitive and accurate, at the expense of a much higher cost of development and operation. They are typically reserved to specific applications in controlled environments.

2.2 Spectrum modulation transducers

Spectrum modulation transducers modulate the spectral response of an element depending on the pressure.

The basic principle is that of a Bragg grating inscribed in an optical fiber. The grating will transmit and reflect a particular portion of a spectrum depending on the spacing of its layers. An external pressure on the fiber will slightly elongate it, modifying the spacing and the transmitted spectrum ([26]). This principle is illustrated on figure 2.2.

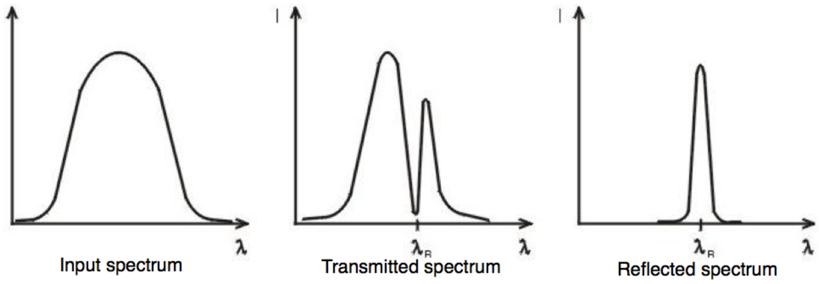

Figure 2.2: Typical transmitted and reflected spectrum for a Bragg grating

Another interesting spectrum-modulation device is the O-ring resonator [27]. A ring-shaped guide next to a straight waveguide will resonated at a specific wavelength and thus absorb a portion of the spectrum. A pressure on the o-ring will modify its index and hence its resonant frequency, resulting in a change in the transmitted spectrum.

As with phase modulation transducers, pressure transducers based on this principle will be usually expensive, mainly due to the price of the source and detector, and are thus reserved for special applications. One domain where they prove useful is distributed sensing over a wide area: several Bragg gratings can be inscribed in a single fiber, and each can be polled using time-resolved spectral analysis.

2.3 Polarization modulation transducers

In polarization modulation transducers the state of polarization of a light beam is dependent on the pressure.

Singlemode optical fiber polarimetric transducers take advantage of the fact that when stressed by a force from a given direction a singlemode fiber will become birefringent, ie it will have an effect on the state of polarization of light. In its simplest incarnation, this method consists in a weighted membrane that stresses a fiber, which modifies the output state of polarization ([28]). A typical communication-grade singlemode fiber has a small intrinsic birefringence that makes the exploitation of this effect difficult over long distances (typically a few meters). Moreover this technique will typically only work for directional forces applied on the fiber which mandates the use of a deformable membrane if one wishes to measure an hydraulic pressure.

Integrated O-rings produce a very similar effect, with the added benefit of being totally integrated on silicium and thus easily producible using the well mastered techniques of microelectronics [27].

Polarization maintaining fibers are special optical fibers designed to maintain a constant state of polarization of the light over long distances. They do so by imposing a very large intrinsic birefringence through a special geometry of the core of the fiber. This birefringence can be modified by an external modulation. For instance an isotropic pressure will slightly modify the shape of the core, modifying the birefringence and the output state of polarization ([29, 30, 31]). These fibers are much more expensive that classical singlemode fibers, but they allow direct measurement of an hydraulic pressure.

2.4 Intensity modulation transducers

In this kind of transducers the intensity of the light is directly modified. This is the cheapest and simplest method, but its performances are lower than that of other devices based on different principles.

Microbending transducers work by locally deforming a multimode optical fiber at a given period [32, 33, 34, 2, 35]. This is typically done through rigid "teeth" pressing on the fiber, and a variation in this pressure will result in a variation of the losses of the fiber and a global lowering in light intensity.

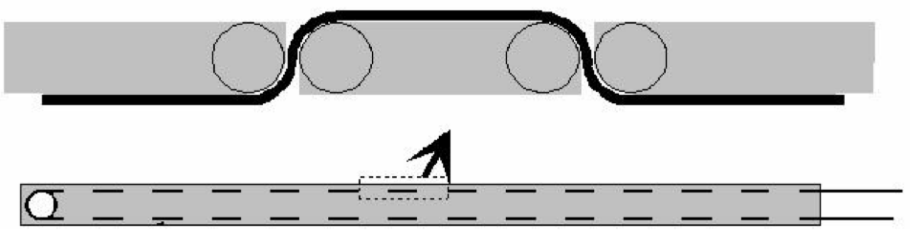

Figure 2.3: Multimode fiber microbendings transducer

Reflective membranes can be used to modulate the intensity of a signal. A fixed fiber illuminates the membrane and a second fiber picks up the reflected light. The intensity will directly depend on the distance between the reflective surface and the fibers.

Mechanical obturation will also modulate the amplitude of light. A membrane will move in the path of a light source as the pressure increases, decreasing the intensity received by a detector.

All these methods are cheap by themselves, but they offer no real advantages over cheaper and more robust electronic transducers except for use in electromagnetically polluted environment. The exception may be the microbending sensors as variations on the basic idea have seen recent industrial development for distributed and distant sensing [36].

Chapter 3

Proposition of a novel optical pressure sensor

In this chapter we state the technical and technological requirements of a new pressure sensor that uses an optical pressure transducer. These requirement were provided by Hydac and the goal is to develop a low-cost high hydrostatic pressure optical sensor. From these requirements we eliminate several potential technologies and conclude by proposing a new concept for an original optical pressure sensor.

3.1 Problem statement

The development of the new pressure sensor that we propose has been guided by two distinct considerations.

The first was of a technological nature: the goal was to design a pressure transducer that makes use of optical effects to generate a measurable signal. A well designed optical sensor is insensitive to high electric and magnetic fields as well as intrinsically safe in dangerous environments (such as explosive gas or fluids) as long as is relies on low-power optical effects. Moreover it should be possible to reach a high precision and accuracy through such a system, at least as good, if not better, than typical electrical sensors of equivalent price and application ranges. For all these reasons such a development is desirable.

The second consideration was a more commercial aspect associated with the production of pressure sensors. As explained in the previous chapter the most common type of hydrostatic pressure sensor is the piezoresistive strain gauge. Its most common implementation for sensors that aim to achieve precisions around one percent is through thin film deposition directly on a ceramic layer, layer itself bonded to the metal membrane under stress. The deposition process requires access to expensive equipments such as a clean room or vacuum sputtering machines as well as to highly skilled workers. The thickness of the metal membrane is of paramount importance as it will dictate the sensitivity of the final device. All these difficulties contribute to the production of elements of extremely variable quality unless there is a strict process control, another expensive step. All sensors will still need to be calibrated, the calibration information written to a micro controller, and this information used in signal conditioning in order to give accurate pressure readings.

In light of these problems it was decided to look into the feasibility of an optical pressure sensor that would meet the specifications detailed below.

The prime technical goal was to develop a sensor that would fit in Hydac's current commercial offering. As such the proposed sensor should measure the same ranges of pressure, work in similar conditions with similar resolution and accuracy and have about the same production price as Hydac's piezoresistive pressure sensors. A detailed list of technical requirements is presented in annex A, and we highlight here the main points:

Working pressure range: The sensor should be able to measure hydraulic pressure (relatively to the ambient pressure) in the 0-100 bar range approximately. It should be able to sustain a transient pressure of 600 bar without permanent damage or loss of containment.

Precision and accuracy: The sensor should output a value of pressure with a total uncertainty better than one percent of the full measurement scale (1% FS). Ideally the intrinsic accuracy should be good enough that no calibration is required after production.

Environmental sensitivity: The sensor should maintain its measurement performances in the -20°C to +70°C temperature range. It should not be sensitive to other external factors such as the nature of the fluid under pressure or ambient vibrations, magnetic or electric fields.

Production cost: The total cost of the parts used to build the sensor should not exceed a few euros, and it should not require access to highly specific processes or machines such as clean rooms technologies.

Safety: The sensor should be adapted or adaptable to safe remote sensing where no electrical current is present near the sensing element.

3.2 Proposition of a low cost piezo-optic pressure sensor

If we look back at the pressure sensors found in the literature described in Chapter 2 with the conditions highlighted above in mind, we can restrict the number of usable technologies.

Phase modulation sensors rely either on silicon waveguide or on singlemode optical fibers and so their fabrication processes require the use of expensive specific tools: access to a clean room and integrated electronics processing facilities for waveguides, various cleavers, splicers and expensive light sources for fibers. Moreover production of sensors that use singlemode fibers cannot easily be automated as their tuning is complex. Each unit would essentially be hand-crafted with all the problems it entails.

Spectrum modulation technologies, based on Bragg gratings, pose essentially the same problems, with the added requirement of an expensive method to analyze the output spectrum for each sensor.

Intensity modulation sensors are more promising since they can make use of telecom multimode optical fiber which are much easier to handle than singlemode ones. Moreover, multimode fiber can also be used with a simple LED as a light source. The main drawback is that a sensor based on an optical fiber would require qualified handling as well as difficult development of special machines if the production process is to be automated for mass production.

Finally, polarimetric sensors typically use standard singlemode fibers, polarization maintaining fibers or integrated waveguides, all methods we have eliminated earlier.

Although the typical fibered polarimetric pressure measurement methods found in the literature are not adapted to our specific problem, partially due to industrialization difficulties, the nature of this measurement method is interesting by itself. As explained before a polarimetric sensor relies on the fact that the refraction index of a material will change due to internal stress; an anisotropic distribution of index will then lead to a change in the polarization of a beam of light that propagates through it. This fact, known as *photoelasticity*, has long been used in structural engineering before we came to rely on finite element deformation simulations: once a structure, for instance a bridge, has been designed, a miniature replica would be fabricated in a transparent material. Loading the model would stress it in a similar manner to a real load on the real bridge, and the repartition of stress could be visualized using polarizers [37, 38, 39, 40, 41, 42].

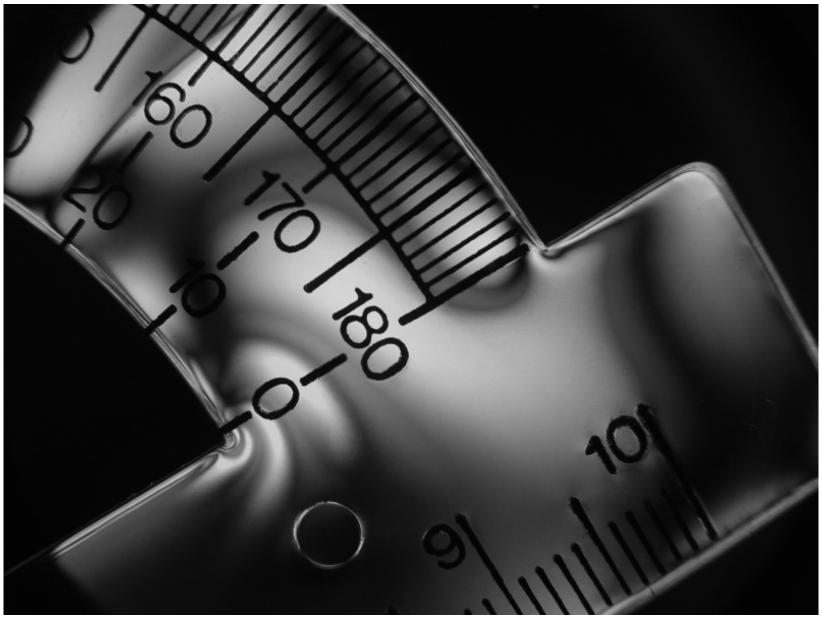

Figure 3.1: Example of photoelasticity: visualization of residual stress in a plastic ruler due to its fabrication process *(Source: Nevit Dilmen, with permission under Creative Commons Attribution ShareAlike 3.0)*

Nowadays the elasto-optic effect is mostly used in light deflectors, light modulators, and high-precision polarization generators [43]: a device precisely controls the force applied on a transparent material which then becomes birefringent with a very precisely controlled variable phase retardance.

This same technique can be used to measure an external pressure. The basic concept is the following: the sensor will consist of a piece of transparent material between two crossed polarizers. The light source is a simple LED and the detector any kind of photodetector. As the pressure on the material increases the polarization of the light inside the material will change, and as it is filtered by the output polarizer so will the output light intensity.

In the next chapters of this report this initial concept will be detailed, refined and optimized. We will modelize it and analyze its performances in the context of the constraints presented above.

Part II

Theoretical Tools

Introduction

One of the first scientific descriptions of a polarization effect dates from 1669 when Danish mathematician Erasmus Bartholinus performed a series of experiments involving a natural crystal named “Iceland Spar”. He reported that when looked through in a certain way the scene behind the crystal is doubled into two slightly separated but roughly identical images.

In 1677 Christian Huygens, a Dutch mathematician, physicist and astronomer, first describes light as a wave and shows that the well-known Snell-Descartes rules of reflection and refraction are compatible with this new model. Also experimenting with Iceland Spar, he notices that light is split into two paths as it goes through the crystal but that each path will not split further is sent through a second crystal oriented in the same manner as the first one. He interprets this behaviour as natural light possessing two “sides” that Iceland Spar can separate.

Thomas Young proposes in 1801 his now famous double-slits interference experiment that validates the wave-like nature of light imagined by Huygens. Later, both Young and Augustin-Jean Fresnel independently show that “double refraction” as it occurs in Iceland Spar can be explained if light is described as the sum of two perpendicular waves that oscillate in planes themselves perpendicular to the direction of propagation of the ray. At this point the polarization phenomena can be formalized and further studied in a quantitative manner.

These results were later explained by the Electro-Magnetic theory that culminated in the development by physicist James-Clerck Maxwell in 1861 of the first version of the now well known set of equations that govern classical electromagnetism, the Maxwell Equations.

In Chapter 4 we begin the mathematical study of polarization from these general equations before presenting further tools more adapted to the description and representation of polarized light, most importantly the

Mueller-Stokes formalism.

We then describe in Chapter 5 the behavior of polarized light in transparent media that present an anisotropic index of refraction. We describe the particular case of pressure-induced birefringence, the piezo-optic effect. Finally we use the Mueller matrix formulation to describe the effect on polarization of the piezo-optic effect as well as of partial and total reflection at a dielectric boundary. These tools will then be used in part III to modelize the proposed piezo-optic pressure sensor.

Chapter 4

Polarization of light

In this chapter we present the mathematical description of light as an electromagnetic field before exposing some of the useful tools developed to study the particular problem of polarization.

4.1 Light as a vectorial electromagnetic field

4.1.1 The free space wave equation

Let us begin by writing down the well-known macroscopic Maxwell equations that describe the behaviour of electromagnetic fields [44]:

$$\nabla \times \mathbf{E}(\mathbf{r}, t) = -\frac{\partial \mathbf{B}(\mathbf{r}, t)}{\partial t} \tag{4.1}$$

$$\nabla \times \mathbf{H}(\mathbf{r}, t) = \mathbf{J}(\mathbf{r}, t) + \frac{\partial \mathbf{D}(\mathbf{r}, t)}{\partial t} \tag{4.2}$$

$$\nabla \cdot \mathbf{D}(\mathbf{r}, t) = \rho(\mathbf{r}, t) \tag{4.3}$$

$$\nabla \cdot \mathbf{B}(\mathbf{r}, t) = 0 \tag{4.4}$$

A bold font indicates a vector while variables in italic are scalar. The $\nabla\cdot$ and $\nabla\times$ operators are respectively the *divergence* and *rotation* (or *curl*) operators that act on a vector $\mathbf{F} = F_x\mathbf{i}+F_y\mathbf{j}+F_z\mathbf{k}$ in a Cartesian basis $(\mathbf{i}, \mathbf{j}, \mathbf{k})$ in the following manner:

$$\nabla \cdot \mathbf{F} = \frac{\partial F_x}{\partial x} + \frac{\partial F_y}{\partial y} + \frac{\partial F_z}{\partial z}$$

$$\nabla \times \mathbf{F} = (\frac{\partial F_z}{\partial y} - \frac{\partial F_y}{\partial z})\mathbf{i} + (\frac{\partial F_x}{\partial z} - \frac{\partial F_z}{\partial x})\mathbf{j} + (\frac{\partial F_y}{\partial x} - \frac{\partial F_x}{\partial y})\mathbf{k}$$

$\mathbf{E}(\mathbf{r}, t)$ and $\mathbf{H}(\mathbf{r}, t)$ are respectively the electric and magnetic field vectors, $\mathbf{D}(\mathbf{r}, t)$ is the electric displacement field, $\mathbf{B}(\mathbf{r}, t)$ is the magnetic induction vector,$\mathbf{J}(\mathbf{r}, t)$ is the total current density and $\rho(\mathbf{r}, t)$ the total charge density. $\mathbf{r} = x\mathbf{i} + y\mathbf{j} + z\mathbf{k}$ is of course the position of a point in space and t represents the time variable.

In the special case of free space, we have the following additional relations:

$$\mathbf{D}(\mathbf{r}, t) = \varepsilon_0 \mathbf{E}(\mathbf{r}, t) \tag{4.5}$$

$$\mathbf{B}(\mathbf{r}, t) = \mu_0 \mathbf{H}(\mathbf{r}, t) \tag{4.6}$$

where $\varepsilon_0 \approx 8.85 \times 10^{-12} As/Vm$ is the permittivity of free space and $\mu_0 = 4\pi \times 10^{-7} H/m$ is its permeability [44, p. 4].

Free space also implies an absence of free charges, and hence of currents, ie $\mathbf{J}(\mathbf{r}, t) = 0$ and $\rho(\mathbf{r}, t) = 0$. Combined with all of this equations 4.7 through 4.10 now become:

$$\nabla \times \mathbf{E}(\mathbf{r}, t) = -\mu_0 \frac{\partial \mathbf{H}(\mathbf{r}, t)}{\partial t} \tag{4.7}$$

$$\nabla \times \mathbf{H}(\mathbf{r}, t) = \varepsilon_0 \frac{\partial \mathbf{E}(\mathbf{r}, t)}{\partial t} \tag{4.8}$$

$$\nabla \cdot \mathbf{E}(\mathbf{r}, t) = 0 \tag{4.9}$$

$$\nabla \cdot \mathbf{H}(\mathbf{r}, t) = 0 \tag{4.10}$$

Taking the curl of 4.7 yields

$$\nabla \times \nabla \times \mathbf{E}(\mathbf{r}, t) = -\mu_0 \frac{\partial}{\partial t}(\nabla \times \mathbf{H}(\mathbf{r}, t))$$

and combined with equation 4.2 it becomes

$$\nabla \times \nabla \times \mathbf{E}(\mathbf{r},t) = -\mu_0\varepsilon_0 \frac{\partial^2 \mathbf{E}(\mathbf{r},t)}{\partial t^2}$$

Given that $\nabla \times \nabla \times \mathbf{E}(\mathbf{r},t) = \nabla \cdot \nabla \cdot \mathbf{E}(\mathbf{r},t) - \nabla^2 \mathbf{E}(\mathbf{r},t)$ and that equation 4.9 sets $\nabla \cdot \mathbf{E}(\mathbf{r},t) = 0$, we no have:

$$\nabla^2 \mathbf{E}(\mathbf{r},t) = \mu_0\varepsilon_0 \frac{\partial^2 \mathbf{E}(\mathbf{r},t)}{\partial t^2} \tag{4.11}$$

This equation is known as the *propagation equation.* Any solution to this equation will be a solution to the free space Maxwell equations and describe one of the many types of behaviors an electromagnetic field can displays. The first observation we can make it that there appear to be solutions other than a null field, which entails that an electromagnetic field can exist in the absence of charges and currents. A second observation is that there is a whole class of material known as *dielectric materials* in which there are no free charges; any solution to equation 4.11 will be valid for propagation in these materials by substituting ε and μ the permittivity and permeability of the material to ε_0 and μ_0; for most materials $\mu \approx \mu_0$ [45, p. 3]. These solution will notably be valid for propagation in glass, clear plastics or various types of crystals. A final observation is that as this type of equation is present throughout physics it is known that its solution represent propagating waves with phase velocity $c_0 = 1/\sqrt{\varepsilon_0\mu_0}$, c_0 being in this case the speed of light in a vacuum. In the case of propagation in a dielectric material the phase velocity is $c = c_0/n = 1/\sqrt{\varepsilon\mu} = \sqrt{\frac{\varepsilon\mu}{\varepsilon_0\mu_0}}/\sqrt{\varepsilon_0\mu_0} = c_0\sqrt{\frac{\varepsilon\mu}{\varepsilon_0\mu_0}}$ with $n = 1/\sqrt{\frac{\varepsilon\mu}{\varepsilon_0\mu_0}} \approx 1/\sqrt{\varepsilon_r}$ being the refractive index and $\varepsilon_r = \varepsilon/\varepsilon_0$ the relative permittivity. Finally we rewrite equation 4.11 as:

$$\nabla^2 \mathbf{E}(\mathbf{r},t) - \frac{1}{c^2} \cdot \frac{\partial^2 \mathbf{E}(\mathbf{r},t)}{\partial t^2} = 0 \tag{4.12}$$

4.1.2 Plane waves

4.1.2.1 The plane wave solution

There exists a relatively simple class of solutions to the wave equation called the *plane wave* solution. Let us consider the special case where $\mathbf{E}(\mathbf{r},t)$ only depends on one spacial direction, for instance z, and on time. Equation 4.12 now becomes:

$$\frac{\partial^2 \mathbf{E}(z,t)}{\partial z^2} - \frac{1}{c^2} \cdot \frac{\partial^2 \mathbf{E}(z,t)}{\partial t^2} = 0 \tag{4.13}$$

which can be rewritten as

$$\left(\frac{\partial .}{\partial z} - \frac{1}{c} \cdot \frac{\partial .}{\partial t} \right) \left(\frac{\partial .}{\partial z} + \frac{1}{c} \cdot \frac{\partial .}{\partial t} \right) \mathbf{E}(z,t) = 0$$

We now introduce the new variables $a = z + ct$ and $b = z - ct$, combine them to get:

$$t = \frac{1}{2c}(a - b),\ z = \frac{1}{2}(a + b)$$

and through differentiation:

$$\frac{\partial .}{\partial a} = \frac{1}{2} \left(\frac{\partial .}{\partial z} - \frac{1}{c} \cdot \frac{\partial .}{\partial t} \right),\ \frac{\partial .}{\partial b} = \frac{1}{2} \left(\frac{\partial .}{\partial z} + \frac{1}{c} \cdot \frac{\partial .}{\partial t} \right)$$

This transformation allows us to rewrite equation 4.13 as

$$\frac{\partial^2 \mathbf{E}(z,t)}{\partial a \partial b} = 0$$

which has for obvious solution any function $\mathbf{E}(z,t)$ such that

$$\mathbf{E}(z,t) = \mathbf{E}_1(a) + \mathbf{E}_2(b)$$

ie

$$\mathbf{E}(z,t) = \mathbf{E}_1(z + ct) + \mathbf{E}_2(z - ct)$$

If we consider the case $\mathbf{E}_1 = 0$ we find that $\mathbf{E}(z,t) = \mathbf{E}(z - ct)$ which is a function with a constant value at all (z,t) pairs such that $z = ct + constant$. Since $\mathbf{E}(z,t)$ doesn't depend on x or y, it it described by an unique vectorial value in any given (x,y) plane. If we know that value at any point (x_i, y_i) in the plane $z = 0$ at time $t = 0$, $\mathbf{E}(x_i, y_i, z = 0, t = 0) = \mathbf{E_0}$, then the same uniform plane with value $\mathbf{E_0}$ will be present at any instant and position such that $z = ct$: *this solution propagates uniform infinite planes through space at speed* c*, positively along the z axis.* Each plane of the function behaves in a similar manner, and this particular solution to the propagation equation is known as a *plane wave.* The same reasoning holds for $\mathbf{E}(z + ct)$ which represents a plane wave propagating along z in the negative direction, and the whole demonstration can of course be applied to $\mathbf{H}(\mathbf{r}, t)$ with similar conclusions.

4.1.2.2 Properties of plane waves

For the sake of clarity we only derive the properties of the plane waves using forward propagating waves, but the results are trivially demonstrated in the general case.

A first interesting general property of plane waves can be determined by through the use of equation 4.9, $\nabla \cdot \mathbf{E}(\mathbf{r}, t) = 0$, applied to a plane wave:

$$\begin{aligned}\nabla \cdot \mathbf{E}(z - ct) &= \frac{\partial E_x(z-ct)}{\partial x} + \frac{\partial E_y(z-ct)}{\partial y} + \frac{\partial E_z(z-ct)}{\partial z} \\ &= \frac{\partial E_z(z-ct)}{\partial z} \\ &= \frac{\partial E_z}{\partial z}(z-ct) \\ &= 0\end{aligned}$$

This final equation $\frac{\partial E_z}{\partial z}(z-ct) = 0$ tells us that E_z is constant for all values of the position z at a given instant t, and it follows from our previous demonstration that a plane wave propagates without changes along z that it must also be constant at all instants in time. The same demonstration can be applied to $\mathbf{H}(z - ct)$ and in the end we have the following relationships:

$$\begin{cases} E_z(z-ct) = \mathit{constant}\,1 \\ H_z(z-ct) = \mathit{constant}\,2 \end{cases} \tag{4.14}$$

We see from equation 4.14 that a plane wave can only have constant electric or magnetic fields along its direction of propagation. Taking these constants to be anything else than zero leads to interesting theoretical implications, but this case is usually ignored for reasons explained bellow in section 4.1.2.3. If the longitudinal field is null then all components of the electromagnetic wave are contained in a plane perpendicular to the direction of propagation, and such a plane wave is said to be *transverse*.

Another important property of a plane wave concerns the relationship between $\mathbf{E}(\mathbf{r}, t)$ and $\mathbf{H}(\mathbf{r}, t)$. Taking the curl of the electric field of a plane wave $\mathbf{E}(z, t) = \mathbf{E}(z-ct) = \mathbf{E}(b)$ and the time derivative of the corresponding magnetic field, we have:

$$\begin{aligned}
\nabla \times \mathbf{E}(\mathbf{r},t) &= \nabla \times \mathbf{E}(z-ct) \\
&= (\frac{\partial E_z(z-ct)}{\partial y} - \frac{\partial E_y(z-ct)}{\partial z})\mathbf{i} \\
&\quad + (\frac{\partial E_x(z-ct)}{\partial z} - \frac{\partial E_z(z-ct)}{\partial x})\mathbf{j} \\
&\quad + (\frac{\partial E_y(z-ct)}{\partial x} - \frac{\partial E_x(z-ct)}{\partial y})\mathbf{k} \\
&= -\frac{\partial E_y(b)}{\partial z}\mathbf{i} + \frac{\partial E_x(b)}{\partial z}\mathbf{j} \\
&= -\frac{\partial E_y(b)}{\partial b}\frac{\partial b}{\partial z}\mathbf{i} + \frac{\partial E_x(b)}{\partial b}\frac{\partial b}{\partial z}\mathbf{j} \\
&= -\frac{\mathrm{d}E_y(b)}{\mathrm{d}b}\mathbf{i} + \frac{\mathrm{d}E_x(b)}{\mathrm{d}b}\mathbf{j} \\
\frac{\partial \mathbf{H}(\mathbf{r},t)}{\partial t} &= \frac{\partial \mathbf{H}(z-ct)}{\partial t} \\
&= \frac{\partial H_x(z-ct)}{\partial t}\mathbf{i} + \frac{\partial H_y(z-ct)}{\partial t}\mathbf{j} + \frac{\partial H_z(z-ct)}{\partial t}\mathbf{k} \\
&= -c\frac{\mathrm{d}H_x(b)}{\mathrm{d}b}\mathbf{i} + -c\frac{\mathrm{d}H_y(b)}{\mathrm{d}b}\mathbf{j}
\end{aligned}$$

Injecting these results in equation 4.7 we end up with the sets of equations:

$$\begin{cases} \frac{\mathrm{d}E_y(b)}{\mathrm{d}b} = & -\mu_0 c\frac{\mathrm{d}H_x(b)}{\mathrm{d}b} \\ \frac{\mathrm{d}E(b)}{\mathrm{d}b} = & \mu_0 c\frac{\mathrm{d}H_y(b)}{\mathrm{d}b} \end{cases}$$

and integrating with respects to b yields:

$$\begin{cases} E_y = & -\mu_0 c H_x \\ E_x = & \mu_0 c H_y \end{cases}$$

and finally we obtain the equality:

$$E_x H_x + E_y H_y = \mu_0 c H_y H_x - \mu_0 c H_x H_y = 0 \tag{4.15}$$

We recognize in equation 4.15 a null scalar product between the two vectors **E** and **H**, which indicates that *the electric and magnetic fields of a plane wave are always perpendicular to each other*, as well as to the propagation direction as demonstrated before.

4.1.2.3 Monochromatic plane waves

So far we have imposed no special condition on the behaviour of $\mathbf{E}$ or $\mathbf{H}$ except that they are at least twice derivable. There is one special case that is of particular physical importance because it describes everyday light and "colors", the case where all components of $\mathbf{E}$ and $\mathbf{H}$ are simple harmonic functions of time. Such a wave oscillates at a single frequency with time, and since each color corresponds to a different frequency it is called a *monochromatic wave.* When combined with the concept of plane wave we get one of the most basic and useful entities used to describe the behaviour of light : the *monochromatic plane wave.*

First let us look back at equation 4.14: the longitudinal fields can only be constant which is incompatible with the harmonic property of monochromatic plane waves unless the oscillating frequency is null or the amplitude of this component is zero. Since we are not concerned with static field the only possibility is that the longitudinal component is always null, and thus *a monochromatic plane wave is always transverse.*

Let us consider a forward propagating plane wave as before. The electric field only depends on $z-ct$, and we recall that $\mathbf{E}(z-ct)$ is a vector function: both its amplitude *and orientation* can vary with $z-ct$ and one has to decompose it into its scalar projections on $(\mathbf{i},\mathbf{j})$ to explicit the function (a monochromatic plane wave has no component along $\mathbf{k}$ as discussed before). We can now write:

$$\mathbf{E}(z-ct)\ \begin{cases} E_x = E_{0x}\cos(k(z-ct)+\varphi_x) \\ E_y = E_{0y}\cos(k(z-ct)+\varphi_y) \end{cases} \tag{4.16}$$

which describes the most general configuration of the monochromatic plane wave. k is a constant, the *wave number,* φ_x, φ_y simply serve to set the initial value of each component at $t=0$,$z=0$, and the overall argument to the cosinus, $(k(z-ct)+\varphi_x)$, is called the *phase* of the wave. It is easy to identify the pulsation of the wave as the coefficient in front of t so $\omega = kc$ and its frequency is $\nu = \omega/2\pi = kc/2\pi$.

If we now "freeze" the wave in time and look at its spatial values we see that it follows a wave with spatial period $\lambda = 2\pi/k = 2\pi c/\omega = c/\nu$. This spatial period is called the *wavelength* of the light and is the most widely used value to describe a given monochromatic wave.

It is important to note that a monochromatic plane wave is defined as an harmonic function of *time* and for a good reason: most detectors (such as the eye ...) detect color depending on the time frequency of the light. The wavelength for a given time frequency depends on the speed of light and thus *the wavelength will vary depending on the medium in which the light propagates.* When referring to a light of a particular wavelength one always refers to its wavelength *in a vacuum* to avoid confusion.

4.1.2.4 The complex notation for monochromatic plane waves

The trigonometric notation of equation 4.16, though useful in some cases, can lead to quite complicated calculations as soon as one wishes to use a plane wave to describe even simple phenomenon. An useful alternative representation of an harmonic plane wave is the complex notation that we describe now.

The representation presented in equation 4.16 make use of simple trigonometric functions. Using Euler's formula:

$$e^{ix} = \cos(x) + i\sin(x)$$

we immediately have:

$$\mathbf{E}(z-ct)\begin{cases} E_x = E_{0x}\cos(kz-\omega t+\varphi_x) = \Re\left\{E_{0x}e^{i(kz-\omega t+\varphi_x)}\right\} \\ E_y = E_{0y}\cos(kz-\omega t+\varphi_y) = \Re\left\{E_{0y}e^{i(kz-\omega t+\varphi_y)}\right\} \end{cases}$$

which can be rewritten as:

$$\begin{aligned} \mathbf{E}(z-ct) &= E_x\mathbf{i} + E_y\mathbf{j} \\ &= \Re\left\{E_{0x}e^{i(kz-\omega t+\varphi_x)}\right\}\mathbf{i} + \Re\left\{E_{0y}e^{i(kz-\omega t+\varphi_y)}\right\}\mathbf{j} \\ &= \Re\left\{\left(E_{0x}e^{i\varphi_x}\mathbf{i} + E_{0y}e^{i\varphi_y}\mathbf{j}\right)e^{i(kz-\omega t)}\right\} \end{aligned} \tag{4.17}$$

with $\Re$ the "real part" operator and i the imaginary unit (not to be confused with the bold **i** which still denotes one of the unit directing vectors of our basis).

The expression is now conveniently separated into a constant complex vector $\mathbf{D_0} = E_{0x}e^{i\varphi_x}\mathbf{i} + E_{0y}e^{i\varphi_y}\mathbf{j}$ and a complex exponential $e^{i(kz-\omega t)}$ which contains the time and space dependence of the field. As the wave propagates the exponential will act on the constant vector to change, in the most general case, both its length and its direction. To illustrate this principle, we plot the evolution of the vector $\mathbf{D_0} = 1e^{i\pi/4}\mathbf{i} + \frac{1}{2}e^{i0}\mathbf{j}$ at different instants at $z = 0$. For convenience we set $\omega = 1$. The electric field vector is then described by:

$$\begin{aligned}
\mathbf{E}(0,t) &= \Re\left\{(1e^{i\pi/4}\mathbf{i} + \frac{1}{2}e^{i0}\mathbf{j}) \cdot e^{i(0-t)}\right\} \\
&= \Re\left\{e^{i(\pi/4-t)}\right\}\mathbf{i} + \Re\left\{\frac{1}{2}e^{-it}\right\}\mathbf{j} \\
&= \cos(\pi/4 - t)\cdot\mathbf{i} + \frac{1}{2}\cos(-t)\cdot\mathbf{j}
\end{aligned}$$

which we plot on figure 4.1 for different values of t.

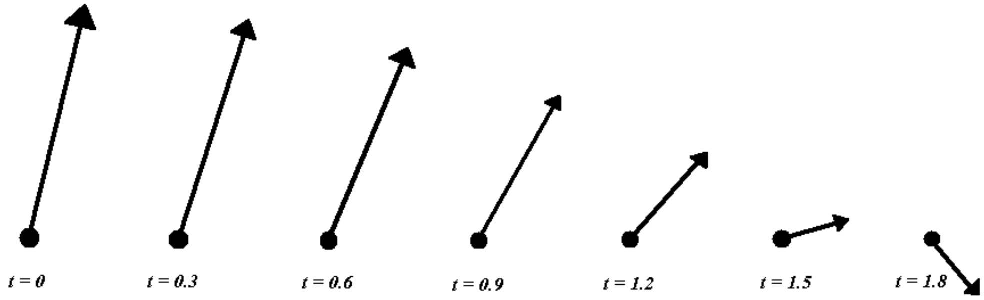

Figure 4.1: Example of the evolution of the electric field vector through time.

To simplify the representation the real part operator is usually omitted but it is implicitly understood that the last operation in a series of computations will always be to take the real part of the result. Using this convention we now represent the electric field component of a monochromatic plane wave in the following manner:

$$\mathbf{E}(z,t) = \mathbf{D_0}e^{i(kz-\omega t)}$$

Neglecting to take the real part during a calculation is correct as long as one only applies linear operations to the complex field but if we need to, for instance, multiply two fields as part of a non-linear process then the real part must be taken before carrying out the operation.

4.1.3 Defining polarization

At this point we have a solution, the monochromatic plane wave, that exactly corresponds to the representation of light proposed by Young and Fresnel as discussed in the introduction (cf. p.47): a wave oscillating in planes transverse to its direction of propagation that can be split into two perpendicular components due to its vectorial nature. It is precisely this vectorial nature that gives rise to the conventional definition of polarization: *to study polarization is to study the time-behavior of the electric field vector of a transverse monochromatic plane wave at a fixed point in space.*

It is important to remember that as shown here the notion of polarization is only strictly defined for a monochromatic plane wave when viewed in a plane transverse to the direction of propagation and that it is not trivial to generalize this notion to an arbitrary waveform. We stray a lot from this definition when dealing, for instance, with focused waves or high numerical aperture optical instruments. Special attention must be paid when carrying out experiments in polarization in order to stay in the region where our models and tools are valid.

4.2 The polarization ellipse

As we have seen in the previous section, the polarization of a plane wave describes the time-behaviour of its electric field vector. To visualize this behaviour, consider the following thought experiment: take an observation plane perpendicular to the direction of propagation of an incoming plane wave with arbitrary polarization, and as the wave passes through it observe the figure drawn on the virtual plane by the tip of the electric field vector as if it had a physical length proportional to its magnitude. Taking the same $\mathbf{D_0}$ as in figure 4.1, letting ωt vary between 0 and 2π in order to represent a full cycle, and superposing the vectors on the same figure, we obtain figure 4.2:

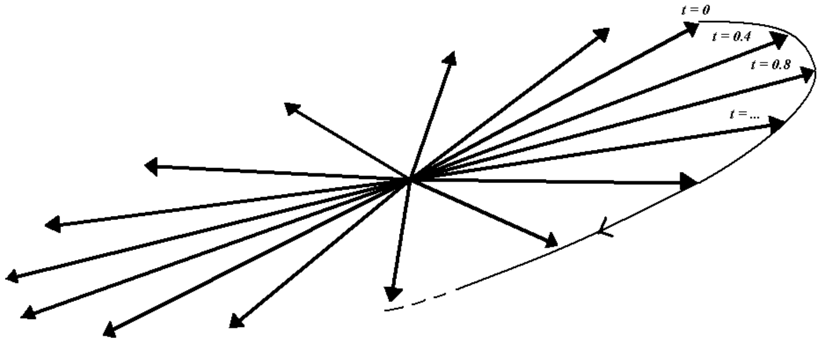

Figure 4.2: Evolution of the electric field vector through a full cycle.

As we see in this example, the field intensity will draw a figure that looks like an ellipse. Using equation 4.16 and setting $\tau = k(z - ct)$, we can prove that the figure is indeed always an ellipse:

$$\begin{cases} E_x = E_{0x}\cos(\tau + \varphi_x) \\ E_y = E_{0y}\cos(\tau + \varphi_y) \end{cases}$$

can be rewritten as

$$\begin{cases} \frac{E_x}{E_{0x}} = \cos(\tau)\cos(\varphi_x) - \sin(\tau)\sin(\varphi_x) \\ \frac{E_y}{E_{0y}} = \cos(\tau)\cos(\varphi_y) - \sin(\tau)\sin(\varphi_y) \end{cases}$$

which combines into

$$\begin{cases} \frac{E_x}{E_{0x}}\sin(\varphi_y) - \frac{E_y}{E_{0y}}\sin(\varphi_x) = \cos(\tau)\sin(\varphi_y - \varphi_x) \\ \frac{E_x}{E_{0x}}\cos(\varphi_y) - \frac{E_y}{E_{0y}}\cos(\varphi_x) = \sin(\tau)\sin(\varphi_y - \varphi_x) \end{cases}$$

and finally, by squaring and then adding:

$$\left(\frac{E_x}{E_{0x}}\right)^2 + \left(\frac{E_y}{E_{0y}}\right)^2 - 2\frac{E_x}{E_{0x}}\frac{E_y}{E_{0y}}\cos(\varphi_y - \varphi_x) = \sin^2(\varphi_y - \varphi_x) \qquad (4.18)$$

Equation 4.18, which describes the locus of points traveled by the "tip" of the electric field vector, is the equation of an ellipse, the *polarization ellipse*. A given polarization can thus be described by the two parameters that identify its associated polarization ellipse: the *orientation angle* ψ between the major axis and the horizontal direction, and the ellipticity angle χ often defined through its tangent being equal to the ratio of the lengths of the two axes, $\tan(\chi) = b/a$. Figure 4.3 illustrates the polarization ellipse and its parameters.

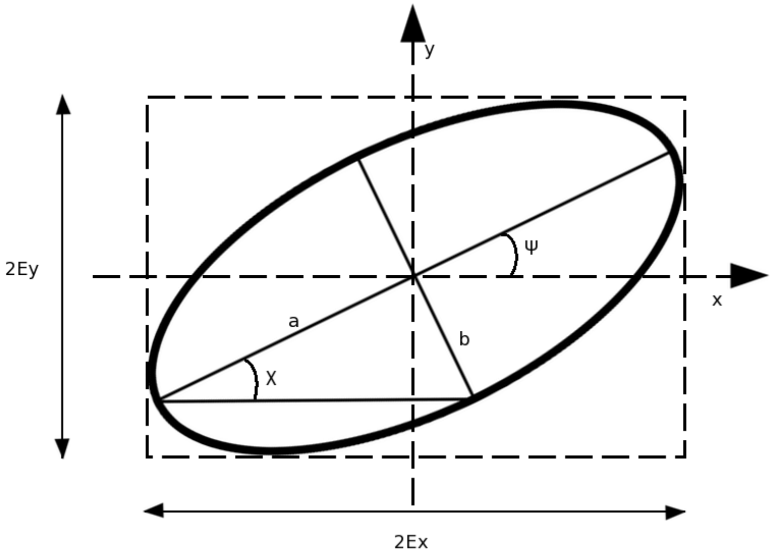

Figure 4.3: The polarization ellipse and its parameters.

ψ and χ are related to the physical parameters of the plane wave through the auxiliary angle α [45, p. 28]:

$$\begin{aligned}\tan(\alpha) &= \frac{E_{0y}}{E_{0x}} \\ \tan(2\psi) &= \tan(2\alpha)\cos(\delta) \\ \sin(2\chi) &= \sin(2\alpha)\sin(\delta)\end{aligned}$$

Using this tool we can explore a few special cases of polarization states. As we have seen, the figure is in general an ellipse. When $\chi = 0$, ie when either E_{0x} is null, E_{0y} is null, or the two components are in phase ($\delta = 0$), the figure is a line and describes *linear polarization* which can have any orientation, with two particular cases being *horizontal linear polarization* when $\phi = 0$ or *vertical linear polarization* when $\phi = \pi/2$. The locus becomes a circle when $a = b$ ie $\chi = \pm\pi/4$ and describes *circular polarization.* Figure 4.4 presents a few typical polarization ellipses and the physical parameters they derive from.

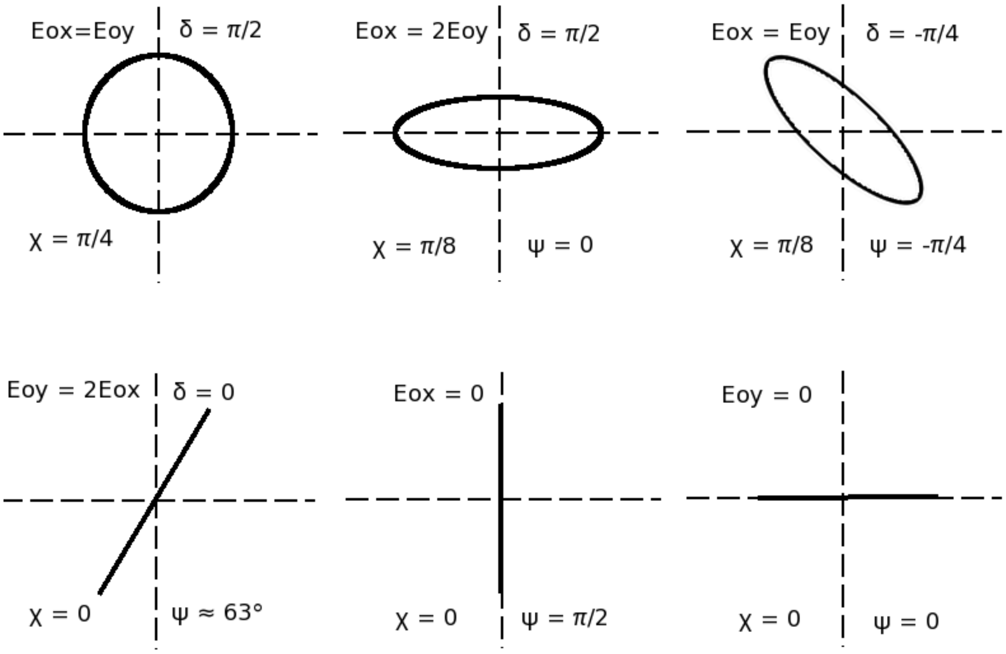

Figure 4.4: The polarization ellipse and its degenerate forms for different values of the physical parameters: circular polarization, two identical elliptic polarizations with different orientations, and three linear polarizations with various orientation.

4.3 Polarizing optical elements

As shown by the Iceland Spar that so puzzled Bartholinus, Huygens, Young and many others there are certain optical elements that have a direct effect on the state of polarization of light. We now present the most common of these elements as they will be widely used throughout the rest of this document.

4.3.1 The waveplate

A *waveplate* is an optical element that adds a known phase delay (the *retardance* of the waveplate) to light along one of its axes. The axis that adds a positive phase delay (i.e. the axis that adds more phase than the other) is known as the *slow axis* while the other one is the *fast axis* of the waveplate.

Let us consider a waveplate with retardance $\triangle\varphi$ in the path of a beam of light, its slow axis aligned along $\mathbf{i}$ and its fast axis along $\mathbf{j}$. The initial electric field is:

$$\mathbf{E}(z,t) = \mathbf{D_0}e^{i(kz-\omega t)} = (E_{0x}e^{i\varphi_x}\mathbf{i} + E_{0y}e^{i\varphi_y}\mathbf{j})e^{i(kz-\omega t)}$$

and after the waveplate it becomes:

$$\mathbf{E}(z,t) = (E_{0x}e^{i(\varphi_x+\triangle\varphi)}\mathbf{i} + E_{0y}e^{i\varphi_y}\mathbf{j})e^{i(kz-\omega t)} = \mathbf{D_1}e^{i(kz-\omega t)}$$

The state of polarization of the wave was modified by the waveplate, in this case simply acting on one component of the vector. If the plate is now rotated so that its axes are not aligned with $\mathbf{i}$ and $\mathbf{j}$ an angle dependent phase delay will be added to both components. The exact dependence on the inclination angle will be explicited in section 4.5.

We can express E_x as:

$$\begin{aligned} E_x &= E_{0x}e^{i(\varphi_x+\triangle\varphi)}e^{i(kz-\omega t)} \\ &= E_{0x}e^{i(kz-\omega t+\varphi_x+\triangle\varphi)} \\ &= E_{0x}e^{i(k(z+\frac{\triangle\varphi}{k})-\omega t+\varphi_x)} \\ &= E_{0x}e^{i(k(z+\frac{\triangle\varphi}{2\pi}\lambda)-\omega t+\varphi_x)} \end{aligned}$$

which expresses the phase delay as an extra length, $\triangle z$ given as a fraction of the wavelength, traveled by that component of the plane wave. For this reason waveplate retardance are usually given as a fraction of their design wavelength.

From the expression above we can identify two special values of $\triangle\varphi$ of particular importance. We simply present here their basic behavior as they will be studied in details in section 4.5.

If we select a linear polarization inclined of 45° $\mathbf{D_0} = E_0 e^{i0}\mathbf{i} + E_0 e^{i0_y}\mathbf{j} = E_0\mathbf{i} + E_0\mathbf{j}$ and send it through a waveplate with retardance $\triangle\varphi = \pi/2$ the output polarization vector will be $\mathbf{D_1} = E_0 e^{i\frac{\pi}{2}}\mathbf{i} + E_0 e^{i0_y}\mathbf{j} = E_0\imath\mathbf{i} + E_0\mathbf{j}$ which identifies a circular polarization. If we express the equivalent wavelength fraction we find $\triangle z = \frac{\triangle\varphi}{2\pi}\lambda = \frac{\lambda}{4}$ and this element is named a *quarter-wave plate.* A quarter-wave plate will transform a linear polarization at 45° into a circular polarization, and a circular polarization into a linear one.

The second interesting waveplate is the *half-wave plate* with retardance $\triangle\varphi = \pi$ or $\triangle z = \frac{\lambda}{2}$. It has the particular effect of modifying the orientation angle of an incoming polarization without changing its ellipticity. If viewed in terms of polarization ellipse the half-wave plate retains the shape of the ellipse but rotates it around its center.

4.3.2 The diattenuator

So far we have only acted on the phase of each components of the light but it is also interesting to only modify their amplitudes. Such optical elements exist and are called diattenuators: they absorb a different fraction of the light along each of their axes. The axis that transmits the most light is the *transmission axis.*

The most widely used diattenuator is the polarizer which totally absorbs light along its *extinction axis.* Take for instance a beam of circularly polarized light :

$$\begin{cases} E_x = E_0 cos(kz - \omega t) \\ E_y = E_0 cos(kz - \omega t + \frac{\pi}{2}) \end{cases}$$

if the polarizer has its extinction axis along $\overrightarrow{y}$ the resulting light will be described by

$$\begin{cases} E_x = E_0 cos(kz - \omega t) \\ E_y = 0 \end{cases}$$

which is clearly a linear vertical polarization. The perfect polarizer is an element that convert any incoming light into a perfectly linearly polarized output of, most of the time, a different intensity. The output intensity depends on the input state of polarization and two special cases can be highlighted : if the incoming light is linearly polarized along the transmission axis of the polarizer it will have no effect on it, while if the polarization lies perpendicularly to that axis no light at all will exit the system. For an angle in between the intensity follows Malus' Law:

$$I = \cos^2(\theta) \tag{4.19}$$

where θ is the angle between the orientation of the linear polarization and the orientation of the transmission axis of the polarizer.

4.4 The Stokes Polarization Parameters

4.4.1 Definition

The two representation of the state of polarization that we presented so far have an important drawback: they can only describe a totally polarized light, ie one that is totally described by the evolution of the electromagnetic field over a single period. Practical light sources show a different behaviour. Imagine for instance a light beam created by combining two uncorrelated linearly polarized light beams at 90° of each other. Let this beam pass through a linear rotating polarizer: whatever its orientation, the intensity on the detector will stay constant as per Malus' Law (4.19) applied once for each polarization; if we add a quarter-wave plate before the polarizer, the result is identical. According to the polarization ellipse the first observation would indicated a circularly polarized beam, but the second experiment is not consistent with this conclusion. This state of polarization can not be correctly described as the light, in this case, is *unpolarized.* In general light can be *totally polarized*, *partially polarized* or *unpolarized.*

In order to address this problem, as well as the fact that the polarization ellipse deals with field amplitudes while the only experimentally available quantity is the intensity which is a time-average of the amplitude, we introduce the *Stokes Polarization Parameters* [46, p. 57][44, p. 51]:

$$S_0 = \left\langle E_x(t)^2 \right\rangle + \left\langle E_y(t)^2 \right\rangle \tag{4.20}$$

$$S_1 = \left\langle E_x(t)^2 \right\rangle - \left\langle E_y(t)^2 \right\rangle \tag{4.21}$$

$$S_2 = \langle 2E_x(t)E_y(t) \rangle \tag{4.22}$$

$$S_3 = \left\langle 2E_x(t)E_y(t - \frac{\pi}{2} \cdot \frac{1}{\omega}) \right\rangle \tag{4.23}$$

where $\langle\ \rangle$ denotes a time average, and as before $E_i(t)$ is the amplitude of the field along axis i at instant t. S_0 is the sum of the average intensities along the two axes, S_1 is the difference of the same average intensities, S_2 is the correlation between the fields along the two axes and finally S_3 is the correlation between the field along one axis and the field along the other retarded by one quarter of a period of the osciallation. By convention the x axis is often taken along the horizontal physical direction; from now on we will often use the term “horizontal” instead of “along the x axis” and “vertical” instead of “along the y axis”.

If the light under study is a purely harmonic plane wave, we have $E_x = E_{0x}\cos(z - ct + \varphi_x)$, $E_y = E_{0y}\cos(z - ct + \varphi_y)$ and equations 4.20 through 4.23 reduce to the commonly presented form of the Stokes Polarization Parameters for a *totally polarized* light (except for a $\frac{1}{2}$ proportionality factor):

$$S_0 = E_{0x}^2 + E_{0y}^2 \tag{4.24}$$

$$S_1 = E_{0x}^2 - E_{0y}^2 \tag{4.25}$$

$$S_2 = 2E_{0x}E_{0y}\cos(\delta) \tag{4.26}$$

$$S_3 = 2E_{0x}E_{0y}\sin(\delta) \tag{4.27}$$

The first parameter S_0 is obviously the total intensity of the light and can be measured by a photodetector. It is customary to set it to one and to express the other components as their actual ratio to S_0.

S_1 represents the balance between the horizontal and the vertical linearly polarized component of the light: it is equal to 1 if the light is totally horizontally polarized and to -1 if it is vertically polarized. Its value can be computed by measuring the intensities through an horizontal and a vertical polarizer and subtracting the two values.

Likewise S_2 represents the difference between linearly polarized portions of the light at $+45°$ and $-45°$. Though this interpretation is not as obvious as the first two, if we remember the polarization ellipse it becomes apparent that $S_2 = \pm 1$ when $E_x = E_y$ and $\delta = 0 + n \cdot \frac{\pi}{2}$, ie when the light is linearly polarized at $\pm 45°$. Its value can be accessed in a similar manner as S_1 using a rotating polarizer at $\pm 45°$.

Finally S_3 represents the portion of the light that is circularly polarized, as shown once again by the polarization ellipse. To measure it one can send the light first through a quarter-wave plate, then through a rotating linear polarizer oriented at $+45°$ and $-45°$.

The validity of the measurement methods given here will be justified in section 4.5.4.

4.4.2 Stokes vectors and their properties

4.4.2.1 Definition

For ease of use the Stokes parameters are often presented as a vector named the *Stokes Vector* $\mathbf{S} = [S_0; S_1; S_2; S_3]$. For instance, the Stokes vectors for some of the remarkable states polarization are:

$$\begin{array}{cc} \text{Linear horizontal polarization} & \text{Linear vertical polarization} \\ \begin{bmatrix} 1 \\ 1 \\ 0 \\ 0 \end{bmatrix} & \begin{bmatrix} 1 \\ -1 \\ 0 \\ 0 \end{bmatrix} \\ \\ \text{Linear polarization at } +45^\circ & \text{Linear polarization at -45}^\circ \\ \begin{bmatrix} 1 \\ 0 \\ 1 \\ 0 \end{bmatrix} & \begin{bmatrix} 1 \\ 0 \\ -1 \\ 0 \end{bmatrix} \\ \\ \text{Right circular polarization} & \text{Left circular polarization} \\ \begin{bmatrix} 1 \\ 0 \\ 0 \\ 1 \end{bmatrix} & \begin{bmatrix} 1 \\ 0 \\ 0 \\ -1 \end{bmatrix} \end{array}$$

4.4.2.2 Physically realizable Stokes vectors

For totally uncorrelated E_x and E_y, S_1 through S_3 from equations 4.21 through 4.23 will be null and this state represents a totally unpolarized light [44, p. 51]. If in contrast the light is totally polarized, equations

4.25-4.27 yield:

$$\begin{aligned} S_1^2 + S_2^2 + S_3^2 &= (E_x^2 - E_y^2)^2 + 4E_x^2E_y^2\cos(\delta) + 4E_x^2E_y^2\sin(\delta) \\ &= S_0^2 \end{aligned}$$

Any partially polarized state will lie in between these values and so a Stokes vector represents a physically possible state of polarization if:

$$S_1^2 + S_2^2 + S_3^2 \leq S_0^2$$

4.4.2.3 Sum of Stokes vectors

If we superpose two *uncorrelated* beams of light of Stokes parameters $S_i^{(1)}$ and $S_i^{(2)}$, the resulting time average of the square of the electric field along x will be equal to:

$$\begin{aligned} \left\langle E_x^2 \right\rangle &= \left\langle (E_x^{(1)} + E_x^{(2)})^2 \right\rangle \\ &= \left\langle (E_x^{(1)})^2 \right\rangle + \left\langle (E_x^{(2)})^2 \right\rangle + 2\left\langle E_x^{(1)}E_x^{(2)} \right\rangle \\ &= \left\langle (E_x^{(1)})^2 \right\rangle + \left\langle (E_x^{(2)})^2 \right\rangle \end{aligned}$$

which results in the $S_0$and S_1 Stokes parameters of the resulting beam being equal to the sum of the $S_0$and S_1 Stokes parameters of the two original beams. The same result can be demonstrated for S_2 and S_3, and the consequence is a very important and useful property of Stokes vectors: *the Stokes vector of the sum of two beams is the sum of their individual Stokes vectors.*

4.4.3 Degree of polarization

If we now apply the Stokes representation to our opening example, two linearly polarized beams, one horizontal and the second vertical, give a resulting beam with Stokes vector:

$$\begin{bmatrix} S_0 \\ S_1 \\ S_2 \\ S_3 \end{bmatrix} = \begin{bmatrix} 1 \\ 1 \\ 0 \\ 0 \end{bmatrix} + \begin{bmatrix} 1 \\ -1 \\ 0 \\ 0 \end{bmatrix} = \begin{bmatrix} 2 \\ 0 \\ 0 \\ 0 \end{bmatrix}$$

We see that this beam cannot be described as having linearly or circularly polarized components. We define the *degree of polarization* as the ratio of "polarized light" (in any of the three possible states) to the total intensity [46, p. 71]:

$$P = \frac{\sqrt{S_1^2 + S_2^2 + S_3^2}}{S_0} \tag{4.28}$$

When a Stokes vector represents a *totally polarized* light, such as a linear or circular polarization, then $P = 1$; if the light is *unpolarized* then $P = 0$; any value in between identifies a *partially polarized* light.

4.5 Computing changes in polarization: the Mueller Matrix

4.5.1 Definition

As we have seen, the Stokes coefficients can be conveniently arranged as a vector. It is then natural to define a transfer matrix between any two Stokes vectors:

$$\begin{bmatrix} S'_0 \\ S'_1 \\ S'_2 \\ S'_3 \end{bmatrix} = \begin{bmatrix} m_{00} & m_{01} & m_{02} & m_{03} \\ m_{10} & m_{11} & m_{12} & m_{13} \\ m_{20} & m_{21} & m_{22} & m_{23} \\ m_{30} & m_{31} & m_{32} & m_{33} \end{bmatrix} \cdot \begin{bmatrix} S_0 \\ S_1 \\ S_2 \\ S_3 \end{bmatrix} \tag{4.29}$$

This 4×4 components transfer matrix is called a *Mueller Matrix.* The effect of any optical system that acts on polarization in a *linear* manner can be represented by a Mueller matrix. Since we only consider linear systems, the coefficients of the matrix are independent from the input or output parameters. This tool enables simple and efficient calculation of the evolution of a state of polarization as light passes through an optical system.

4.5.2 The Mueller matrices of usual polarizing elements

We can now apply the Mueller matrix formalism to the polarizing elements we presented in section 4.3. Moreover we introduce a new type of element: since the Stokes formalism can represent partially polarized light, we define a *depolarizer* that can lower the degree of polarization.

4.5.2.1 The Mueller Matrix of a Waveplate

As seen in section 4.3.1 a waveplate adds a phase difference $\triangle\varphi$ between E_x and E_y thus the only difference between the input and output Stokes vectors will be the phase in S_2 and S_3. Using equations 4.24-4.27 and 4.29 we have:

$$\begin{bmatrix} S_0 \\ S_1 \\ 2E_xE_y\cos(\delta+\triangle\varphi) \\ 2E_xE_y\sin(\delta+\triangle\varphi) \end{bmatrix} = \begin{bmatrix} m_{00} & m_{01} & m_{02} & m_{03} \\ m_{10} & m_{11} & m_{12} & m_{13} \\ m_{20} & m_{21} & m_{22} & m_{23} \\ m_{30} & m_{31} & m_{32} & m_{33} \end{bmatrix} \cdot \begin{bmatrix} S_0 \\ S_1 \\ 2E_xE_y\cos(\delta) \\ 2E_xE_y\sin(\delta) \end{bmatrix}$$

The fact that S_0 and S_1 are not modified and that the equation must be verified for any value they may take directly implies that $m_{00} = m_{11} = 1$ and that all other coefficients but m_{22}, m_{23}, m_{32}, and m_{33} are null. We are left with the two equations:

$$\begin{aligned} m_{22}\cos(\delta) + m_{23}\sin(\delta) &= \cos(\delta+\triangle\varphi) = \cos(\delta)\cos(\triangle\varphi) - \sin(\delta)\sin(\triangle\varphi) \\ m_{32}\cos(\delta) + m_{33}\sin(\delta) &= \sin(\delta+\triangle\varphi) = \cos(\delta)\sin(\triangle\varphi) + \sin(\delta)\cos(\triangle\varphi) \end{aligned}$$

and we identify directly $m_{22} = m_{33} = \cos(\triangle\varphi)$, $m_{23} = -\sin(\triangle\varphi)$ and $m_{32} = \sin(\triangle\varphi)$. The Mueller matrix of a waveplate is thus:

$$\mathbf{M}_{WP}(\triangle\varphi) = \begin{bmatrix} 1 & 0 & 0 & 0 \\ 0 & 1 & 0 & 0 \\ 0 & 0 & \cos(\triangle\varphi) & -\sin(\triangle\varphi) \\ 0 & 0 & \sin(\triangle\varphi) & \cos(\triangle\varphi) \end{bmatrix} \tag{4.30}$$

In section 4.3.1 we mentioned two remarkable wave plates: the quarter-wave plate with retardance $\Delta\phi = \pi/2$ and the half-wave plate with $\Delta\phi = \pi$. Their Mueller matrices are respectively:

$$\mathbf{M}_{QWP} = \begin{bmatrix} 1 & 0 & 0 & 0 \\ 0 & 1 & 0 & 0 \\ 0 & 0 & 0 & -1 \\ 0 & 0 & 1 & 0 \end{bmatrix} \tag{4.31}$$

for the quarter-wave plate, and:

$$\mathbf{M}_{WP}\left(\triangle\varphi\right)=\begin{bmatrix}1 & 0 & 0 & 0\\ 0 & 1 & 0 & 0\\ 0 & 0 & -1 & 0\\ 0 & 0 & 0 & -1\end{bmatrix} \tag{4.32}$$

for the half-wave plate.

4.5.2.2 The Mueller Matrix of a Diattenuator

A diattenuator absorbs a fraction of the input electric field along each of its axes. If one of the axes totally absorbs the field, the element is called an *ideal linear polarizer* as it only lets totally polarized linear light through. Taking the *amplitude transmission coefficients* along axes x and y of the diattenuator as p_x and p_y, we have $E'_x = p_x E_x$ and $E'_y = p_y E_y$ hence:

$$\begin{bmatrix}p_x^2E_x^2+p_y^2E_y^2\\ p_x^2E_x^2-p_y^2E_y^2\\ 2p_xp_yE_xE_y\cos\left(\delta\right)\\ 2p_xp_yE_xE_y\sin\left(\delta\right)\end{bmatrix}=\begin{bmatrix}m_{00} & m_{01} & m_{02} & m_{03}\\ m_{10} & m_{11} & m_{12} & m_{13}\\ m_{20} & m_{21} & m_{22} & m_{23}\\ m_{30} & m_{31} & m_{32} & m_{33}\end{bmatrix}\cdot\begin{bmatrix}E_x^2+E_y^2\\ E_x^2-E_y^2\\ 2E_xE_y\cos\left(\delta\right)\\ 2E_xE_y\sin\left(\delta\right)\end{bmatrix}$$

which resolves to the Mueller Matrix of a diattenuator:

$$\mathbf{M}_{diat}\left(p_x,p_y\right)=\frac{1}{2}\cdot\begin{bmatrix}p_x^2+p_y^2 & p_x^2-p_y^2 & 0 & 0\\ p_x^2-p_y^2 & p_x^2+p_y^2 & 0 & 0\\ 0 & 0 & 2p_xp_y & 0\\ 0 & 0 & 0 & 2p_xp_y\end{bmatrix} \tag{4.33}$$

In the case of an ideal *horizontal* linear polarizer this matrix reduces to $\mathbf{M}_{pol}=\mathbf{M}_{diat}\left(p_x,0\right)$ ie:

$$\mathbf{M}_{polh}=\frac{p_x^2}{2}\cdot\begin{bmatrix}1 & 1 & 0 & 0\\ 1 & 1 & 0 & 0\\ 0 & 0 & 0 & 0\\ 0 & 0 & 0 & 0\end{bmatrix} \tag{4.34}$$

and in the case of an ideal *vertical* linear polarizer to:

$$\mathbf{M}_{polv} = \frac{p_y^2}{2} \cdot \begin{bmatrix} 1 & -1 & 0 & 0 \\ -1 & 1 & 0 & 0 \\ 0 & 0 & 0 & 0 \\ 0 & 0 & 0 & 0 \end{bmatrix} \tag{4.35}$$

4.5.2.3 The Mueller Matrix of a Depolarizer

We define a *depolarizer* as an element that decreases the degree of polarization $P = \sqrt{S_1^2 + S_2^2 + S_3^2}/S_0$. In general a depolarizer could also modify the relative amount of light in any of the three states represented by S_1 through S_3, but we restrict ourselves to a *pure depolarizer* that only lowers P without modifying the ratios S_1/S_2, S_1/S_3, S_2/S_3 or the total intensity S_0. A *depolarization ratio* α, $0 \leq \alpha \leq 1$ results in:

$$\begin{aligned} P' &= \alpha P \\ \sqrt{S'^2_1 + S'^2_2 + S'^2_3}/S_0 &= \alpha\sqrt{S_1^2 + S_2^2 + S_3^2}/S_0 \\ \sqrt{S'^2_1 + S'^2_2 + S'^2_3} &= \sqrt{\alpha^2 S_1^2 + \alpha^2 S_2^2 + \alpha^2 S_3^2} \end{aligned}$$

which in turns implies the Mueller Matrix for a pure depolarizer:

$$\mathbf{M}_{depol}(\alpha) = \begin{bmatrix} 1 & 0 & 0 & 0 \\ 0 & \alpha & 0 & 0 \\ 0 & 0 & \alpha & 0 \\ 0 & 0 & 0 & \alpha \end{bmatrix} \tag{4.36}$$

In the case of a perfect depolarizer we have $\alpha = 0$ and (4.36) reduces to a matrix full of zeros except for $m_{00} = 1$.

4.5.3 The Mueller Matrix of a rotated optical element

The Mueller matrices we have defined in 4.5.2 describe optical elements with a fixed orientation. In practice a polarizer or a waveplate is often mounted so that it can freely rotate about its optical axis, and it is desirable to describe the behaviour of such rotated elements.

Let us consider an optical element described by a Mueller matrix **M** in the path of a beam of light with Stokes vector **S**. The output Stokes vector is then $\mathbf{S}' = \mathbf{M} \cdot \mathbf{S}$. Consider now that the optical element is rotated by an angle θ: the Mueller matrix **M** does not describe it anymore; but if we - mathematically - apply a rotation of angle $-\theta$ to the system consisting of the input beams and the optical element, the resulting system corresponds to the non rotated optical element now acting on an input beam with polarization rotated by $-\theta$; this is exactly equivalent to a projection of the polarization along the reference axes of the optical element. Applied directly to the electric field of the light, a rotation of angle θ is described by the well known rotation matrix for a 2D vector:

$$\begin{bmatrix} Er_x \\ Er_y \end{bmatrix} = \begin{bmatrix} \cos(\theta) & -\sin(\theta) \\ \sin(\theta) & \cos(\theta) \end{bmatrix} \cdot \begin{bmatrix} E_x \\ E_y \end{bmatrix} = \begin{bmatrix} E_x \cos(\theta) - E_y \sin(\theta) \\ E_x \sin(\theta) + E_y \cos(\theta) \end{bmatrix}$$

which in turn, when combined with 4.24-4.27 and4.29 gives us the Mueller matrix for a rotator:

$$\mathbf{M}_{rot}(\theta) = \begin{bmatrix} 1 & 0 & 0 & 0 \\ 0 & \cos(2\theta) & -\sin(2\theta) & 0 \\ 0 & \sin(2\theta) & \cos(2\theta) & 0 \\ 0 & 0 & 0 & 1 \end{bmatrix} \tag{4.37}$$

We can then compute the effect of a rotated element through the following steps: decompose the polarization of the incoming beam along the main axes of the rotated element, apply the Mueller matrix of the non-rotated element to this state of polarization, and finally project the resulting state back onto the original reference axes. The whole procedure is described by:

$$\mathbf{S}' = \mathbf{M}_{rot}(\theta) \cdot \mathbf{M} \cdot \mathbf{M}_{rot}(-\theta) \cdot \mathbf{S} \tag{4.38}$$

which produces a direct expression for the Mueller matrix of a rotated optical element.

Carrying out the matrix multiplications in equation 4.38 we get the

Mueller matrix of a waveplate with retardance $\triangle\varphi$ rotated by an angle θ:

$$\mathbf{M}_{WP}\left(\triangle\varphi,\theta\right) =$$

$$\begin{bmatrix} 1 & 0 & 0 & 0 \\ 0 & \cos^2\left(2\theta\right)+\cos\left(\triangle\varphi\right)\sin^2\left(2\theta\right) & \left(1-\cos\left(\triangle\varphi\right)\right)\cos\left(2\theta\right)\sin\left(2\theta\right) & \sin\left(\triangle\varphi\right)\sin\left(2\theta\right) \\ 0 & \left(1-\cos\left(\triangle\varphi\right)\right)\cos\left(2\theta\right)\sin\left(2\theta\right) & \cos\left(\triangle\varphi\right)\cos^2\left(2\theta\right)+\sin^2\left(2\theta\right) & -\sin\left(\triangle\varphi\right)\cos\left(2\theta\right) \\ 0 & -\sin\left(\triangle\varphi\right)\sin\left(2\theta\right) & \sin\left(\triangle\varphi\right)\cos\left(2\theta\right) & \cos\left(\triangle\varphi\right) \end{bmatrix} \tag{4.39}$$

and of a diattenuator rotated by an angle θ:

$$\mathbf{M}_{diat}\left(p_x,p_y,\theta\right) =$$

$$\frac{1}{2}\left[\begin{array}{cccc} p_x^2+p_y^2 & \left(p_x^2-p_y^2\right)\cos\left(2\theta\right) & \left(p_x^2-p_y^2\right)\sin\left(2\theta\right) & 0 \\ \left(p_x^2-p_y^2\right)\cos\left(2\theta\right) & \left(p_x^2+p_y^2\right)\cos^2\left(2\theta\right)+2p_xp_y\sin^2\left(2\theta\right) & \left(p_x-p_y\right)^2\cos\left(2\theta\right)\sin\left(2\theta\right) & 0 \\ \left(p_x^2-p_y^2\right)\sin\left(2\theta\right) & \left(p_x-p_y\right)^2\cos\left(2\theta\right)\sin\left(2\theta\right) & \left(p_x^2+p_y^2\right)\sin^2\left(2\theta\right)+2p_xp_y\cos^2\left(2\theta\right) & 0 \\ 0 & 0 & 0 & 2p_xp \end{array}\right. \tag{4.40}$$

which in turns reduces for an ideal horizontal polarizer ($p_x = 1$, $p_y = 0$) to:

$$\mathbf{M}_{polh}\left(\theta\right) = \frac{1}{2}\begin{bmatrix} 1 & \cos\left(2\theta\right) & \sin\left(2\theta\right) & 0 \\ \cos\left(2\theta\right) & \cos^2\left(2\theta\right) & \cos\left(2\theta\right)\sin\left(2\theta\right) & 0 \\ \sin\left(2\theta\right) & \cos\left(2\theta\right)\sin\left(2\theta\right) & \sin^2\left(2\theta\right) & 0 \\ 0 & 0 & 0 & 0 \end{bmatrix} \tag{4.41}$$

4.5.4 Measurement of the Stokes parameters

Now that we have an efficient tool to perform polarization calculus, we can apply it to show how the Stokes parameters can be experimentally measured. The method presented here is far from being the best, or even the simplest, method to measure Stokes parameters, but it serves to illustrate the physical meaning we gave to each of them in section 4.4.1.

Let us consider a beam of light of unknown polarization state $\mathbf{S} = [S_0\ S_1\ S_2\ S_3]$. The intensity observed through an ideal horizontal linear polarizer is computed through:

$$\frac{1}{2}\cdot\begin{bmatrix}1&1&0&0\\1&1&0&0\\0&0&0&0\\0&0&0&0\end{bmatrix}\cdot\begin{bmatrix}S_0\\S_1\\S_2\\S_3\end{bmatrix}=\frac{1}{2}\begin{bmatrix}S_0+S_1\\S_0+S_1\\0\\0\end{bmatrix}$$

and found to be equal to $I_1 = \frac{1}{2}(S_0 + S_1)$; likewise, an ideal vertical linear polarizer yields an intensity $I_2 = \frac{1}{2}(S_0 - S_1)$. We directly obtain the first two Stokes parameters by addition and subtraction:

$$\begin{aligned}S_0 &= I_1 + I_2\\S_1 &= I_1 - I_2\end{aligned}$$

If the polarizer is now rotated first at +45° and then at −45° we obtain the two intensities $I_3 = \frac{1}{2}(S_0 + S_2)$ and $I_4 = \frac{1}{2}(S_0 - S_2)$ and straightforwardly:

$$S_2 = I_3 - I_4$$

Finally we now place a quarter-wave plate in front the polarizer at +45°:

$$\frac{1}{2}\cdot\begin{bmatrix}1&0&1&0\\0&0&0&0\\1&0&1&0\\0&0&0&0\end{bmatrix}\cdot\begin{bmatrix}1&0&0&0\\0&1&0&0\\0&0&0&-1\\0&0&1&0\end{bmatrix}\cdot\begin{bmatrix}S_0\\S_1\\S_2\\S_3\end{bmatrix}=\frac{1}{2}\begin{bmatrix}S_0-S_3\\0\\S_0-S_3\\0\end{bmatrix}$$

to obtain $I_5 = \frac{1}{2}(S_0 - S_3)$ and then rotate the polarizer to −45° which yields $I_6 = \frac{1}{2}(S_0 + S_3)$. S_3 is then given by:

$$S_3 = I_6 - I_5$$

This method of measuring the Stokes parameters clearly shows the physical meaning of each one: S_0 is the total intensity of the light, S_1 represents the fraction of the light that is predominantly either horizontally or vertically linearly polarized, S_2 is the same for linearly polarized light oriented at ±45°, and finally S_3 is the fraction of light that is circularly polarized: the quarter-wave plate transforms the circular component into linearly polarized light at ±45° and the inclined polarizers measures it, the whole system acting as a circular polarizer.

These four measurementes are sufficient to completely determine the state of polarization.

Chapter 5

Polarized light in transparent media

This chapter deals with the interaction of polarized light with transparent media and focuses on two particular points: birefringence, its causes and its effects, and reflection/transmission at an interface.

5.1 The notion of linear birefringence

We have seen in the wave equation 4.12 that the phase speed of light depends on physical properties of the material, namely its permittivity ε and permeability μ that combine into the refractive index $n = c_0/c = \sqrt{\frac{\varepsilon\mu}{\varepsilon_0\mu_0}}$. The electric field being of vectorial nature, it is sensitive to the refractive index along its orientation. It is then interesting to study the scenario where the index is not the same along **i** and **j** the two axes perpendicular to the direction of propagation of light: the two components of the electric field along each axis will "see" two different indexes of refraction. This is known as *linear birefringence* and a material that displays this property is called *birefringent*.

Equation 4.17 shows that after traveling through a dielectric material of thickness z and refractive index n the electric field of a propagating wave of pulsation ω has acquired a phase equal to $\triangle\varphi = kz = \frac{\omega}{c_0}nz = \frac{2\pi}{\lambda_0}nz$. If the refractive indexes along the two axes **i** and **j** are n_1 and n_2, the electric field after the birefringent material is:

$$\mathbf{E}(z,t) = (E_{0x}e^{i(\varphi_x+\triangle\varphi_1)}\mathbf{i} + E_{0y}e^{i(\varphi_y+\triangle\varphi_2)}\mathbf{j})e^{i(kz-\omega t)}$$

and the phase difference between the two components is:

$$\triangle\varphi = \frac{2\pi}{\lambda_0}\left(n_1 - n_2\right) z = \frac{2\pi}{\lambda_0}\triangle n \cdot z$$

In the end, a birefringent material has the effect of adding a phase difference $\triangle\varphi$ between the two components of the electric field. The axis with the highest refractive index is known as the *slow axis* of the material, as the phase speed is the slowest of the two. Likewise, the axis with the lowest refractive index is the *fast axis* of the material.

Since the orientation of the electric field depends on the *relative*, and not absolute, phases of the two components, the effect of a birefringent material with birefringence Δn and thickness e is exactly that of a waveplate as described in section 4.3.1 and it can be modelized by the Mueller matrix 5.1:

$$\mathbf{M}_{biref}\left(\triangle\varphi = \frac{2\pi}{\lambda_0}\triangle n \cdot e\right) = \begin{bmatrix} 1 & 0 & 0 & 0 \\ 0 & 1 & 0 & 0 \\ 0 & 0 & \cos\left(\frac{2\pi}{\lambda_0}\triangle n \cdot e\right) & -\sin\left(\frac{2\pi}{\lambda_0}\triangle n \cdot e\right) \\ 0 & 0 & \sin\left(\frac{2\pi}{\lambda_0}\triangle n \cdot e\right) & \cos\left(\frac{2\pi}{\lambda_0}\triangle n \cdot e\right) \end{bmatrix} \tag{5.1}$$

Naturally birefringent materials, such as quartz, are often used in practical implementations of wave plates by cutting them to the desired thickness. For instance, a quarterwave-plate made of quartz, which has a birefringence of $\Delta n \approx 9.01 \times 10^{-3}$ at $\lambda_0 = 670.8\,nm$ [47], would have a thickness of $18.6\,\mu m$.

In opposition to *linear* birefringence, some material present a different refractive index to right and left circular polarizations. This is known as *circular birefringence* and its effect on a linear polarization is simply to rotate its orientation angle. This effect is not used in the rest of this document, and we only mention it succinctly to justify the “linear” adjective we associated to birefringence.

5.2 Stress-induced linear birefringence : the piezo-optic effect

5.2.1 The dielectric tensor

In section 4.1 we stated that in an *isotropic* dielectric media the electric field **E** and the electric displacement field **D** are linked by the dielectric constant ε through the equation $\mathbf{D}(\mathbf{r},t) = \varepsilon\mathbf{E}(\mathbf{r},t)$. If the material is *electrically anisotropic*, we can no longer assume that **D** and **E** are collinear; if we still admit that there exists a linear relationships between the components [45, p. 790], they are now linked by the set of equations:

$$\begin{cases} D_x &= \varepsilon_{xx}E_x + \varepsilon_{xy}E_y + \varepsilon_{xz}E_z \\ D_y &= \varepsilon_{yx}E_x + \varepsilon_{yy}E_y + \varepsilon_{yz}E_z \\ D_z &= \varepsilon_{zx}E_x + \varepsilon_{zy}E_y + \varepsilon_{zz}E_z \end{cases} \tag{5.2}$$

from which we define the *dielectric tensor* ϵ:

$$\epsilon = \begin{bmatrix} \varepsilon_{xx} & \varepsilon_{xy} & \varepsilon_{xz} \\ \varepsilon_{yx} & \varepsilon_{yy} & \varepsilon_{yz} \\ \varepsilon_{zx} & \varepsilon_{zy} & \varepsilon_{zz} \end{bmatrix}$$

that links **D** to **E** through $\mathbf{D}(\mathbf{r},t) = \epsilon\mathbf{E}(\mathbf{r},t)$. It can be shown that the dielectric tensor is always a symmetric tensor, ie that is $\varepsilon_{ij} = \varepsilon_{ji}$ $(i, j = x, y, z)$, which in turns implies that there always exists a system of coordinates $(\hat{x}, \hat{y}, \hat{z})$, in general different from (x, y, z), in which ϵ is diagonal [45, pp. 791,792]:

$$\hat{\epsilon} = \begin{bmatrix} \varepsilon_{\hat{x}} & 0 & 0 \\ 0 & \varepsilon_{\hat{y}} & 0 \\ 0 & 0 & \varepsilon_{\hat{z}} \end{bmatrix}$$

$\varepsilon_{\hat{x}}, \varepsilon_{\hat{y}}, \varepsilon_{\hat{z}}$ are the *principal dielectric constants*, and and in this basis the system 5.2 can be rewritten as:

$$\begin{cases} D_{\hat{x}} &= \varepsilon_{\hat{x}}E_{\hat{x}} \\ D_{\hat{y}} &= \varepsilon_{\hat{y}}E_{\hat{y}} \\ D_{\hat{z}} &= \varepsilon_{\hat{z}}E_{\hat{z}} \end{cases}$$

The behaviour of the components of the electric field along each of the three principal axes are now independent from each other and can be treated separately: each component of the electric field interacts with a different dielectric constant, which results for a non-magnetic material in each component interacting with a different index of refraction $n_{\hat{i}} = 1/\sqrt{\varepsilon_{\hat{i}}/\varepsilon_0}$. We drop the " ˆ " symbol from now on and always work in the principal basis unless specified otherwise.

5.2.2 The effect of stress on an isotropic dielectric material

We assume that in first approximation the *variation* in the dielectric constant, $\triangle\epsilon$, of a material due to stress is linearly dependent on the local stress. This assumption has been largely verified experimentally over the years since it was first proposed by Pockels (see references [37, 38, 39, 40, 42] for instance). The stress in a material being in general described by a symmetric 3×3 tensor σ [48], that can always be represented as a diagonal tensor in its principal basis just as the dielectric tensor. The two principal bases need not in general be the same, and so σ will be in general linked to $\triangle\epsilon$ through a set of 6×6 coefficients, the *piezo-optic* or *stress-optic* constants p_{ijkl}. In an isotropic dielectric, these 36 components reduce to only two [49] and written in the system of coordinates of the principal stresses we have:

$$\begin{bmatrix} \triangle\varepsilon_{xx} \\ \triangle\varepsilon_{yy} \\ \triangle\varepsilon_{zz} \\ \triangle\varepsilon_{xy} \\ \triangle\varepsilon_{xz} \\ \triangle\varepsilon_{yz} \end{bmatrix} = \begin{bmatrix} p_{11} & p_{12} & p_{12} & 0 & 0 & 0 \\ p_{12} & p_{11} & p_{12} & 0 & 0 & 0 \\ p_{12} & p_{12} & p_{11} & 0 & 0 & 0 \\ 0 & 0 & 0 & \frac{1}{2}(p_{11}-p_{12}) & 0 & 0 \\ 0 & 0 & 0 & 0 & \frac{1}{2}(p_{11}-p_{12}) & 0 \\ 0 & 0 & 0 & 0 & 0 & \frac{1}{2}(p_{11}-p_{12}) \end{bmatrix} \cdot \begin{bmatrix} \sigma_x \\ \sigma_y \\ \sigma_z \\ 0 \\ 0 \\ 0 \end{bmatrix} \tag{5.3}$$

The first result from 5.3 is that $\triangle\varepsilon_{xy} = \triangle\varepsilon_{xz} = \triangle\varepsilon_{yz} = 0$, which means that *for an isotropic material, the principal dielectric directions are the same as the principal stress directions.*

Assuming small variations in the dielectric indices and since in an isotropic material $\varepsilon_x = \varepsilon_y = \varepsilon_z = 1/n^2$, $\triangle\varepsilon_i \sim -2\delta n_i/n^3$ and we obtain the variation of the index of refraction along each direction due to stress:

$$\begin{cases} \delta n_x &= -\frac{1}{2}n^3(p_{11}\sigma_x + p_{12}(\sigma_y + \sigma_z)) \\ \delta n_y &= -\frac{1}{2}n^3(p_{11}\sigma_y + p_{12}(\sigma_x + \sigma_z)) \\ \delta n_z &= -\frac{1}{2}n^3(p_{11}\sigma_z + p_{12}(\sigma_x + \sigma_y)) \end{cases} \tag{5.4}$$

If a plane wave now propagates in such stressed material along the z direction it will see two difference refraction indices $n_x = n - \delta n_x$ and $n_y = n - \delta n_y$ which finally gives an expression of the *stress-induced birefringence in an isotropic material*:

$$\triangle n = n_x - n_y = \frac{1}{2}n^3(p_{11} - p_{12})(\sigma_x - \sigma_y) \tag{5.5}$$

Experimentally we do not often access the piezo-optic constants directly, so the $\frac{1}{2}n^3(p_{11} - p_{12})$ factor is often measured as a constant C called the *piezo-optic coefficient*[1] and the birefringence is $\triangle n = C \cdot (\sigma_x - \sigma_y)$.

5.3 Polarization effects at an interface

When a propagating electromagnetic wave comes in contact with an interface between two dielectric material of different refraction index, the wave is in general split into a *refracted (transmitted) wave* and a *reflected wave.*

To illustrate the reflection and transmission at an interface, consider figure 5.1. An incident plane wave $\mathbf{E}^{(i)}$, here represented as a ray of light that indicates it propagation direction, reaches an interface between two materials of respective refractive indices n_1 and n_2. At the interface $\mathbf{E}^{(i)}$ is split into a transmitted wave $\mathbf{E}^{(t)}$ and a reflected wave $\mathbf{E}^{(r)}$. The plane that contains the incident ray and the normal to the surface is known as the *plane of incidence*, and both the reflected and refracted rays lie in it [45, p. 39].

---

[1] Or sometimes stress-optic coefficient, Brewster constant or elasto-optic coefficient. When referring to the coefficients that link stress to index of refraction, the correct prefix is either stress- or piezo-; elasto- should be reserved when the physical variable one considers is an elongation (strain).

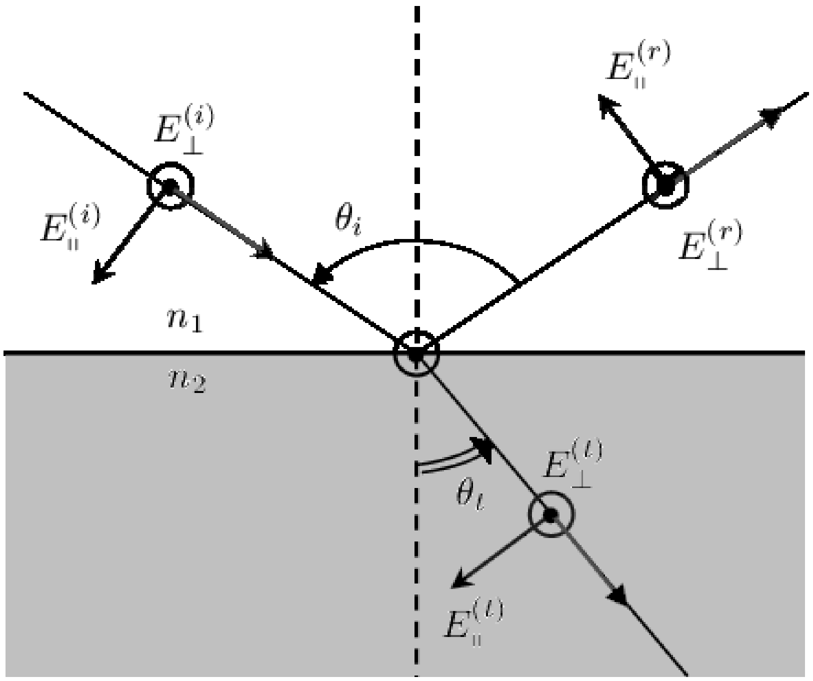

Figure 5.1: Reflection and transmission at an interface.

5.3.1 Snell's law of refraction

The angle the refracted ray makes with the normal to the interface is related to the angle of the incident wave through the law of refraction [45, p. 40]:

$$\sin(\theta_t) = \frac{n_1}{n_2} \sin(\theta_i) \tag{5.6}$$

If $n_2 > n_1$there exists a real angle θ_t for any angle of incidence. On the other hand, if $n_1 > n_2$ there exists a *critical angle* θ_c, found through the equation $\sin(\theta_c) = \frac{n_2}{n_1}$, above which $\frac{n_1}{n_2} \sin(\theta_i) > 1$ and the transmission angle becomes imaginary. In this situation no light is transmitted beyond the interface, and this phenomenon is known as *total internal reflection*.

5.3.2 The Fresnel reflection and transmission coefficients

The behaviour of the transmitted and reflected electric fields are governed by the Fresnel coefficients [45, p. 42]:

$$t_\perp = \frac{E_\perp^{(t)}}{E_\perp^{(i)}} = \frac{2\sin(\theta_t)\cos(\theta_i)}{\sin(\theta_t+\theta_i)} = \frac{2n_1\cos(\theta_i)}{n_1\cos(\theta_i)+n_2\cos(\theta_t)} \tag{5.7}$$

$$t_{\shortparallel} = \frac{E_{\shortparallel}^{(t)}}{E_{\shortparallel}^{(i)}} = \frac{2\sin(\theta_t)\cos(\theta_i)}{\sin(\theta_i+\theta_t)\cos(\theta_i-\theta_t)} = \frac{2n_1\cos(\theta_i)}{n_2\cos(\theta_i)+n_1\cos(\theta_t)} \tag{5.8}$$

$$r_\perp = \frac{E_\perp^{(r)}}{E_\perp^{(i)}} = -\frac{\sin(\theta_i-\theta_t)}{\sin(\theta_i+\theta_t)} = \frac{n_1\cos(\theta_i)-n_2\cos(\theta_t)}{n_1\cos(\theta_i)+n_2\cos(\theta_t)} \tag{5.9}$$

$$r_{\shortparallel} = \frac{E_{\shortparallel}^{(r)}}{E_{\shortparallel}^{(i)}} = \frac{\tan(\theta_i-\theta_t)}{\tan(\theta_i+\theta_t)} = \frac{n_2\cos(\theta_i)-n_1\cos(\theta_t)}{n_2\cos(\theta_i)+n_1\cos(\theta_t)} \tag{5.10}$$

where $E_\perp$ denotes the component of the field *perpendicular to the plane of incidence* and $E_{\shortparallel}$ the component *parallel to the plane of incidence*. These coefficients compute the reflected and transmitted *amplitudes*; one has to square them to obtain the *intensity* coefficients. Only the properties of reflected waves are needed in the rest of this document, and so we focus on the reflection coefficients only.

5.3.2.1 Partial reflection and the Brewster angle

We first consider the case where $n_2 > n_1$. The reflection coefficients are real for any value of the incidence angle, and are plotted on figure 5.2 for both the parallel and perpendicular components of the electric field:

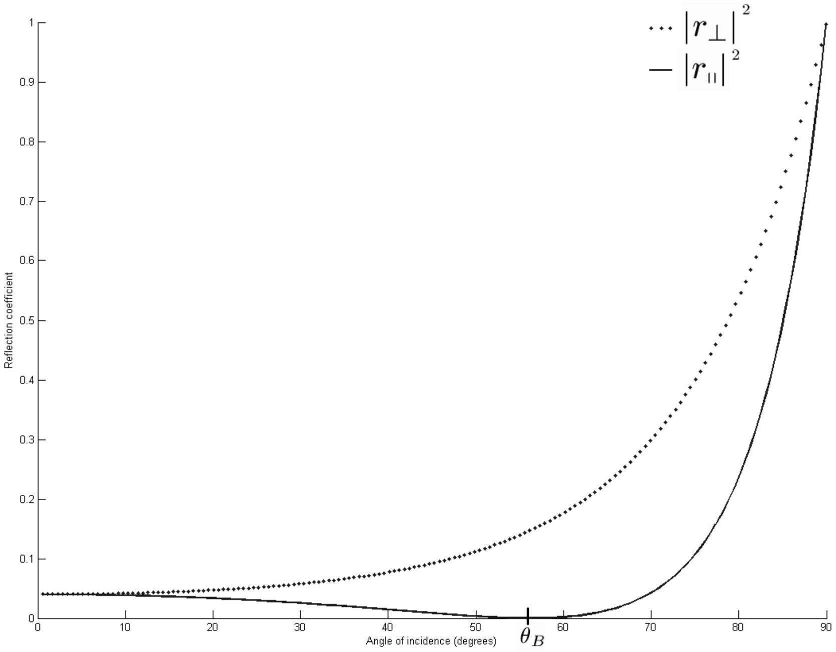

Figure 5.2: Reflection coefficients at a dielectric interface ($n_1 = 1,\ n_2 = 1.5$, approximately an air/glass interface).

An important property of dielectric reflection is immediately apparent: there exists an incidence angle, the *Brewster Angle* θ_B, at which the component of the field parallel to the plan of incidence is not reflected at all. Only a portion of the perpendicular component is reflected, and thus *the reflected light is linearly polarized perpendicularly to the plane of incidence*. Looking at the transmission coefficient, this angle corresponds to a special situation where the reflected and transmitted rays are at a 90° angle with each other: $\theta_t = \theta_r + \frac{\pi}{2} = -\theta_i + \frac{\pi}{2}$ which implies that $\theta_i + \theta_t = \frac{\pi}{2}$ and since $1/\tan(\pi/2) = 0$ we obtain $r_{\shortparallel} = 0$. Injecting this property in the law of refraction 5.6 we obtain:

$$\tan(\theta_B) = \frac{n_2}{n_1} \tag{5.11}$$

and $r_\perp$ becomes:

$$r_\perp(\theta_B) = \frac{n_1^2 - n_2^2}{n_1^2 + n_2^2} \tag{5.12}$$

5.3.2.2 Total reflection

If we now consider the case where $n_1 > n_2$, we have mentioned before that the transmission angle becomes imaginary when $\frac{n_1}{n_2}\sin(\theta_i) > 1$.

We first rewrite the reflection coefficients by expressing $\cos(\theta_t)$ as a function of θ_i by using the trigonometric identity $\cos^2(\theta_t) + \sin^2(\theta_t) = 1$. We obtain:

$$\begin{aligned}\cos(\theta_t) &= \pm\sqrt{1-\sin^2(\theta_t)} = \pm i\sqrt{\sin^2(\theta_t)-1}\\ &= \pm i\sqrt{\left(\frac{n_1}{n_2}\sin(\theta_i)\right)^2 - 1}\end{aligned} \tag{5.13}$$

As long as $\theta_i < \theta_c$ we have $\frac{n_1}{n_2}\sin(\theta_i) < 1$ ie $\left(\frac{n_1}{n_2}\sin(\theta_i)\right)^2 - 1 < 0$, and so $\cos(\theta_t) = \pm(i)^2\sqrt{1-\left(\frac{n_1}{n_2}\sin(\theta_i)\right)^2}$. Since the refracted ray is always inside the second material, we see from figure [fig] that $\cos(\theta_t) > 0$ and from these two relations we deduce that only the negative sign in front of the square root in equation 5.13 corresponds to a physical situation and so:

$$\cos(\theta_t) = -i\sqrt{\left(\frac{n_1}{n_2}\sin(\theta_i)\right)^2 - 1} \tag{5.14}$$

Using a similar argument for the sign of the square root, we can also give an expression of $\cos(\theta_i)$:

$$\cos(\theta_i) = \sqrt{1-\sin^2(\theta_i)} \tag{5.15}$$

We can now rewrite the reflection coefficients using equations 5.10, 5.9, 5.14 and 5.15:

$$r_\perp = \frac{n_1\sqrt{1-\sin^2(\theta_i)} + n_2 i\sqrt{\left(\frac{n_1}{n_2}\sin(\theta_i)\right)^2 - 1}}{n_1\sqrt{1-\sin^2(\theta_i)} - n_2 i\sqrt{\left(\frac{n_1}{n_2}\sin(\theta_i)\right)^2 - 1}} \tag{5.16}$$

$$r_\shortparallel = \frac{n_2\sqrt{1-\sin^2(\theta_i)} + n_1 i\sqrt{\left(\frac{n_1}{n_2}\sin(\theta_i)\right)^2 - 1}}{n_2\sqrt{1-\sin^2(\theta_i)} - n_1 i\sqrt{\left(\frac{n_1}{n_2}\sin(\theta_i)\right)^2 - 1}} \tag{5.17}$$

As long as $\theta_i < \theta_c$, $r_\perp$ and $r_{\parallel}$are real as before. Once $\theta_i > \theta_c$ they become complex numbers, and computing their modulus yields:

$$|r_\perp| = r_\perp r_\perp^* = 1$$
$$|r_{\parallel}| = r_{\parallel} r_{\parallel}^* = 1$$

which indicates that the amplitude of the field of the reflected wave is equal to that of the incident wave: the light is *totally reflected* at the interface as illustrated on figure 5.3.

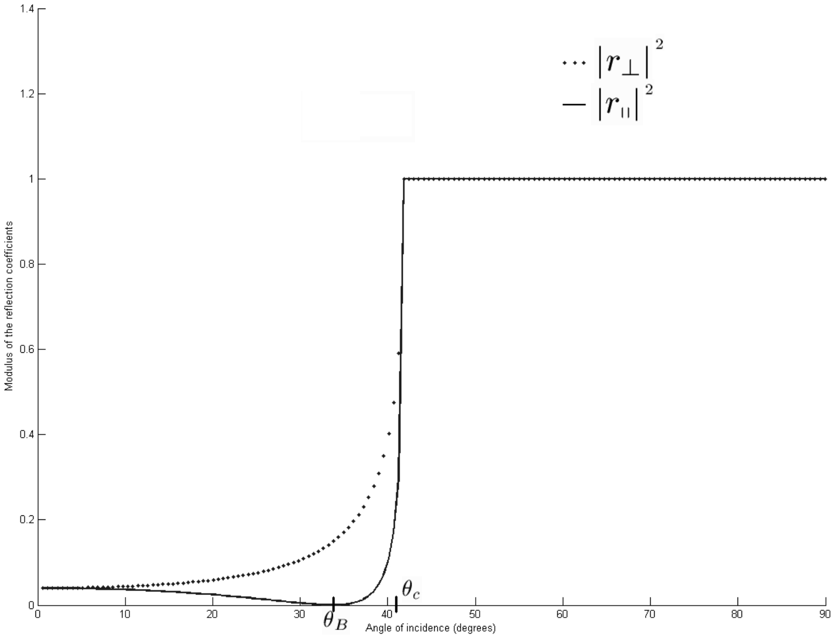

Figure 5.3: Reflection coefficients at an interface with $n_1 = 1.5,\ n_2 = 1)$

In contrast, the arguments of the reflection coefficients are not zero and thus a total internal reflection adds a phase shift to each component of the field. To find the phase shift on each component we write the reflection coefficients in their polar forms:

$$r_\perp = |r_\perp|\, e^{i\varphi_\perp}$$
$$r_{\parallel} = |r_{\parallel}|\, e^{i\varphi_{\parallel}}$$

with $\varphi_\perp$ and $\varphi_{\shortparallel}$ defined by [45, p. 52]:

$$\tan(\frac{1}{2}\varphi_\perp) = -\frac{\sqrt{\sin^2(\theta_i) - \left(\frac{n_2}{n_1}\right)^2}}{\cos(\theta_i)}$$
$$\tan(\frac{1}{2}\varphi_{\shortparallel}) = -\frac{\sqrt{\sin^2(\theta_i) - \left(\frac{n_2}{n_1}\right)^2}}{\left(\frac{n_2}{n_1}\right)^2\cos(\theta_i)}$$

Since polarization effects arise from phase differences between the two components of the electric field, we express the phase difference $\delta_r = \varphi_\perp - \varphi_{\shortparallel}$ resulting from a total internal reflexion as:

$$\tan(\frac{1}{2}\delta_r) = -\frac{\cos(\theta_i)\sqrt{\sin^2(\theta_i) - \left(\frac{n_2}{n_1}\right)^2}}{\sin^2(\theta_i)} \tag{5.18}$$

which we plot on figure 5.4.

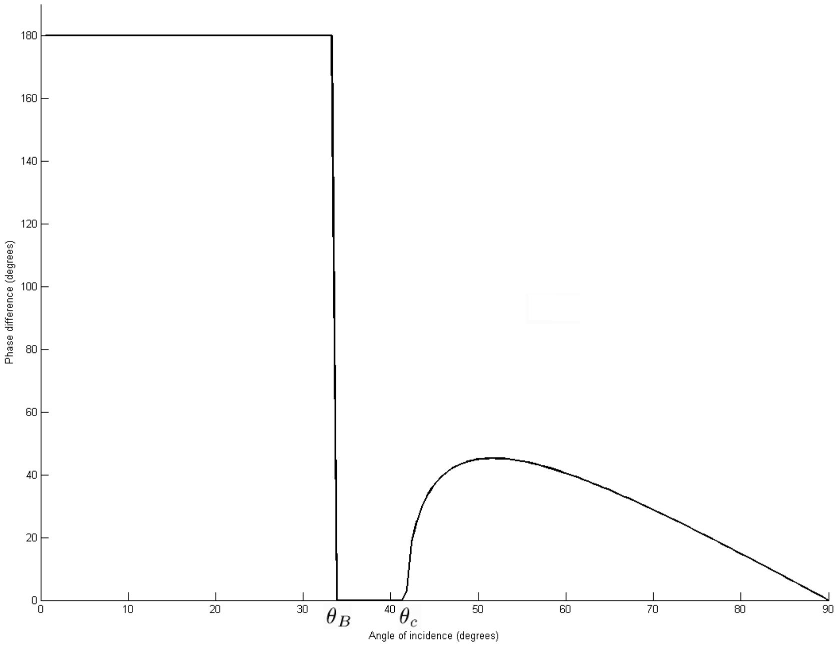

Figure 5.4: Phase difference between the two components of the field after a reflection ($n_1 = 1.5,\ n_2 = 1$).

5.3.3 The Mueller matrix of a reflection

We now use the tools of section 4.5 to modelize the effects of a reflection at an interface in terms of its effects on polarization.

5.3.3.1 The Mueller matrix of a partial reflection

We have seen that as long as the incidence angle is below the critical angle the reflexion coefficients are real. In this case a different proportion of each component of the field is transmitted, and as such a partial reflection behave exactly as a diattenuator [50]. We recall the Mueller matrix from section 4.5.2.2, and taking $p_x = r_\perp$ and $p_y = r_\shortparallel$ as defined in equations 5.9 and 5.10

we obtain:

$$\mathbf{M}_{pr}\left(n_1, n_2, \theta_i < \theta_c\right) = \frac{1}{2} \cdot \begin{bmatrix} r_\perp^2 + r_\shortparallel^2 & r_\perp^2 - r_\shortparallel^2 & 0 & 0 \\ r_\perp^2 - r_\shortparallel^2 & r_\perp^2 + r_\shortparallel^2 & 0 & 0 \\ 0 & 0 & 2r_\perp r_\shortparallel & 0 \\ 0 & 0 & 0 & 2r_\perp r_\shortparallel \end{bmatrix} \tag{5.19}$$

At the Brewster angle we have $r_\shortparallel = 0$ and $r_\perp = \frac{n_1^2 - n_2^2}{n_1^2 + n_2^2}$, which yields:

$$\mathbf{M}_{pr}\left(n_1, n_2, \theta_B\right) = \frac{1}{2} \cdot \left(\frac{n_1^2 - n_2^2}{n_1^2 + n_2^2}\right)^2 \cdot \begin{bmatrix} 1 & 1 & 0 & 0 \\ 1 & 1 & 0 & 0 \\ 0 & 0 & 0 & 0 \\ 0 & 0 & 0 & 0 \end{bmatrix} \tag{5.20}$$

and we verify that indeed a reflection at this particular angle acts as a linear polarizer.

5.3.3.2 The Mueller matrix of a total internal reflection

Above the critical angle, the reflection coefficients become complex with an unitary amplitude and an argument $\delta_r = \varphi_\perp - \varphi_\shortparallel$ as defined in equation 5.18. A pure phase shift is exactly the effect of a waveplate as defined in section 4.5.2.1 and thus the equivalent Mueller matrix for a total reflection is:

$$\mathbf{M}_{tr}\left(n_1, n_2, \theta_i > \theta_c\right) = \begin{bmatrix} 1 & 0 & 0 & 0 \\ 0 & 1 & 0 & 0 \\ 0 & 0 & \cos\left(\delta_r\right) & -\sin\left(\delta_r\right) \\ 0 & 0 & \sin\left(\delta_r\right) & \cos\left(\delta_r\right) \end{bmatrix} \tag{5.21}$$

Part III

Piezo-optic Pressure Sensor

Introduction

After having presented both the commercial and scientific environment the present work fits in as well as the theoretical tools that are going to be used, we now enter into a more detailed description of the proposed piezo-optic pressure sensor.

Chapter 6 presents the conceptual design of our sensor. We start by exposing the underlying idea, the various environmental and commercial constraints and the resulting expected performances of the sensor. A critical look at the initial design leads to the highlighting of a few keys points that can be modified in order to improve the overall quality of the proposed sensor. Each problem is analyzed and solved to result in a refined proposal. The final concept uses an original approach, different from the one usually seen in polarimetric sensors.

Chapter 7 concerns itself with the modelization of the proposed sensor using the theoretical tools presented before. We first modelize each component of the sensor in terms of Mueller matrices and show the final integrated behaviour of the device in response to pressure. The next section deals with tolerancing. We analyze the theoretical sensitivity of our design to mechanical construction errors as well as to temperature fluctuations and establish a theoretical model of the precision and accuracy of the sensor in the absence of calibration. We also propose solutions to physically compensate for temperature-induced uncertainties when necessary.

Chapter 6

Conceptual design of a piezo-optic pressure sensor

This chapter presents the evolution of the proposed sensor from a simple initial concept to a more polished design. The initial idea is presented in details with its strengths and weaknesses. We present the different constraints - both environmental and commercial - the sensor would be subjected to, as well as its qualities with regards to each of them. From this analysis we find the key points that can be improved and propose a revised concept for the sensor.

6.1 Initial concept

The proposed sensor is based on a simple idea: a dielectric material subjected to a force will become birefringent through the piezo-optic effect, as presented in chapter 5. This birefringence can be analyzed by using polarized light, and the amplitude of the force can thus be deduced. This principle, upon which we will build the rest of the discussion, is illustrated in figures 6.1 (a) and (b).

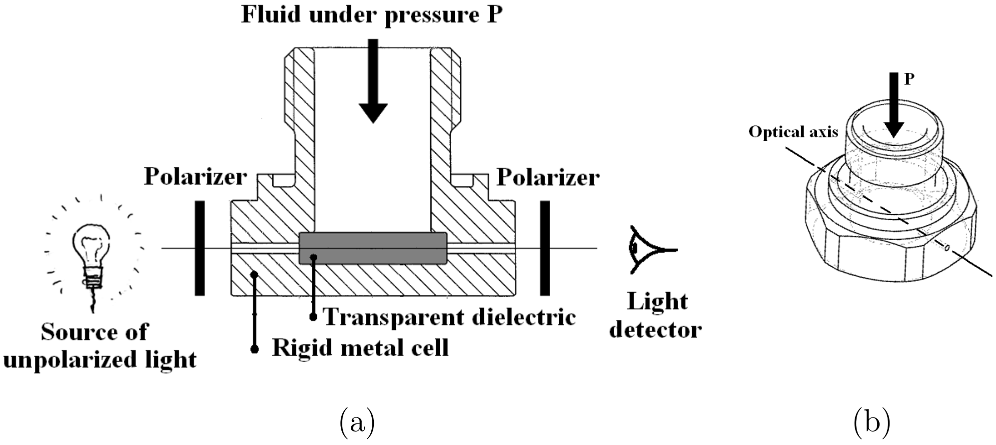

Figure 6.1: Initial concept of a piezo-optic pressure sensor. (a) 2D sketch of the principle, (b) 3D representation of a possible realization.

A source of unpolarized light sends a beam through a first polarizer, then through the dielectric material embedded in a rigid cell and finally through a second polarizer; the output intensity is detected on a photodetector. The presence of the rigid cell is motivated by two reasons: firstly only one face of the dielectric material is under pressure, effectively converting the pressure into a directional force, and secondly the cell allows the portion of the system potentially exposed to the fluid to be quite small and more robust, greatly reducing the risk of leakage.

We now present how this system works in greater details.

6.2 Modelization

6.2.1 Mechanical modelization

We modelize the dielectric transducing portion of the system as a cylinder oriented along $\mathbf{y}$. The rigid cell prevents any deformation along $\mathbf{x}$ and $\mathbf{z}$ as well as any movement of the lower face of the cylinder. Only the top face is free, and that face is subjected to a pressure P. The two windows through which the light will enter and exit the cell are along the $\mathbf{x}$ axis and are considered small compared to the size of the system. The dielectric cylinder has Young modulus E, Poisson ratio ν and diameter d.

Considering only elastic deformations, we can calculate the distribution of stress σ and strain δ in the material using Hooke's Law [51]. Owing to the isotropy of the material and the uniformity of the constraints, any solution in a elementary portion of the volume will be valid for the whole cylinder and no shear stresses or strains can appear. Hooke's laws gives the elementary displacements as:

$$\begin{cases} \delta_x &= \frac{1}{E}\left(\sigma_x - \nu(\sigma_y + \sigma_z)\right) \\ \delta_y &= \frac{1}{E}\left(\sigma_y - \nu(\sigma_x + \sigma_z)\right) \\ \delta_z &= \frac{1}{E}\left(\sigma_z - \nu(\sigma_x + \sigma_y)\right) \end{cases} \tag{6.1}$$

The cylindrical symmetry of the geometry imposes that $\sigma_x = \sigma_z = \sigma$, and the fact that the rigid cell prevents any displacement along $\mathbf{x}$ and $\mathbf{z}$ imposes $\delta_x = \delta_z = 0$. The stress along $\mathbf{y}$ is only due to the pressure on the element, ie $\sigma_y = -P$, and we can now easily solve the problem:

$$\begin{aligned} \delta_x &= \frac{1}{E}\left(\sigma_x - \nu(\sigma_y + \sigma_z)\right) = \frac{1}{E}\left(\sigma - \nu(-P + \sigma)\right) = 0 \\ \text{ie} \quad \sigma &= -\frac{\nu P}{1-\nu} \\ \delta_y &= \frac{1}{E}\left(\sigma_y - \nu(\sigma_x + \sigma_z)\right) = \frac{1}{E}\left(-P - 2\nu\sigma\right) \\ \text{ie} \quad \delta_y &= -\frac{P}{E}\left(1 - \frac{2\nu^2}{1-\nu}\right) \end{aligned}$$

and in the end we have:

$$\begin{cases} \delta_x &= 0 \\ \delta_y &= -\frac{P}{E}\left(1 - \frac{2\nu^2}{1-\nu}\right) \\ \delta_z &= 0 \end{cases} \quad \begin{cases} \sigma_x &= -\frac{\nu P}{1-\nu} \\ \sigma_y &= -P \\ \sigma_z &= -\frac{\nu P}{1-\nu} \end{cases} \tag{6.2}$$

These results are independent from the dimensions of the cylinder and are valid at all points in the volume under pressure.

In a practical device the dielectric cylinder would be bound to the walls of the cell, resulting in a non-uniform stress in the path of the light. The problem can be modelized and solved using a Finite Element Method (FEM) simulation to obtain the kind of "realistic" stress and strain profiles illustrated in figure 6.2:

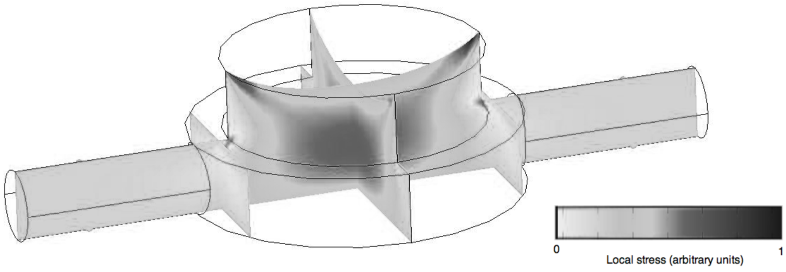

Figure 6.2: FEM (COMSOL) Simulation of a realistic device with the edges of the dielectric cylinder rigidly bound to the rigid cell (not shown). The gradient indicates internal stress, and the apparent deformation is proportional to the computed surface deformation.

The magnitude of the effect of the walls on the stress/strain distribution will depend on various parameters, but with a wide enough cylinder and small overall deformations this error can be small enough to be safely ignored in a first modelization of the problem. The validity of this simplification will be further justified in chapter 7 through a comparison between FEM models.

6.2.2 Optical modelization

Using the Mueller matrices presented in section 4.5 and 5.1, the behaviour of the system is straightforward to modelize. So far we have not specified the orientations of the different optical elements, and so we have in general:

$$\mathbf{M} = \mathbf{M}_{diat}\left(p_{x2}, p_{y2}, \theta_2\right) \cdot \mathbf{M}_{Cell} \cdot \mathbf{M}_{diat}\left(p_{x1}, p_{y1}, \theta_1\right)$$

We choose to use the direction of the force on the dielectric cylinder, ie $\mathbf{y}$, as the reference for angular positions. From the stress-induced birefringence result of section 5.2 and the mechanical stress in 6.2 we find that the phase difference due to the pressure is:

$$\begin{aligned}\triangle\varphi &= \frac{2\pi}{\lambda}\cdot d\cdot\triangle n = \frac{2\pi}{\lambda}\cdot d\cdot C\cdot(\sigma_x-\sigma_y)\\ &= \frac{2\pi}{\lambda}\cdot d\cdot C\cdot P\cdot\frac{1-2\nu}{1-\nu}\end{aligned} \tag{6.3}$$

and we can explicit $\mathbf{M}_{Cell}$:

$$\mathbf{M}_{Cell} = \begin{bmatrix} 1 & 0 & 0 & 0\\ 0 & 1 & 0 & 0\\ 0 & 0 & \cos\left(\frac{2\pi}{\lambda}\cdot d\cdot C\cdot P\cdot\frac{1-2\nu}{1-\nu}\right) & -\sin\left(\frac{2\pi}{\lambda}\cdot d\cdot C\cdot P\cdot\frac{1-2\nu}{1-\nu}\right)\\ 0 & 0 & \sin\left(\frac{2\pi}{\lambda}\cdot d\cdot C\cdot P\cdot\frac{1-2\nu}{1-\nu}\right) & \cos\left(\frac{2\pi}{\lambda}\cdot d\cdot C\cdot P\cdot\frac{1-2\nu}{1-\nu}\right)\end{bmatrix} \tag{6.4}$$

Carrying out the multiplications and applying the resulting matrix to the Stokes vector for an unpolarized light, we find that the output intensity is:

$$\begin{aligned}I = &\frac{I_0}{4}\cdot\left(p_{x2}^2+p_{y2}^2\right)\left(p_{x1}^2+p_{y1}^2\right)\\ &+\frac{I_0}{4}\cdot\left(p_{x2}^2-p_{y2}^2\right)\left(p_{x1}^2-p_{y1}^2\right)\cos\left(2\theta_1\right)\,\cos\left(2\theta_2\right)\\ &-\frac{I_0}{4}\cdot\left(p_{x2}^2-p_{y2}^2\right)\left(p_{x1}^2-p_{y1}^2\right)\sin\left(2\theta_1\right)\sin\left(2\theta_2\right)\cos\left(\frac{2\pi}{\lambda}\cdot d\cdot C\cdot P\cdot\frac{1-2\nu}{1-\nu}\right)\end{aligned} \tag{6.5}$$

We see from this expression that the overall sensitivity of the sensor will depend on the quality of the polarizers and on the relative angular orientations of the elements. The sensitivity to the pressure is readily seen to depend on the term $\sin(2\theta_1)\sin(2\theta_2)$, and will be maximum if θ_1 and θ_2 are multiples of $\pi/4$. We can reach a similar conclusion without the explicit formula through a more physical and visual approach to the problem:

Consider a totally polarized light as the sum of two independent transverse waves respectively oscillating along $\mathbf{x}$ and $\mathbf{y}$, of amplitudes E_x, E_y. These waves cross a birefringent element with its axes also aligned with $\mathbf{x}$ and $\mathbf{y}$. In this configuration the birefringent material simply adds a different phase to each component of the light. Consider the case where $E_x = 0$: the output beam is only polarized along $\mathbf{y}$ and though its phase will vary its intensity will not; but if E_x increases both waves have to be summed to find the output state of polarization, and the phase component starts having an effect. The same result is of course true for $E_y = 0$, and intuitively the maximum effect is attained when $E_x = E_y$. In the case of a linearly polarized input light, this corresponds to a ±45° inclination of the input polarizer with regards to the stress axes.

To find the optimal orientation for the output polarizer we can reason in a similar way: if it is oriented along either $\mathbf{x}$ or $\mathbf{y}$ it will only "select" E_x or E_y, totally ignoring any phase difference effect. The optimal angle is then once again ±45°, which means the two polarizers have to be either crossed or parallel to each other.

Finally we can use a graphical simulation, presented on figure 6.3 of the sensitivity with regards to the angles to confirm our result:

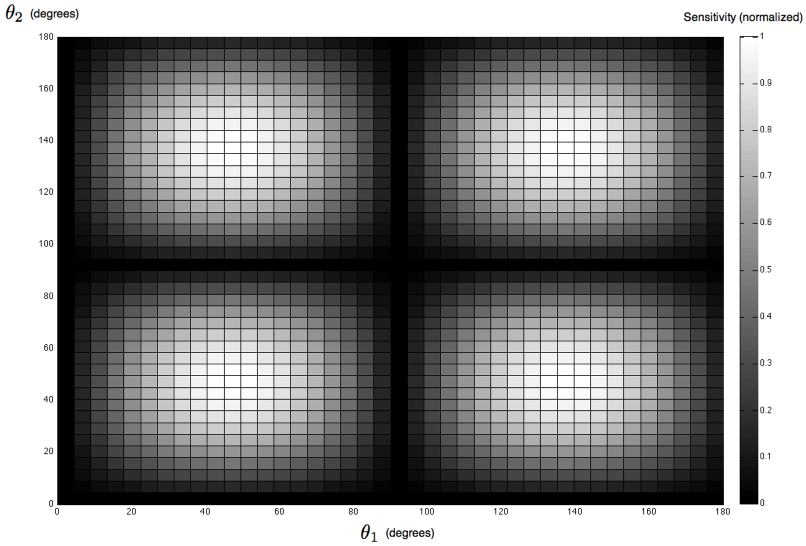

Figure 6.3: Sensitivity depending on the angles of the input and output polarizers. The sensitivity is calculated here as the difference between the minimum and maximum output intensity for each combination of polarizer angles.

We see clearly that the maximums of sensitivity are attained for any combination of $\theta_1 = \pm 45°$ and $\theta_2 = \pm 45°$ as expected. Another interesting aspect is that the peaks are rather flat which indicates a low sensitivity to positioning errors; this particular aspect of the system, along with its sensitivity to various other parameters, will be further studied in the next section.

6.3 Performances and limitations of the proposed concept

Now that the mechanical and optical behaviors of our sensing system are clearer, we analyze it in terms of performances: realistic ranges of pressure that can be measured, measurement precision, and sensitivity to fabrication errors.

We then analyze it further in terms of commercial feasibility, mainly by checking the cost/quality ratio of our sensor compared to commercially available products.

6.3.1 Theoretical performances

6.3.1.1 Sensor size and pressure measurement range

Simplifying equation 6.5 by considering perfect polarizers at the ideal inclination, we find that the output intensity of our sensor would follow:

$$I = \frac{I_0}{4} \cdot \left(1 - \cos\left(\frac{2\pi}{\lambda} \cdot d \cdot C \cdot P \cdot \frac{1-2\nu}{1-\nu}\right)\right) \tag{6.6}$$

The periodicity of this function restricts the unambiguous measurement of its phase to one period and we have a first restriction on the pressure we can measure:

$$P \leqq \frac{\lambda}{d} \cdot \frac{1-\nu}{1-2\nu} \cdot \frac{1}{C} \tag{6.7}$$

We grouped the parameters depending on the level of control that we can have over them: the wavelength and the length of the cylinder can be somewhat freely selected, the second term depends on the geometry of the cell (most importantly on whether the cylinder is allowed to deform in a given direction) and on the Poisson ratio, and the last variable is set by the choice of the dielectric material.

We now impose further restrictions to our sensor, keeping in mind that they are just rough constraints to make the problem more realistic:

- The cost being of importance, the light source should be the cheapest possible. The oldest, easiest to produce and thus cheapest LEDs emit in the red and infrared regions [52]; we select 650nm as a reference wavelength,

- A second consequence of the cost limitation is that the dielectric has to be readily available. Such common transparent materials include glass as well as polymethylmethacrylate (PMMA) and a variety of other polymers [53, 54]; these two examples have physical properties typical of the materials we could use, and we will use them as reference,

- The size of the sensor is somewhat limited by its commercially available equivalents to a few centimeters in length at most, so we impose that the dielectric path be no longer than two centimeters.

With these additional constraints we can estimate that the sensor will measure pressures on a full scale of as little as $400\,mbar$ with a soft polymer[1]. The range can be increased to much higher pressures by a suitable choice of material, and for instance a full scale of $100\,bar$ using typical PMMA[2] cylinder is attainable for $d \leqq 2.1\,cm$.

6.3.1.2 Sensitivity to pressure

As discussed in section 6.2.2, the overall amplitude of the response of our transducer can be maximized by selecting the optimal angles for the polarizers. The resulting output intensity, assuming that we are using perfect polarizers, then follows equation 6.6, where is it seen that the response follows a sine function with respect to increasing pressure.

Taking the Taylor expansion of equation 6.6 near three different points of the sine curve, $\triangle\varphi = \frac{2\pi}{\lambda} \cdot d \cdot C \cdot \frac{1-2\nu}{1-\nu} \cdot P = K \cdot P = 0,\ \frac{\pi}{2},\ \pi$, provides information on the sensitivity of the sensor. For low pressures, ie around the zero of the sine curve, the intensity varies with the square of the pressure: the sensor has very poor sensitivity and a highly non-linear response; around the middle of the curve the intensity is proportional to pressure with maximum sensitivity and linearity; finally at the “top” of the sine the intensity varies once again with the square of the pressure. These

---

[1] $d = 2\,cm,\ \nu = 0.4,\ C = 1.2 \cdot 10^{-9}\,Pa^{-1}$ [54]

[2] Plexiglas 55, $\nu = 0.345,\ C = 3.3 \cdot 10^{-12}\,Pa^{-1}$ [55, 56]

conclusions immediately apparent when looking at figure 6.4 which shows a typical pressure/intensity response curve:

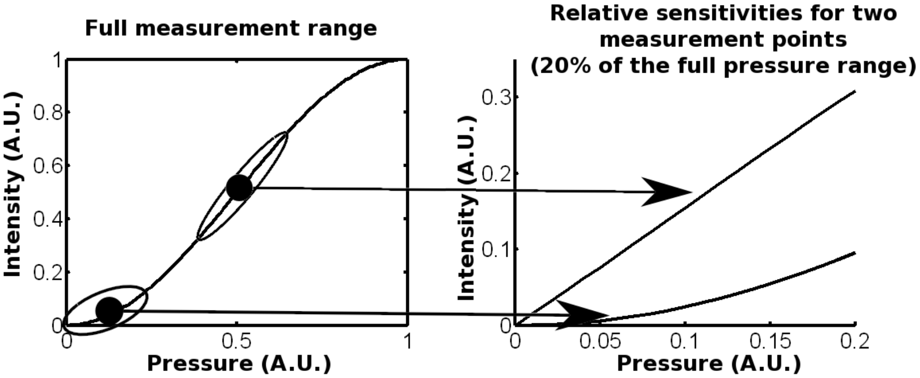

Figure 6.4: A typical pressure/intensity response curve, which illustrates the differences in sensitivity depending on the measurement point.

Clearly the most favorable point of measurement is around the $\varphi = \pi/2$ portion of the response curve as it is the point where the sensitivity is maximal and the response is the most linear. Using this result in the Mueller matrix of our birefringent cell (equation 6.4), we obtain the Mueller matrix of a quarter-wave plate with its axes aligned with our reference axes. The combination of a quarterwave-plate right after a linear polarizer inclined at 45° always results in a circular polarization, and so the best performances of the proposed sensor are attained when the detected polarization is circular.

6.3.1.3 Sensitivity to temperature

One critical point, if the transducer is to be integrated in an industrial product, is its behaviour under temperature changes. Temperature could easily affect the precision or the accuracy of a sensor, so its sensitivity to temperature has to be carefully checked and made as small as possible.

In our case temperature can have an effect on three different parameters of the transducer:

- it can modify the refractive index of the dielectric material [57],
- it can result in a deformation of the geometry through temperature-induced dilatation and contraction [58, 59]; a dilatation or a

contraction can, in turn, result in a new distribution of stress in the material,

- the Young modulus and Poisson ratio of the material depend on temperature and will also be modified [58, 59].

All of these effects will have to be taken into account and potentially compensated for if they turn out to be too important to maintain the precision within the desired range.

6.3.1.4 Systematic errors

The sensitivity to temperature was singled out in the previous section because of its importance, but it is only one of the various possible sources of measurement uncertainty in the proposed sensor. The temperature-independent optical sources of uncertainty can be identified in equation 6.5: in the subsequent analysis we assumed perfect polarizers and a perfect alignment of the optical components, which is of course never the case in practice [60].

The first limiting factor is the quality of the polarizers: as can be seen in equation 6.5 a non-zero extinction along the extinction axis will result in a systematic error:

$$\triangle I_{ext} = \frac{I_0}{4} \cdot \left(1 - \left(p_{x2}^2 + p_{y2}^2\right)\left(p_{x1}^2 + p_{y1}^2\right)\right)$$

that is in effect a constant bias added to the measured pressure. The same defects in the polarizers will also impact the sensitivity of the system as can be seen in equation 6.5.

The second source of error is the alignment of the polarizers with respect to each other and to the direction of applied force. In the same manner as before we can see that an error on the alignment, in the presence of non-ideal polarizers, results in a systematic error:

$$\triangle I_{align} = \frac{I_0}{4} \cdot \left(p_{x2}^2 - p_{y2}^2\right)\left(p_{x1}^2 - p_{y1}^2\right) \cos\left(2\theta_1\right)\, \cos\left(2\theta_2\right)$$

As with the extinction ratio, this issue results in a lower sensitivity.

Preventing these systematic errors requires high quality polarizers and a precise alignment method, but they could also be compensated for through a calibration phase for each sensor previously to its use.

6.3.2 Commercial and technological constraints

So far we have only analyzed the theoretical behaviour, and potential problems, of the proposed system. Another aspect of the problem to take into consideration, if the ultimate goal is a commercial application, is the overall cost of producing the sensor. Putting aside everything not related to the optical portion of the device, we can split the cost into the cost of the individual elements and the cost of assembling these elements, ie the complexity of the system.

So far the proposed design requires at least three purely optical components (ignoring the light source, detector, and the accompanying electronics): two polarizers and the dielectric cell. While the dielectric cell can be made of any convenient material and is a very flexible component, the polarizers pose more of a problem. Plastic "Polaroid" polarizers are cheap, but their poor extinction ratio [61] will create a systematic error as seen in the section 6.3.1.4. High quality polarizers would reduce that error, but they are much more expensive and difficult to handle.

The second source of production costs is the inherent complexity of the system and the number of steps it would take to build it. Here the costly steps would mainly be the alignment of the polarizers. As we have seen in section 6.3.1.4, an alignment error is yet another source of systematic error, and a precise alignment can only be achieved through optical control, hardly a simple step to add to a production chain.

Although the problems listed here are not intractable in the proposed setup, they are best addressed through a redesign of the transducer.

6.4 Revised concept

The previous section presented a basic concept for a piezo-optic pressure transducer. Although the proposed setup is a straightforward application of the theoretical principles that make this transducing method work, it presents several shortcomings and weaknesses that we now try to negate. The main issues were the price and quality of polarizers, the low sensitivity around the "null pressure" point, and the overall complexity of the system. We now address these points one by one and unify the resulting solutions into a revised design proposal.

6.4.1 Maximization of the sensitivity

We deduced in section 6.2.2 a condition on the orientation of the input and output polarizers to maximize the sensitivity of the sensor. We now produce a more general demonstration where the input state of polarization is not linear anymore but can be any fully-polarized state.

We consider, as before, a dielectric cell with one of its faces submitted to the pressure to be measured. The force applied to the dielectric material is in strictly vertical (see 6.2.1), so the total effect is that of a vertical variable-phase waveplate as we presented in equation 6.4. After passing through the cell, the light goes through a linear polarizer that can be set at any desired angle before hitting the detector. Assuming that we use perfect components the output of the full system can be described by:

$$S_{out} = M_{Rotator}(-\theta_{pol}) \cdot M_{Polarizer} \cdot M_{Rotator}(\theta_{pol}) \cdot M_{waveplate}(\triangle\varphi) \cdot S_{in}$$

where the first component of S_{out} will be the intensity seen by the detector.

Carrying out the multiplications and looking only at $S0_{out}$ which contains the intensity seen by the detector, we find that:

$$I_{out} = S0_{out} = \frac{1}{2} \cdot (S0_{in} + S1_{in}\cos(2\theta_{pol}) + (S2_{in}\cos(\Delta\varphi) - S3_{in}\sin(\Delta\varphi)) \cdot \sin(2\theta_{pol})) \tag{6.8}$$

The first noticeable aspect of this equation is that the amplitude of the force-dependent portion of the output intensity is directly modulated by the orientation of the output polarizer through the term $\sin(2\theta_{pol})$. The amplitude is maximal for $\sin(2\theta_{pol}) = \pm 1$, ie for $\theta_{pol} = \frac{\pi}{4} + n \cdot \frac{\pi}{2}$, which means that the axes of the polarizer have to be oriented at ±45° of the vertical axis for best performances. This is the same result we found before, and we select this angle for the rest of the analysis.

Another point of interest is revealed through the application of the trigonometric identity

$$S2_{in}\cos(\Delta\varphi) - S3_{in}\sin(\Delta\varphi) = \sqrt{S2_{in}^2 + S3_{in}^2} \cdot \sin(\Delta\varphi + \Phi)$$

where $\tan(\Phi) = \frac{S2_{in}}{-S3_{in}}$. Since we only considered totally polarized light we know that $S1_{in}^2 + S2_{in}^2 + S3_{in}^2 = S0_{in}^2$ ie that $\sqrt{S2_{in}^2 + S3_{in}^2} = S0_{in} \cdot \sqrt{1 - S1_{in}^2}$ which has to be maximized in order to once again optimize the sensitivity. The maximum is obviously attained for $S1_{in}^2 = 0$ which gives a new strong constraint on the input state of polarization for best performances of the setup.

With these two conditions,

$$\begin{cases} \theta_{pol} = \pm 45° \\ S1_{in} = 0 \end{cases}$$

we have maximized the sensitivity of the setup and the output intensity is, similarly to equation 6.6:

$$\frac{I_{out}}{I_{in}} = \frac{1}{2} \cdot (1 + \sin(\Delta\varphi + \Phi))$$

Because Φ depends on $\frac{S2_{in}}{-S3_{in}}$, changing the input state of polarization changes the zero point of the sensor on the response curve, and thus the sensitivity to pressure around that point. Exactly as discussed in section 6.3.1.2 we can see that the response is most sensitive and linear for a circular input polarization, but one additional important information from this derivation is that the polarization only has to be circular *when it reaches the output polarizer*; as long as $S1_{in} = 0$ before entering the piezo-optic cell, the sensitivity will be maximum. This deduction decorrelates the optimization of the sensitivity of the piezo-optic process and the optimization of the sensitivity of the detection process and grants us more freedom in the conception of the overall system.

We can now optimize the sensitivity of the detection process, or rather recall that we already did before in section 6.3.1.2: we have shown that the detection sensitivity in highest in the quasi-linear part of the typical sinusoidal response curve, which corresponds to a circular polarization right before the final linear polarizer.

From the two conclusions above we now know how to, at least in principle, maximize the sensitivity of the transducer.

6.4.2 Reduction of the complexity of the design

6.4.2.1 Generation of the optimal state of polarization

We have shown that maximal piezo-optic sensitivity is attained when the state of polarization entering the piezo-birefringent portion of the sensor verifies the condition $S1_{in} = 0$. As for the maximal sensitivity of the detection, it is attained for a circular polarization at the output linear polarizer.

The first condition is easily achieved by rotating the input polarizer to 45° of the principal axes of the pressure-sensitive section.

The second requirement can be met by placing a quarter-wave plate in the path of the light, either before or after piezo-birefringent area. Both of these solutions have the inconvenience of adding another component to the sensor, a component that has to be precisely aligned; moreover, good quarter-wave plates are expensive, and cheap plastic ones are notoriously sensitive to temperature. Alternatively, we can use the polarizing properties of reflections to achieve the desired optical functions.

We have seen in chapter 5 that partial and total reflections at a dielectric boundary have respectively the properties of a diattenuator and of a waveplate. Our goal being to emulate a quarter-wave plate, we can make use of the phase shift induced by a total internal reflection to transform a linear polarization into a circular one. This is essentially the problem solved by Fresnel in the creation of the Fresnel rhomb [45, p. 53], and we are confronted with the same issue: the refractive index of usual materials is too small to generate a full $\pi/2$ phase shift in a single reflection (on figure 5.4 for instance, at a typical glass/air interface, the maximum phase shift is a little over 45°); this is easily solved by ensuring that the beam of light reflects twice to achieve the desired total phase shift. For instance, numerically solving for the incidence angle in equation 5.18 with $\delta_r = \pi/4$, $n_1 = 1.5$, $n_2 = 1$ we obtain two values for the "semi-circularizing" angle:

$$\theta_{sc} = \begin{cases} 50.2^\circ \\ 53.3^\circ \end{cases}$$

We can find the minimum value for n_2/n_1 that allows a $\pi/4$ phase shift by differentiating δ_r with regards to θ_i in equation 5.18 and equating the result to zero in order to find the angle for which the phase difference is maximum. This yields:

$$\theta_m = \frac{\pi}{2} - \arcsin\left(\sqrt{\frac{(n_1/n_2)^2 - 1}{(n_1/n_2)^2 + 1}}\right) \tag{6.9}$$

and inserting it back into 5.18:

$$\tan(\frac{1}{2}\delta_r) = \frac{(n_1/n_2)^2 - 1}{2(n_1/n_2)} \tag{6.10}$$

Finally, solving 6.10 for $\delta_r = \pi/4$ yields the condition on the ratio of the refraction indices:

$$\frac{n_1}{n_2} \geq 1.4966 \tag{6.11}$$

At this particular ratio, the semi-circularizing angle is, as per equation 6.9, equal to 51.79°.

6.4.2.2 Replacement of the polarizers

One method to easily attain high degrees of linear polarization is to make use of the Brewster Angle at a reflection. We discussed this effect in section 5.3. To summarize the principle, there exists an angle θ_B for which the reflected light will be totally linearly polarized perpendicularly to the plane of incidence.

Since this effect is dependent on the angle of incidence, and hence the divergence of the light source, planar polarizers are often preferred as they are not as challenging to align and use. Brewster polarizers are also more bulky than their conventional counterparts. They are mostly used when extremely high extinction ratios that can not be attained by regular polarizers are required, and this results in most available Brewster polarizers being very precise and expensive optical components. In the case of our pressure transducer, we are in the special situation where even low-quality Brewster polarizers would give us a much better extinction ratio than low-cost Polaroid ones for a comparable final cost, as they can be molded in plastic or any other easily usable material. Moreover we already plan on using reflection effects to generate circular polarization, and consequently adding one more interface at a precise angle will not be a problem.

6.4.3 Proposed design for a piezo-optic pressure sensor

Building on all the ideas put forward in this chapter, we can now propose a monolithic design for a piezo-optic pressure sensor, presented on figure 6.5.

The first component of the system is a LED so as to provide cheap, reliable, and relatively monochromatic unpolarized light (1). This unpolarized beam enters a single specially shaped block of dielectric material, and the first interface it crosses is at the Brewster angle (2); the beam is now linearly polarized in the incidence plane of the Brewster interface (3).

The next surface (4) has its plane of incidence oriented at 45° to that of the Brewster interface, and the incidence angle of the beam is θ_{sc} so that a relative phase shift of $\pi/4$ is added, resulting in an elliptic polarization (5). The light now enters the pressure-sensitive section of the sensor, which consists in a rigid cell (not shown) encasing the dielectric material (6), ensuring that hydraulic pressure will only act on one of its faces; the cell has two optical windows to let the light beam in and out (not shown). The rest of the system is symmetrical to the first part: the light next reaches a second interface at the angle θ_{sc}, before being filtered by a second Brewster interface. Finally the output intensity is detected on a photodetector (7).

In the schematic representation presented here the pressure applied on (6) would be transmitted to the whole material and modify its properties outside of the area of interest, but in practice the section under pressure would be isolated inside a steel vessel (with windows to let the light through) around which the rest of the device would be molded.

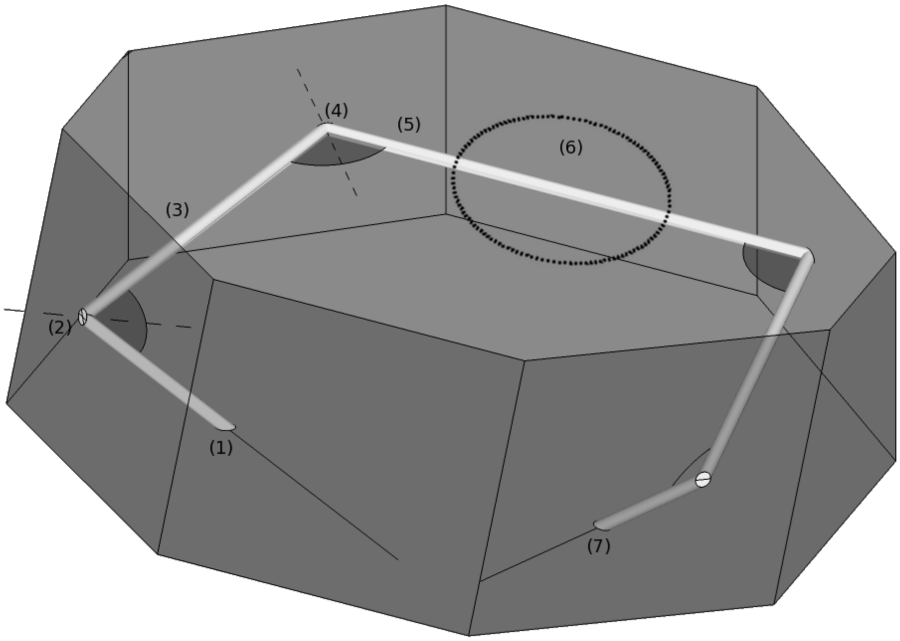

Figure 6.5: 3D representation of the proposed optical component for a piezo-optic pressure sensor

This orignal design presents several advantages, the main one being that it can essentially molded in a single block of transparent material. Once a mold has been realized, each sensor can be produced in only a few steps and does not require any sort of setup to align optical elements. Once the monolithic portion has been molded the optical portion of the device is ready. Another advantage, as discussed before, is that the sensor works in its range of maximum sensitivity; the response is also quasi-linear and does not require complex electronic corrections to output a pressure value.

Chapter 7

Modelization of the proposed piezo-optic pressure sensor

We now consider the concept proposed in the previous chapter and modelize its behaviour using the theoretical tools presented in chapters 4 and 5. Once the system has been modelized in terms of Mueller matrices, we explicit its response in an ideal scenario. We then analyze and quantify the different sources of error and uncertainty that can appear in a real device.

7.1 Optical modelization

7.1.1 Description

We briefly recall the principle of the device being modelized, as illustrated on figure 7.1.

An unpolarized beam of light enters a transparent material. It is reflected on a first interface at the Brewster angle θ_B, then on a second interface at the angle θ_{hc}; the plane of incidence on the first interface (1) is tilted 45° from the plane of incidence (2) on the second interface. The beam of light next passes through a section of the device that can be subjected to an external pressure. In a symmetrical manner, it is then once again reflected at the angle θ_{hc} and on a final interface at the Brewster angle; the two planes of incidence are tilted at 45° of each other.

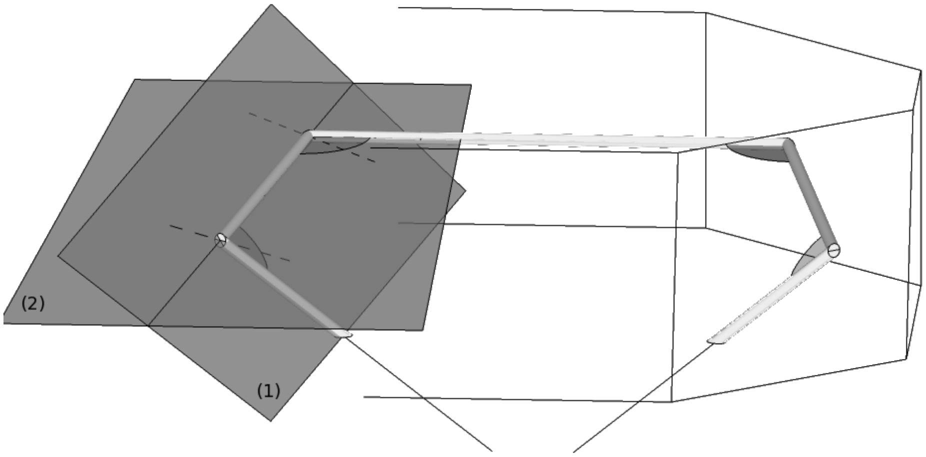

Figure 7.1: Schematic of the path followed by a ray of light inside the proposed device

7.1.2 Mueller-Stokes modelization

We now describe the system in terms of Mueller matrices and calculate the Stokes vectors that describe the polarization at different points along the optical path. Mueller matrices and Stokes coefficients are defined in a given basis, and in the case of reflections at an interface we use the one defined by the plane of incidence and the propagation direction. As seen in figure 7.1 the light propagates in three non-collinear planes as it crosses the device. The Mueller matrices will always be defined in the plane of incidence of the reflection they describe, and we will specify the plane which serves as reference for the Stokes coefficients with the exponent $S^{(i)}$.

The source emits unpolarized light. Ignoring eventual losses at the entrance of the device, the normalized initial Stokes vector is $\mathbf{S}_{\mathbf{in}}^{(\mathbf{1})} = [1; 0; 0; 0]$.

The first reflection is a partial reflection at the angle θ_{B1}, equal or close to the Brewster angle, and is described by Mueller matrix 7.1 (using equations

5.10, 5.9 and 5.19):

$$\begin{cases} \mathbf{M}_{pr}\left(n_1, n_2, \theta_{B1}\right) = \frac{1}{2} \cdot \begin{bmatrix} r_\perp^2 + r_\shortparallel^2 & r_\perp^2 - r_\shortparallel^2 & 0 & 0 \\ r_\perp^2 - r_\shortparallel^2 & r_\perp^2 + r_\shortparallel^2 & 0 & 0 \\ 0 & 0 & 2r_\perp r_\shortparallel & 0 \\ 0 & 0 & 0 & 2r_\perp r_\shortparallel \end{bmatrix} \\ r_\perp = -\frac{\sin(\theta_{B1}-\theta_{t1})}{\sin(\theta_{B1}+\theta_{t1})} = \frac{n_1\cos(\theta_{B1})-n_2\cos(\theta_{t1})}{n_1\cos(\theta_{B1})+n_2\cos(\theta_{t1})} \\ r_\shortparallel = \frac{\tan(\theta_{B1}-\theta_{t1})}{\tan(\theta_{B1}+\theta_{t1})} = \frac{n_2\cos(\theta_{B1})-n_1\cos(\theta_{t1})}{n_2\cos(\theta_{B1})+n_1\cos(\theta_{t1})} \end{cases} \tag{7.1}$$

after which the Stokes vector becomes $\mathbf{S_1^{(1)}} = \mathbf{M}_{pr}\left(n_1, n_2, \theta_{B1}\right) \cdot \mathbf{S_{in}}$. The plane of incidence of the second reflection being tilted at $\theta_1 = 45°$ with respects to the plane of incidence of the first reflection, so we have to perform a rotation of the basis in which we describe the Stokes coefficients before carrying out the next calculation. Taking the second plane as the new reference, this is in effect equivalent to the polarization being subjected to a rotation of angle θ_1 described by Mueller matrix 7.2 (from equation 4.37):

$$\mathbf{M}_{rot}\left(\theta_1\right) = \begin{bmatrix} 1 & 0 & 0 & 0 \\ 0 & \cos\left(2\theta_1\right) & -\sin\left(2\theta_1\right) & 0 \\ 0 & \sin\left(2\theta_1\right) & \cos\left(2\theta_1\right) & 0 \\ 0 & 0 & 0 & 1 \end{bmatrix} \tag{7.2}$$

and the Stokes parameters in the correct basis are described by $\mathbf{S_1^{(2)}} = \mathbf{M}_{rot}\left(\theta_1\right) \cdot \mathbf{M}_{pr}\left(n_1, n_2, \theta_{B1}\right) \cdot \mathbf{S_{in}^{(1)}}$.

The second reflection is a total reflection at the angle θ_{sc1}, and it is described by Mueller matrix :

$$\begin{cases} \mathbf{M}_{tr}\left(n_1, n_2, \theta_{sc1}\right) = \begin{bmatrix} 1 & 0 & 0 & 0 \\ 0 & 1 & 0 & 0 \\ 0 & 0 & \cos\left(\delta_{r1}\right) & -\sin\left(\delta_{r1}\right) \\ 0 & 0 & \sin\left(\delta_{r1}\right) & \cos\left(\delta_{r1}\right) \end{bmatrix} \\ \tan(\frac{1}{2}\delta_{r1}) = -\frac{\cos(\theta_{sc1})\sqrt{\sin^2(\theta_{sc1})-\left(\frac{n_2}{n_1}\right)^2}}{\sin^2(\theta_{sc1})} \end{cases} \tag{7.3}$$

The Stokes vector at this point is then $\mathbf{S_2^{(2)}} = \mathbf{M}_{tr}\left(n_1, n_2, \theta_{sc1}\right) \cdot \mathbf{S_1^{(2)}}$.

Next, the beam of light propagates through the piezo-birefringent section of the system. We recall from equation 6.4 that it is described by the Mueller matrix:

$$\begin{cases} \mathbf{M}_{Cell}(\triangle\varphi) = \begin{bmatrix} 1 & 0 & 0 & 0 \\ 0 & 1 & 0 & 0 \\ 0 & 0 & \cos(\triangle\varphi) & -\sin(\triangle\varphi) \\ 0 & 0 & \sin(\triangle\varphi) & \cos(\triangle\varphi) \end{bmatrix} \\ \triangle\varphi = \frac{2\pi}{\lambda} \cdot d \cdot C \cdot P \cdot \frac{1-2\nu}{1-\nu} \end{cases} \tag{7.4}$$

and the state of polarization at this point is described by the Stokes vector $\mathbf{S_3^{(2)}} = \mathbf{M}_{Cell}(\triangle\varphi) \cdot \mathbf{S_2^{(2)}}$.

The system is then symmetrical: a total reflection at angle θ_{sc2} yields $\mathbf{S_4^{(2)}} = \mathbf{M}_{tr}(n_1, n_2, \theta_{sc2}) \cdot \mathbf{S_3^{(2)}}$, and a last partial reflection at angle θ_{B2} after a rotation of angle θ_2 finally results in the output Stokes vector $\mathbf{S_{out}^{(1)}} = \mathbf{M}_{pr}(n_1, n_2, \theta_{B2}) \cdot \mathbf{M}_{rot}(\theta_2) \cdot \mathbf{S_4^{(2)}}$.

We can now describe the total polarimetric behaviour of the system by a single Mueller matrix:

$$\begin{aligned} \mathbf{M} &= \mathbf{M}_{pr}(n_1, n_2, \theta_{B2}) \cdot \mathbf{M}_{rot}(\theta_2) \cdot \mathbf{M}_{tr}(n_1, n_2, \theta_{sc2}) \\ &\quad \times \mathbf{M}_{Cell}(\triangle\varphi) \\ &\quad \times \mathbf{M}_{tr}(n_1, n_2, \theta_{sc1}) \cdot \mathbf{M}_{rot}(\theta_1) \cdot \mathbf{M}_{pr}(n_1, n_2, \theta_{B1}) \end{aligned} \tag{7.5}$$

7.1.3 Ideal optical behaviour

Let us consider the case where all the angles in the previous modelization are perfectly equal to their desired value: $\theta_{B1} = \theta_{B2} = \theta_B$, $\theta_1 = \theta_2 = 45°$ and $\theta_{sc1} = \theta_{sc1} = \theta_{sc}$. The two partial reflections simplify to:

$$\mathbf{M}_{pr}(n_1, n_2, \theta_B) = \frac{1}{2} \cdot \left(\frac{n_1^2 - n_2^2}{n_1^2 + n_2^2} \right)^2 \cdot \begin{bmatrix} 1 & 1 & 0 & 0 \\ 1 & 1 & 0 & 0 \\ 0 & 0 & 0 & 0 \\ 0 & 0 & 0 & 0 \end{bmatrix}$$

the two total reflections to:

$$\mathbf{M}_{tr}\left(n_1, n_2, \theta_{hc}\right) = \frac{\sqrt{2}}{2}\begin{bmatrix} \sqrt{2} & 0 & 0 & 0 \\ 0 & \sqrt{2} & 0 & 0 \\ 0 & 0 & 1 & -1 \\ 0 & 0 & 1 & 1 \end{bmatrix}$$

and the two rotations to:

$$\mathbf{M}_{rot}\left(\pi/4\right) = \begin{bmatrix} 1 & 0 & 0 & 0 \\ 0 & 0 & -1 & 0 \\ 0 & 1 & 0 & 0 \\ 0 & 0 & 0 & 1 \end{bmatrix}$$

Carrying out the operations in equation 7.5 we obtain the Mueller matrix for an "ideal" device:

$$\mathbf{M} = \frac{1}{4} \cdot \left(\frac{n_1^2 - n_2^2}{n_1^2 + n_2^2}\right)^4 \cdot (1 + \sin(\triangle\varphi)) \cdot \begin{bmatrix} 1 & 1 & 0 & 0 \\ 1 & 1 & 0 & 0 \\ 0 & 0 & 0 & 0 \\ 0 & 0 & 0 & 0 \end{bmatrix} \tag{7.6}$$

Equation 7.6 is clearly the Mueller matrix of a linear polarizer with an optical density that depends on the pressure. Assuming the light at the input is totally unpolarized, i.e. $\mathbf{S_{in}} = I_0 \cdot [1; 0; 0; 0]$, the output intensity is then:

$$I = \frac{I_0}{4} \cdot \left(\frac{n_1^2 - n_2^2}{n_1^2 + n_2^2}\right)^4 \cdot (1 + \sin(\triangle\varphi)) \tag{7.7}$$

which is exactly equivalent to equation 6.6 with a $\pi/2$ offset on the phase and an attenuation factor that depends on the optical properties of the material. To get a sense of the order of magnitude of this attenuation factor we can select $n_1 = 1.5$ and $n_2 = 1$ as typical refraction indices, and for $\triangle\varphi = 0$ we obtain $I/I_0 \simeq 5.5 \times 10^{-3}$.

7.2 Measurement uncertainties

7.2.1 Geometry errors

7.2.1.1 Errors on the “semi-circularizing” angles

One source of uncertainty is the angle of the two “semi-circularizing” reflections.

We have seen previously that there are in general two reflection angles that will give us the desired $\pi/4$ phase shift, but it is apparent on figure 7.2 that the phase shift has a steeper dependence on the angle around the least inclined reflection. To minimize the influence of angle error, we always select the second value.

We have also computed in equation 6.11 the ratio of refraction indices, and the corresponding angle, for which the phase shift is exactly $\pi/4$. Since at this point the curve is at a maximum, and since the curve for different indices ratios is sensibly the same as illustrated on figure 7.2, this is the combination of values for which the system will be the least sensitive to an error on the angle of reflection if the right combination of materials can be found.

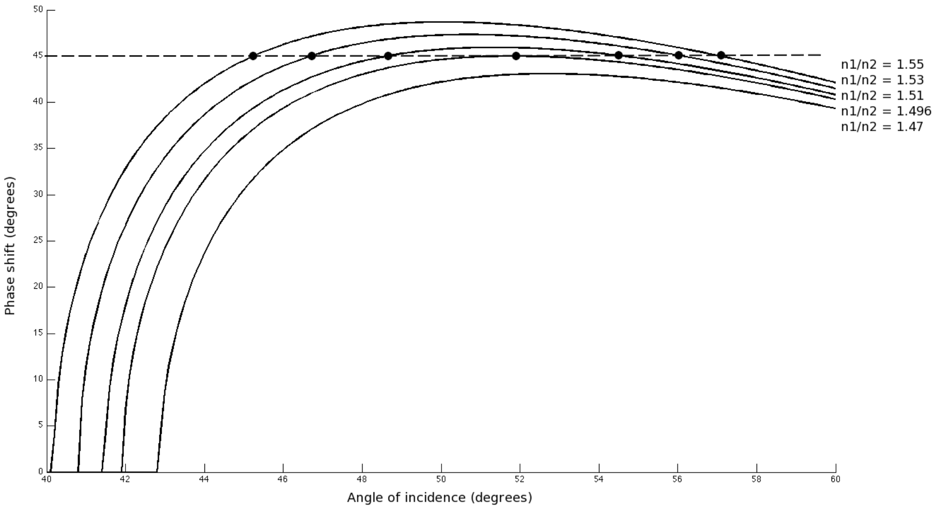

Figure 7.2: Phase shifts induced by a total reflection for different ratios of the indices of refraction

Figure 7.3 displays the phase shift for $n_1/n_2 = 1.4966$ around $\theta_i = 51.79°$, and a quadratic fit shows that the phase shift error varies with the angle error as:

$$\Delta\delta_r \approx -0.106\,(\Delta\theta_i)^2$$

Since the effect of pressure is also to add a phase shift, we can directly obtain the constant error on pressure generated by an error on the angle of reflection:

$$\Delta P \approx -0.106 \frac{\lambda(1-\nu)}{2\pi d C(1-2\nu)}\,(\Delta\theta_i)^2 \tag{7.8}$$

which gives a full-scale precision, according to equation 6.7, of $\Delta P/P_{max} \approx -0.0169 \cdot (\Delta\theta_i)^2$. For instance, with a tolerance on the angle allowing for 1° of error, the error on the measured pressure is lower than 0.06% of the full scale. This error, shown on figure 7.3, is systematic and can be calibrated for, though its order of magnitude is small enough to be ignored depending on the target precision for the sensor.

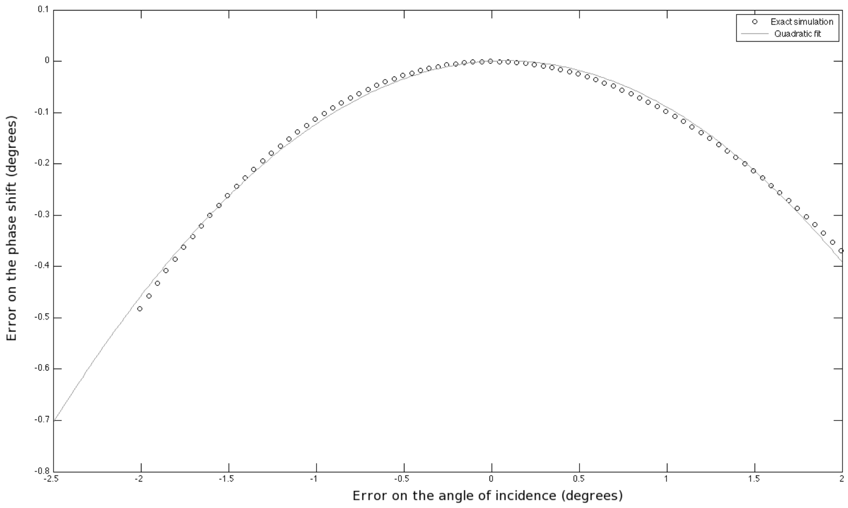

Figure 7.3: Error on the phase shift resulting from an error on the reflection angle ($n_1/n_2 = 1.4966$, incidence angle centered on $\theta_i = 51.79°$ and phase shift on 45°)

7.2.1.2 Errors on the Brewster angles

A second source of uncertainty in the response of the system is the effect of angle errors on the two Brewster reflections.

If the reflection angle slightly differs from the Brewster angle, we no longer have $r_\perp = \frac{n_1^2-n_2^2}{n_1^2+n_2^2}$ and $r_{\shortparallel} = 0$, and the Mueller matrix associated with the reflection becomes that of an imperfect polarizer. The light after the first reflection would in this case be slightly depolarized, and we can split the beam into the sum of a totally polarized beam and a totally depolarized one (cf. section 4.4.2.3, [62, 63]). Applying system 7.1 to $\mathbf{S_{in}} = [1;0;0;0]$ we obtain:

$$\begin{aligned} S &= \begin{bmatrix} (r_\perp+\Delta r_\perp)^2 + (r_{\shortparallel}+\Delta r_{\shortparallel})^2 \\ (r_\perp+\Delta r_\perp)^2 - (r_{\shortparallel}+\Delta r_{\shortparallel})^2 \\ 0 \\ 0 \end{bmatrix} \\ &= \left((r_\perp+\Delta r_\perp)^2 - (\Delta r_{\shortparallel})^2\right) \begin{bmatrix} 1 \\ 1 \\ 0 \\ 0 \end{bmatrix} + 2(\Delta r_{\shortparallel})^2 \begin{bmatrix} 1 \\ 0 \\ 0 \\ 0 \end{bmatrix} \end{aligned} \tag{7.9}$$

The depolarized light would of course not be modified by any polarizing element save the output Brewster angle, and would result in an output intensity offset. The totally polarized fraction of the light would propagate in the system as described before and result in an output intensity described by a slightly different version of equation 7.7 with a multiplicative factor modified as in 7.9.

Differentiating equations 5.6 and 5.9 with respects to θ_i and taking the Taylor expansions at $\theta_i = \theta_B + \Delta\theta_B$ yields error $\Delta r_\perp \approx r_\perp(\theta_B + \Delta\theta_B) - r_\perp(\theta_B)$ on the reflection coefficients as:

$$\Delta r_\perp \approx \frac{2n_1/n_2}{(n_2/n_1)^2+1}\Delta\theta_B \tag{7.10}$$

If we use the "ideal" ratio of indices of refraction as before, i.e. $n_1/n_2 = 1.4966$, equation 7.10 yields $\Delta r_\perp \approx 2.07\Delta\theta_B$, and equation 5.12 $r_\perp(\theta_B) \approx 0.383$. As for the parallel component, it is easier to work $\Delta r_{\shortparallel}^2$ than with $\Delta r_{\shortparallel}$; since $r_{\shortparallel}(\theta_B) = 0$ we have $(r_{\shortparallel}+\Delta r_{\shortparallel})^2 = r_{\shortparallel}^2 + (\Delta r_{\shortparallel})^2 + 2r_{\shortparallel}\Delta r_{\shortparallel} = (\Delta r_{\shortparallel})^2 =$

$r_{\shortparallel}^2 + \Delta r_{\shortparallel}^2$ and so the two terms are equivalent, $(\Delta r_{\shortparallel})^2 = \Delta r_{\shortparallel}^2$. A quadratic fit on equation 5.10 squared yields $\Delta r_{\shortparallel}^2 \approx 1.93(\Delta\theta_B)^2$. Using these values the Stokes vector 7.9 becomes:

$$S \approx \big(0.147 + 1.58\Delta\theta_B + 2.35(\Delta\theta_B)^2\big) \begin{bmatrix} 1 \\ 1 \\ 0 \\ 0 \end{bmatrix} + 3.86(\Delta\theta_B)^2 \begin{bmatrix} 1 \\ 0 \\ 0 \\ 0 \end{bmatrix}$$

This amounts to the unpolarized light generating and intensity that corresponds to a pressure offset at the output, assuming a perfect angle for the second Brewster reflection, of:

$$\frac{\Delta P}{P_{max}} \approx \frac{3.86\,(\Delta\theta_B)^2}{2\pi\,(0.147 + 1.58\Delta\theta_B + 2.35(\Delta\theta_B)^2)} \tag{7.11}$$

which, for instance taking an 1° error on the angle as before, represents a 0.21% full-scale measurement error. Once again this is a systematic error that can be calibrated for.

7.2.1.3 Light source collimation

Another source of geometry error is the angular spread of the light source.

So far we have always considered a perfectly collimated beam of light, but a real source will emit over an angular aperture. Each ray of light will meet the different interfaces at a slightly incorrect angle, and the result will be exactly as if there was an error on the inclination of the interfaces and produce the results discussed previously. Each ray can be treated independently from the others, and their total effect on the measurement error is the integration of their individual errors, with a proportionality coefficient that represents the fraction of the total intensity that corresponds to a given angle, over the aperture of the source.

The aperture can be easily controlled in practice by using diaphragms of suitable sizes in front of the source and of the detector. Another method is to use additional collimation/imaging optics that can be directly integrated by modifying the mold.

7.2.2 Influence of temperature

7.2.2.1 ... on the index of refraction

In general, the refraction index depends on the temperature in a complex manner. One widely used model is that of Prod'homme [64]. For polymers there exists a linear relationship, derived from the Lorentz-Lorenz equation, between the temperature, the linear thermal expansion coefficient of the material and a polynomial that contains the index of refraction [65, 66]:

$$\frac{n^2+2}{n^2-1} = \alpha_L(T - T_{ref}) + b \tag{7.12}$$

where n is the index of refraction, T the temperature, α_L the linear expansion coefficient and b a constant offset found by $b = (n_{ref}^2+2)/(n_{ref}^2-1) - \alpha_L T_{ref}$ when a reference index n_{ref} for the material is known at a reference temperature T_{ref}. α_L is constant over wide ranges of temperature between transition points in the polymer [67, 66, 65].

Using the values from [66] as an example, differentiating equation 7.12 for PMMA with $n_{(T=0°\mathrm{C})} = 1.4948$ yields an almost constant thermo-optic coefficient between -20°C and 70°C, $dn/dt \approx -1.2 \times 10^{-4} K^{-1}$. Over the same temperature range, the index of refraction varies between $n_{(T=-20°\mathrm{C})} = 1.4972$ and $n_{(T=95°\mathrm{C})} = 1.4834$.

Since the Brewster angles are dependent on the refractive indices, a temperature induced variation of n is equivalent to an error on the angles. Setting $n_2 = 1$ in equation 5.11 and differentiating with respects to temperature, we obtain:

$$\frac{d\theta_B}{dT} = \frac{1}{1+n_1^2}\frac{dn_1}{dT}$$

i.e. for PMMA:

$$\Delta\theta_B \approx -3.71 \times 10^{-5} \Delta T$$

which yields an angle error over the -20°C / +70°C temperature range comprised between +0.04° and −0.15°. The corresponding errors on the measured pressure are calculated as before using equation 7.11 and we obtain between $2.28 \times 10^{-4}\%$ and $2.9 \times 10^{-3}\%$ of P_{max}.

As for the “semi-circularizing” reflections, we can directly estimate the effect on the phase shift by differentiating 5.18 to obtain:

$$\frac{d\delta_r}{dT} = \frac{2 \cdot \tan(\frac{1}{2}\delta_r) \cdot \cos^2(\frac{1}{2}\delta_r)}{n_1^3(\sin(\theta_{sc}) - 1/n_1^2)} \frac{dn_1}{dT}$$

or, with the numerical values used before, $d\delta_r/dT \approx -1.48 \times 10^{-4} K^{-1}$. Since $P/P_{max} = \Delta\varphi/2\pi$, the equivalent full-scale error on the measured pressure is,

$$\frac{\Delta P}{P_{max}} = \frac{1}{2\pi} \cdot \frac{d\delta_r}{dT} \cdot \Delta T \approx -2.36 \times 10^{-5} \Delta T$$

which is comprised between 0.047% and -0.17% of P_{max} for T between -20°C and 70°C.

7.2.2.2 ... on the piezo-optic coefficients

It has been reported in [68, 69], and experimentally verified in[57] for PMMA, that the piezo-optic coefficient $C = \frac{1}{2}n^3(p_{11} - p_{12})$ varies linearly with the temperature as long as it doesn’t get too close to the transition temperatures [70]. In most optical plastics the glass transition temperature is typically around 100°C [53, pp. 122-147], a good margin from our maximum temperature of 70°C.

The temperature dependence of the piezo-optic coefficients for different materials is not easily found in the literature, but some examples for silica glass [71, 72, 73] and PMMA [74, 57] are available. To get a sense of the order of magnitude of the thermal effect, we can extract the values of the variation of C with temperature from [57] and we obtain for PMMA:

$$\begin{cases} C_{(T=20°\mathrm{C},\lambda=650nm)} = 1.2 \times 10^{-12}\, Pa^{-1} \\ \frac{dC}{dT} = 6.9 \times 10^{-15}\, Pa^{-1}\, K^{-1} \end{cases}$$

Differentiating 6.3 with regards to C we obtain the relative error on the measured pressure:

$$\frac{\Delta P}{P} = \frac{\Delta C}{C} = \frac{1}{C}\frac{dC}{dT}\Delta T \tag{7.13}$$

which for PMMA using the values given above, results in $\Delta P/P \approx 5.75 \times 10^{-3}\Delta T$. This is equivalent to a relative error on the measured pressure of -23% at -20°C and +29% at 70°C. These values are very high compared to any of the other sources of errors we have seen so far, and it follows that one of the most important factors in choosing the dielectric material has to be the thermal sensitivity of the piezo-optic coefficients. In practice this is the key point in the choice of the dielectric material for the sensor.

7.2.2.3 ... on the elastic deformation

The mechanical properties of polymers in general, and PMMA in particular, have been extensively studied [75, 76, 54, 58, 59]. Their elastic properties vary slowly as long as the temperature is not too close to the transition temperatures[77]. This remains typically correct as long as the temperature is at least 20K below the glass transition temperature. In this domain, using the model proposed by Seitz [78, 70], the values for PMMA given in [70, sec. ll.B.2.b], and a linear regression over -20°C / +70°C, we obtain the temperature variation of the Poisson ratio:

$$\begin{cases} \nu_{(T=23°C)} = 0.354 \\ \frac{d\nu}{dT} = 2.18 \times 10^{-4} K^{-1} \end{cases}$$

The relative error on pressure is, differentiating 6.3 with regards to ν,

$$\frac{\Delta P}{P} = \frac{-1}{(1-\nu)(1-2\nu)} \frac{d\nu}{dT} \Delta T \tag{7.14}$$

i.e. $\Delta P/P \approx -1.16 \times 10^{-3} \Delta T$. This corresponds to a relative error of +5.2% at -20°C and -5.2% at +70°C.

The Young modulus also varies with temperature. Even though the response of our sensor does not depend on it due to the particular geometrical configuration we considered, it is useful to know it behaves. There exists a good model that works across transition temperatures [79], but since we limit ourselves to a ranger lower than the glass transition we can use a simpler representation valid over than range [79, 54, 75, 80]:

$$\frac{E(T)}{E(T_{ref})} = \frac{T_g/T_{ref} + 2}{T_g/T_{ref} + 2T/T_{ref}} \tag{7.15}$$

where T_{ref} is the reference temperature at which a value of the Young modulus is known, T_g is the glass transition temperature of the polymer and T is the temperature in Kelvin.

Another important effect of a temperature change is thermal dilatation. The linear thermal expansion coefficient α_L is defined as:

$$\alpha_L = \frac{1}{L}\frac{dL}{dT}$$

where L is the dimension which dilatation we are considering. Modifying the Hooke's law system of equations 6.1 to take the thermal expansion into account yields:

$$\delta_y = \frac{1}{E}\left(\sigma_y - \nu(\sigma_x + \sigma_z)\right) + \alpha_L \Delta T$$

and ultimately:

$$\sigma_x - \sigma_y = \frac{1-2\nu}{1-\nu}\left(P - \frac{E\cdot\alpha_L}{1-2\nu}\Delta T\right)$$

which has the total effect of adding a negative temperature dependent offset to the measured pressure:

$$\triangle P = -\frac{E\cdot\alpha_L}{1-2\nu}\Delta T \tag{7.16}$$

Typical values of for PMMA are $\alpha_L \approx 7\times10^{-5}K^{-1}$ and $E \approx 3\times10^{9}Pa$ [53, pp. 122-147] which yields a temperature-induced offset on the measured pressure $\triangle P \approx -7.2\times10^{5}\Delta T$, or 7.2 bars per Celsius degree. This is of course an unacceptable error value that would overshadow any pressure measurement, simple geometrical changes can be made to physically remove this effect.

One such change is to add a second identical pressure sensitive section in the optical path right after the first one. The only differences is that the free face would not be subjected to pressure (or rather, it would be subjected to ambient pressure) and oriented perpendicularly to the first one, i.e. along the **x** axis instead of **y**. This way, the two sections add a temperature dependent phase of the exact same value but of opposite sign: the two effects exactly compensate each other and the temperature induced pressure offset disappears.

A second method is to let the the dielectric expand in all directions in the volume that interacts with the light. This is equivalent to having an unconstrained cylinder while maintaining a seal at the top of the sensor where it is in contact with the fluid under pressure. In this configuration equation 6.3 becomes:

$$\triangle\varphi = \frac{2\pi}{\lambda} \cdot d \cdot \triangle n = \frac{2\pi}{\lambda} \cdot d \cdot C \cdot (\sigma_x - \sigma_y) = \frac{2\pi}{\lambda} \cdot d \cdot C \cdot P$$

In this configuration the dependence on the Poisson ratio vanished, removing one source of uncertainty and slightly increasing the sensitivity. As we mentioned the effect of the thermal dilatation is also negated since the material can freely expand in all directions.

Part IV

Experimental Validation

Introduction

We now propose to experimentally validate the concept of a piezo-optic pressure sensor that we presented and modelized in part III.

To analyze the polarization effects of various optical elements we first describe the realization and calibration of a Mueller polarimeter, an experimental tool that allows us to obtain the Mueller matrix of a component. The polarimeter we built is a dual rotating compensators[1] polarimeter: the light passes through a fixed linear polarizer, then through a quarter-wave plate that can be rotated to any angle, then though the sample to the analyzed, and then through a symmetric setup: a rotated quarter-wave plate and a fixed polarizer. Finally the output intensity is read from a photodetector. We present the experimental setup and its specificities, the calibration of the elements, the compensation of errors in the Mueller coefficients reconstruction method, and finally the measured Mueller matrix of the "void", i.e. with no sample, to validate the polarimeter.

In Chapter 9 we describe one experimental realization of the proposed pressure sensor in order to validate the measurement principle.

---

[1] waveplates

Chapter 8

Mueller polarimeter

In this chapter, we describe the experimental realization of a Mueller polarimeter. We first describe the theoretical behavior of a rotating compensators polarimeter and explain how the Mueller coefficients can be recovered using a 2D Fourier Transform. We then describe the actual realization of our polarimeter, the calibration of the elements and the compensation of their defects. Finally we extract a Mueller matrix with no sample in the polarimeter in order to validate its performances.

8.1 Measurement of Mueller coefficients using a dual rotating compensators polarimeter

8.1.1 Choice of polarimeter configuration

There are various ways to obtain the Mueller matrix of an element, but the general method is always the same: a polarization generator creates known states of polarization, the light propagates through (or reflects on) the sample, and the resulting state of polarization is determined by a polarization analyzer. By repeating this analysis for several input states of polarization, the Mueller coefficients of the sample can be determined. A good overview of the various existing methods with key references has been written by Chipman [81, chp. 15].

We have selected to use a very popular polarimeter, a dual rotating compensator polarimeter. In this configuration a light source shines through a fixed linear polarizer, then through a rotating waveplate, then through the sample, then through a second rotating waveplate and finally through another fixed linear polarizer. In our polarimeter, schematically represented on figure 8.1, the entrance polarizer has its transmission axis horizontal and the exit polarizer has his vertical. The two waveplates are quarter-wave plates (the optimal retardance to minimize errors is around 127° [82] but such waveplates were not available to us) that can be rotated independently from each other, in contrast with a popular type of polarimeter where they have a fixed $\theta_{wp1} = 5\theta_{wp2}$ relationship [83, 84].

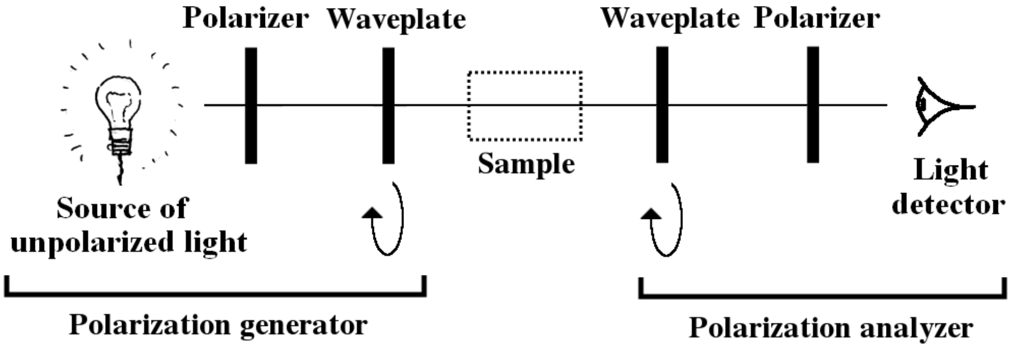

Figure 8.1: Principle of the dual rotating compensators polarimeter.

This configuration provides several advantages. The main one comes from the fact that the two polarizers are fixed: this renders the polarimeter insensitive to the eventual polarization effects of optical components before and after the polarimeter itself as it ensures that the light after the first polarizer will always be polarized in the same manner, and likewise for the light after the second polarizer. This is most important if the input light is not perfectly unpolarized, which is never the case in practice, and when there are collection optics behind the polarimeter that will have an eventual polarization response.

A second advantage of this configuration is that, as will be explained in the next section, the Mueller coefficients can be obtained by applying a Fourier Transform to the experimentally measured intensities. This method is simple, robust, and a fast algorithm to compute it, the Fast Fourier Transform, exists. Increasing the number of sample points increases the precision on the coefficients without requiring the inversion of a large matrix as in a direct inversion method, and information about the sources of measurement errors can be found in the Fourier coefficients that should theoretically be zero but are not due to imperfections in the polarimeter.

8.1.2 Computation of the Mueller coefficients

Using the Mueller matrices from Chapter 4, the Mueller matrix of an ideal polarimeter is given by:

$$\mathbf{M_{ideal}} = \mathbf{M}_{polv} \cdot \mathbf{M}_{QWP}\left(\theta_A\right) \cdot \mathbf{M}_{sample} \cdot \mathbf{M}_{QWP}\left(\theta_G\right) \cdot \mathbf{M}_{polh} \tag{8.1}$$

After carrying out the matrix multiplications and only looking at the intensity of the output light for an unpolarized input light of intensity I_0 we obtain equation 8.2:

$$\begin{aligned}
\frac{I_{ideal}}{I_0} = & \sin(2\theta_G) \cdot \left(\frac{1}{4}m_{13} + \frac{1}{2}m_{03} - \frac{1}{2}m_{33}\sin(2\theta_A) + \frac{1}{4}m_{13}\cos(4\theta_A) + \frac{1}{4}m_{23}\sin(4\theta_A)\right) \\
& + \cos(4\theta_G) \cdot \left(-\frac{1}{4}m_{01} - \frac{1}{8}m_{11} + \frac{1}{4}m_{31}\sin(2\theta_A) - \frac{1}{8}m_{11}\cos(4\theta_A) - \frac{1}{8}m_{21}\sin(4\theta_A)\right) \\
& + \sin(4\theta_G) \cdot \left(\frac{1}{4}m_{02} + \frac{1}{8}m_{12} - \frac{1}{4}m_{32}\sin(2\theta_A) + \frac{1}{8}m_{12}\cos(4\theta_A) + \frac{1}{8}m_{22}\sin(4\theta_A)\right) \\
& + \left(-\frac{1}{8}m_{11} + \frac{1}{4}m_{10} - \frac{1}{4}m_{01} + \frac{1}{2}m_{00}\right) \\
& + \left(\frac{1}{4}m_{31} - \frac{1}{2}m_{30}\right) \cdot \sin(2\theta_A) \\
& + \left(\frac{1}{4}m_{10} - \frac{1}{8}m_{11}\right) \cdot \cos(4\theta_A) \\
& + \left(\frac{1}{4}m_{20} - \frac{1}{8}m_{21}\right) \cdot \sin(4\theta_A)
\end{aligned} \tag{8.2}$$

in which we have factored $\cos(n\theta_G)$ and $\sin(n\theta_G)$. It is immediately visible that we can extract the coefficients of the harmonic functions of θ_G by Fourier Transform (FT). Likewise, a second FT on the resulting coefficients that only depend on θ_A will yield a combination of the Mueller coefficients of the sample, and this provides a simple method to obtain the coefficients: rotate the two waveplates, record the intensities for each combination of angles in a matrix and perform a 2D FT on it. The Mueller coefficients are then obtained by simple manipulations of the Fourier coefficients.

One important point to note is that while the first FT acts on real values, and will thus always output conjugate coefficients for the positive and negative frequencies, the second one does not: the negative part of the resulting spectrum is not redundant can not be ignored, it is necessary to obtain all the Mueller coefficients.

The Fourier coefficients calculated from equation 8.2 are presented on table 8.1. We separated the real and imaginary part of each coefficient to simplify reading. The coefficients for harmonics not represented in the table are zero. We will refer to each Fourier coefficient by $f_{Fg,Fa}$ where Fg and Fa are the normalized frequencies of, respectively, the polarization generator and analyzer with regards to the "unit" frequency that corresponds to one turn of a waveplate. Using this notation, coefficient $f_{2,-2}$ in the table is for instance equal to $-\frac{1}{8}m_{33}$.

		Fa				
		0	2	4	-4	-2
Fg	0	$-\frac{1}{8}m_{11}+\frac{1}{4}m_{10}-\frac{1}{4}m_{01}+\frac{1}{2}m_{00}$	$\left\{\frac{1}{8}m_{31}-\frac{1}{4}m_{30}\right\}i$	$-\frac{1}{16}m_{11}+\frac{1}{8}m_{10}$ $\left\{-\frac{1}{16}m_{21}+\frac{1}{8}m_{20}\right\}i$	$-\frac{1}{16}m_{11}+\frac{1}{8}m_{10}$ $\left\{\frac{1}{16}m_{21}-\frac{1}{8}m_{20}\right\}i$	$\left\{-\frac{1}{8}m_{31}+\frac{1}{4}m_{30}\right\}i$
	2	$\left\{\frac{1}{8}m_{13}+\frac{1}{4}m_{03}\right\}i$	$\frac{1}{8}m_{33}$	$-\frac{1}{16}m_{23}$ $\left\{\frac{1}{16}m_{13}\right\}i$	$\frac{1}{16}m_{23}$ $\left\{\frac{1}{16}m_{13}\right\}i$	$-\frac{1}{8}m_{33}$
	4	$-\frac{1}{16}m_{11}-\frac{1}{8}m_{01}$ $\left\{\frac{1}{16}m_{12}+\frac{1}{8}m_{02}\right\}i$	$\frac{1}{16}m_{32}$ $\left\{\frac{1}{16}m_{31}\right\}i$	$-\frac{1}{32}m_{11}-\frac{1}{32}m_{22}$ $\left\{-\frac{1}{32}m_{21}+\frac{1}{32}m_{12}\right\}i$	$-\frac{1}{32}m_{11}+\frac{1}{32}m_{22}$ $\left\{\frac{1}{32}m_{21}+\frac{1}{32}m_{12}\right\}i$	$-\frac{1}{16}m_{32}$ $\left\{-\frac{1}{16}m_{31}\right\}i$
	-4	$-\frac{1}{16}m_{11}-\frac{1}{8}m_{01}$ $\left\{-\frac{1}{16}m_{12}-\frac{1}{8}m_{02}\right\}i$	$-\frac{1}{16}m_{32}$ $\left\{\frac{1}{16}m_{31}\right\}i$	$-\frac{1}{32}m_{11}+\frac{1}{32}m_{22}$ $\left\{-\frac{1}{32}m_{21}-\frac{1}{32}m_{12}\right\}i$	$-\frac{1}{32}m_{11}-\frac{1}{32}m_{22}$ $\left\{\frac{1}{32}m_{21}-\frac{1}{32}m_{12}\right\}i$	$\frac{1}{16}m_{32}$ $\left\{-\frac{1}{16}m_{31}\right\}i$
	-2	$\left\{-\frac{1}{8}m_{13}-\frac{1}{4}m_{03}\right\}i$	$-\frac{1}{8}m_{33}$	$\frac{1}{16}m_{23}$ $\left\{\frac{1}{16}m_{13}\right\}i$	$-\frac{1}{16}m_{23}$ $\left\{-\frac{1}{16}m_{13}\right\}i$	$\frac{1}{8}m_{33}$

Table 8.1: Frequency content of the intensity at the output of the polarimeter. The reference unity frequency corresponds to one full turn of the waveplates. Fg (lines) indexes the frequencies relative to the rotation of the polarization generator's waveplate. Fa (columns) indexes the frequencies relative to the rotation of the analyzer's waveplate.

Setting m_{00} to 1 to normalize the reconstructed Mueller matrix with regards to a constant attenuation, we then obtain from table 8.1 the Mueller coefficients:

$$m_{00} = 1 \tag{8.3}$$
$$m_{01} = 8 \cdot \Re\left\{ f_{0,4} - \frac{1}{2} f_{0,0} + \frac{1}{4} \right\} \tag{8.4}$$
$$m_{02} = 8 \cdot \Im\left\{ f_{4,0} + f_{-4,4} + f_{-4,-4} \right\} \tag{8.5}$$
$$m_{03} = 4 \cdot \Im\left\{ f_{2,0} - 2 \cdot f_{2,4} \right\} \tag{8.6}$$
$$m_{10} = 8 \cdot \Re\left\{ f_{4,0} - \frac{1}{2} f_{0,0} + \frac{1}{4} \right\} \tag{8.7}$$
$$m_{11} = 16 \cdot \Re\left\{ \frac{1}{2} f_{0,0} - f_{4,0} - f_{0,4} - \frac{1}{4} \right\} \tag{8.8}$$
$$m_{12} = 16 \cdot \Im\left\{ -f_{-4,4} - f_{-4,-4} \right\} \tag{8.9}$$
$$m_{13} = 16 \cdot \Im\left\{ f_{2,4} \right\} \tag{8.10}$$
$$m_{20} = 8 \cdot \Im\left\{ f_{0,4} + f_{4,-4} + f_{-4,-4} \right\} \tag{8.11}$$
$$m_{21} = 16 \cdot \Im\left\{ f_{4,-4} + f_{-4,-4} \right\} \tag{8.12}$$
$$m_{22} = 16 \cdot \Re\left\{ \frac{1}{4} - \frac{1}{2} \cdot f_{0,0} + f_{4,0} + f_{0,4} - 2 \cdot f_{4,4} \right\} \tag{8.13}$$
$$m_{23} = 16 \cdot \Re\left\{ -f_{2,4} \right\} \tag{8.14}$$
$$m_{30} = 4 \cdot \Im\left\{ 2 \cdot f_{4,2} - f_{0,2} \right\} \tag{8.15}$$
$$m_{31} = 16 \cdot \Im\left\{ f_{4,2} \right\} \tag{8.16}$$
$$m_{32} = 16 \cdot \Re\left\{ f_{4,2} \right\} \tag{8.17}$$
$$m_{33} = 8 \cdot \Re\left\{ f_{2,2} \right\} \tag{8.18}$$

where $\Re\{\cdot\}$ denotes the real part and $\Im\{\cdot\}$ the imaginary part.

8.1.3 imperfect compensators

When the retardance of the waveplates is not exactly $\pi/2$, the above relationships are modified. Mueller polarimeters with imperfect compensators and other sources of errors have been extensively studied [85, 86, 83, 87, 88, 82]. The dominant sources of measurement errors are small errors on the relative angular positions of the different elements as well as the non ideal retardation of the waveplates [86]; of those, in our case, only the angle of the exit polarizer and the retardations of the waveplates are systematic errors, and according to [86] the waveplates should be the main sources of error.

In general the errors on the Fourier coefficients due to imperfect compensators will depend on the Mueller matrix being measured. To simplify the problem here, we only check the effect on the measurement of the "no sample" Mueller matrix, i.e. the identity matrix.

Using a small angle approximation on Mueller matrix 4.39, the Mueller matrix of an imperfect quarter-wave plate is:

$$\mathbf{M}_{WP}\left(\frac{\pi}{2}-\varepsilon,\theta\right)=\begin{bmatrix}1 & 0 & 0 & 0\\ 0 & \cos^2(2\theta)+\varepsilon\sin^2(2\theta) & (1-\varepsilon)\cos(2\theta)\sin(2\theta) & \sin(2\theta)\\ 0 & (1-\varepsilon)\cos(2\theta)\sin(2\theta) & \varepsilon\cos^2(2\theta)+\sin^2(2\theta) & -\cos(2\theta)\\ 0 & -\sin(2\theta) & \cos(2\theta) & \varepsilon\end{bmatrix}$$

which can be mathematically decomposed in the sum of the Mueller matrix of a perfect quarter-wave plate and of an error matrix:

$$\begin{aligned}\mathbf{M}_{WP}\left(\frac{\pi}{2}-\varepsilon,\theta\right)&=\mathbf{M}_{QWP}(\theta)+\varepsilon\cdot\begin{bmatrix}0 & 0 & 0 & 0\\ 0 & \sin^2(2\theta) & \cos(2\theta)\sin(2\theta) & 0\\ 0 & \cos(2\theta)\sin(2\theta) & \cos^2(2\theta) & 0\\ 0 & 0 & 0 & 1\end{bmatrix}\\ &=\mathbf{M}_{QWP}(\theta)+\mathbf{M}_{\Delta}(\varepsilon,\theta)\end{aligned}$$

Equation 8.1 becomes:

$$\begin{aligned}\mathbf{M}&=\mathbf{M}_{polv}\cdot\mathbf{M}_{WP}\left(\frac{\pi}{2}-\varepsilon_A,\theta_A\right)\cdot\mathbf{Id}\cdot\mathbf{M}_{WP}\left(\frac{\pi}{2}-\varepsilon_G,\theta_G\right)\cdot\mathbf{M}_{polh}\\ &=\mathbf{M}_{polv}\cdot\left(\mathbf{M}_{QWP}(\theta_A)+\mathbf{M}_{\Delta}(\varepsilon_G,\theta_G)\right)\cdot\mathbf{Id}\cdot\left(\mathbf{M}_{QWP}(\theta_G)+\mathbf{M}_{\Delta}(\varepsilon_G,\theta_G)\right)\cdot\mathbf{M}_{polh}\end{aligned}$$

which decomposes in the sum of the Mueller matrix of the ideal polarimeter and of several other terms that depend on the error matrices. Consequently, computing the intensity at the exit of the polarimeter yields a sum of the ideal intensity and of three error intensity terms that depend respectively on ε_A, ε_G and $\varepsilon_A\varepsilon_G$. The cross term will be negligible in front of the two others so we neglect it from now on. Carrying out the calculation that we do not detail here, the errors on intensity due to the retardance errors are respectively:

$$\Delta I_G=\frac{\varepsilon_G}{16}\left(-1+\cos(4\theta_G)-\cos(4\theta_A)+\cos(4\theta_G)\cos(4\theta_A)+\sin(4\theta_G)\sin(4\theta_A)\right)$$

and:

$$\Delta I_{GA} = \frac{\varepsilon_A}{16}\left(-1 - \cos(4\theta_G) + \cos(4\theta_A) - \cos(4\theta_G)\cos(4\theta_A) + \sin(4\theta_G)\sin(4\theta_A)\right)$$

Due to the linearity of the Fourier transform, this directly results in the errors, listed in table 8.2, on the Fourier coefficients:

		Fa		
		0	4	-4
Fg	0	$\frac{1}{16}(\varepsilon_G + \varepsilon_A)$	$\frac{1}{32}(\varepsilon_G - \varepsilon_A)$	$\frac{1}{32}(\varepsilon_G - \varepsilon_A)$
	4	$\frac{1}{32}(\varepsilon_A - \varepsilon_G)$	$\frac{1}{32}\varepsilon_A$	$-\frac{1}{32}\varepsilon_G$
	-4	$\frac{1}{32}(\varepsilon_A - \varepsilon_G)$	$-\frac{1}{32}\varepsilon_G$	$\frac{1}{32}\varepsilon_A$

Table 8.2: Errors caused by imperfect compensators on the Fourier coefficients when measuring the "void" Mueller matrix.

Inserted these errors into equations 8.3-8.18, we obtain the measured Mueller matrix with no sample in the polarimeter:

$$\mathbf{M}_{void} = \begin{bmatrix} 1 & -\frac{1}{2}\varepsilon_A & 0 & 0 \\ -\frac{1}{2}\varepsilon_G & 1 + \frac{1}{2}(\varepsilon_A + \varepsilon_G) & 0 & 0 \\ 0 & 0 & 1 - \frac{1}{2}(\varepsilon_A + \varepsilon_G) - \varepsilon_A & 0 \\ 0 & 0 & 0 & 1 \end{bmatrix}$$

8.2 Experimental realization of the polarimeter

8.2.1 Description of the experimental setup

The experimental setup is pictured on figure 8.2 below. The datasheets for the various components are available in Annex E. The polarization generator and analyzer are separated on two Newport X26 rails so as to be independent from each other. In between is a heating apparatus with a temperature sensor feedback on which is placed a metal cell with two 5mm clear aperture windows; this enables control of the temperature in the cell while Mueller measurements are performed on the sample placed inside.

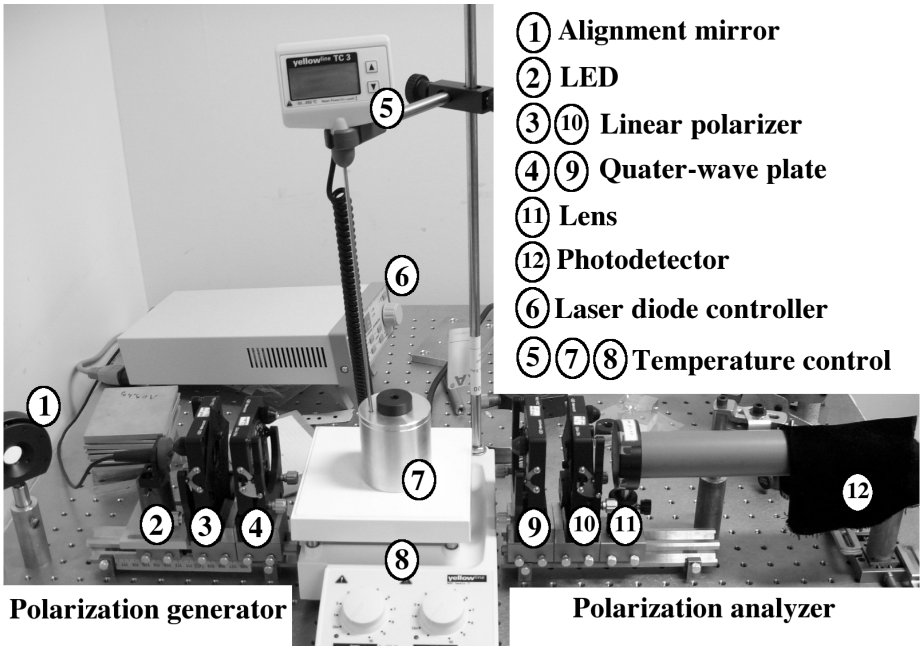

Figure 8.2: Photography of the polarimeter. A sample that has to be characterized at a given temperature can be put in the heated cell (7).

The light source is a L7868-02 red LED by HAMAMATSU, equipped with a glass lens window to obtain a small beam divergence (typically ±1° at 50% intensity). Its emission is centered on 670nm with a 20nm spectral half width. The LED is alimented by a laser diode controller in constant current mode in order to obtain a light intensity as stable as possible. The controller is a Thorlabs LDC202B that can provide up to 200mA with an accuracy of ±0.1mA and fluctuations at a set current inferior to 10µA. The stability of the source was checked by recording the measurement signal over 12 hours. No variation above the resolution of the recording instrument was found.

The polarizers are TechSpec linear polarizers from Edmund Optics, with announced extinction ratio 10000:1 at visible wavelength. The two quarter-wave plates are optimized for 670nm and were also provided by Edmund Optics with an announced precision of 1/500th wavelength retardance error. Both elements were experimentally calibrated and the results are presented in the next section. They are mounted on manual rotation stages with vertical and horizontal tilt tuning knobs, and were aligned using the retro-reflection at about three meters of a laser beam on their surface.

The detector is a HAMAMATSU S7183 photodiode with an integrated current amplifier that amplifies the photocurrent up to 1300 times, allowing direct current measurements without additional amplification under low illumination conditions. The detector was alimented by a battery to minimize voltage fluctuations, and the whole device put inside an isolated metal box so as to form a floating sensor. It was connected to a Metrix MTX3250 precision multimeter (0.08% announced accuracy) through a shielded foiled twisted pairs cable to avoid electromagnetic induction noise.

Particular steps were taken to minimize various sources of errors. Various screw holes in the rotating stages were sealed to avoid stray light, and the walls inside the windows of the temperature-controlled cell were blackened to minimize reflections. One source of error in non-imaging polarimeters is the light reflected and diffused on the apertures of the optical elements: its polarization is modified by the interaction with the edges and generates an error on the real state of polarization we want to measure. An example of this effect is shown on figure 8.3. To avoid this problem, we added a diaphragmed lens between the exit polarizer and the detector. The lens focal length, position and diaphragm aperture were calculated so that the marginal rays seen by the detector would always be inside of the apertures of the elements of the system; in practice the most limiting apertures are the windows of the temperature-controlled cell, and the system was calculated so that the center of the cell is imaged on the detector. This configuration has the added benefices of strictly limiting the sources of parasite light that influence the detector, as well as of limiting the inclination of the observed rays; this serves to minimize the effect of the optics on non perpendicular rays and to ensure that we observe waves that are close to plane waves. In practice, the most inclined rays seen by the detector make angle angle smaller than 3° with the optical axis. This was checked by placing opaque screens at different positions on the various apertures of the system while recording the intensity on the detector: it would start to drop when the screen entered the portion of the aperture that was “visible” by the detector.

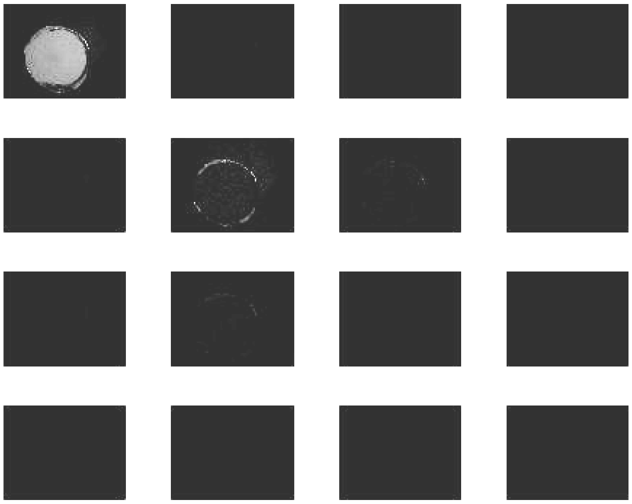

Figure 8.3: Mueller image of a depolarizer in a metal holder. The repolarizing effect of edge reflections is clearly visible on m_{11} and slightly on m_{12} and m_{21}. (Image courtesy of Y. TAKAKURA)

8.2.2 Calibration and adjustment of the elements of the polarimeter

8.2.2.1 Photodetector

Since the photodetector has an integrated current amplifier, it is very sensitive even for very small illuminations. The detection circuit can thus be a simple battery and a resistance in series with the detector. The measured signal is the tension value is across the resistance, read by a low-noise operational amplifier in voltage follower configuration. As mentioned before, we use a battery which is a very stable source of tension to minimize the power source noise; moreover the whole circuit was put inside a conducting box and connected to the external voltmeter through a shielded foiled twisted pairs cable (each twisted pair is wrapped in a conducting foil, and the whole cable is itself shielded) to minimize the influence of electromagnetic induction from environmental sources (mainly power outlets, fluorescent lights in the adjacent rooms, and heavy machinery in a workshop under the laboratory). References [89, 90, 91] give a good hands on overview of “do’s and don’t’s” when it comes to shielding a circuit from external sources of noise.

Calibration using a variable optical density filter was performed to check the linearity of the photodetector’s response. The log of the measured signal was taken, since an linearly varying optical density results in an exponential transmission coefficient, and the result plotted and fitted to a linear curve (see figure 8.4). It was found that it is linear within 0.1% over a wide range of light intensities, down to “no light” where the measured tension results from the dark current of the diode. The superimposed points correspond to the regions were two series of measurements have been superposed, which was necessary to explore the whole dynamic of the detector with a single variable optical density of limited maximum attenuation: between each series the power of the LED was reduced and the optical density reset to minimum attenuation. Near zero intensity the noise on the measured points

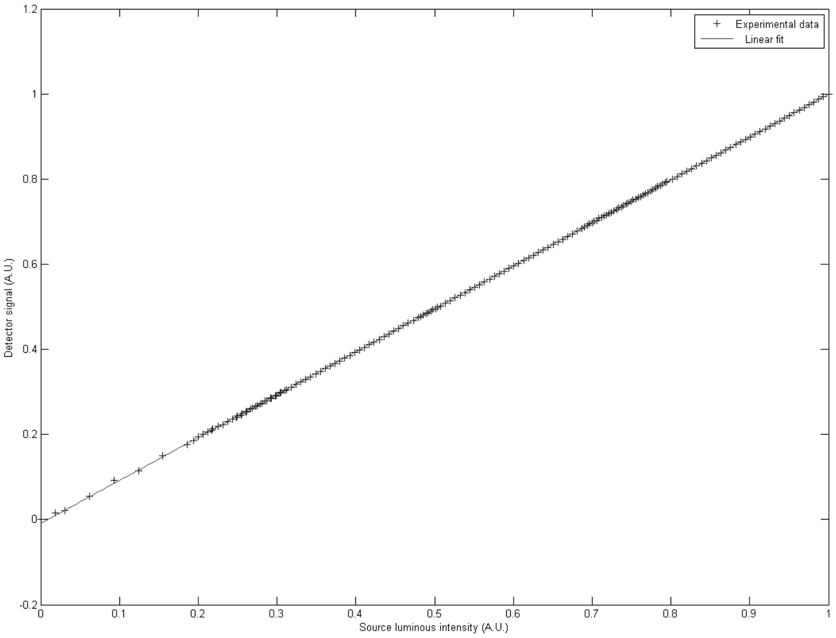

Figure 8.4: Test of the linearity of the photodetector at room temperature. All values in arbitrary normalized units.

is due to the instability of the source of current that powers the LED at low currents.

As the voltage across the resistance increases, the linearity drops; in practice this effect is not noticeable as long as the voltage across the photodetector is 5 Volts or above, i.e. as long as the voltage across the resistance is no closer than 5 Volts to the supplied voltage.

The value of the resistance was selected so that the maximum light intensity in the polarimeter, i.e. when both polarizers are aligned, would not force the detector outside of its linear response region. The voltage of the power supply was selected so that when there is no current in the circuit the voltage across the detector does not exceed the maximum tolerated value. The combination of these two choices ensures that we obtain the largest output voltage dynamic for our photodetector.

Measured values for the "dark voltage" and the "maximum voltage" across the resistance were respectively 0.02mV and 7.3V, which corresponds to a dark current of 0,2nA and a maximum current in the detector of 73µA.

8.2.2.2 Polarizers

The entrance polarizer was rotated to have its transmission axis horizontal. To ensure that the horizontal position was identified as well as possible we used the fact, presented in section 5.3, that the reflection coefficient for the parallel polarization is always smaller than for perpendicular polarization. We placed a PMMA cube, set on an horizontal rotation stage, on the path with it's first face perpendicular to the optical axis; the perpendicularity was checked by retro-reflection of the same alignment laser used to align the other elements and the deviation from vertical at the point of impact of the laser spot was minimized to less than 0.04°. The rotation stage was then rotated approximately to the Brewster angle of PMMA. In this configuration, the plane of incidence on the face of the cube was parallel to the ground, so any fraction of the incident light polarized parallel to the ground would be almost extinguished in the reflection. The polarizer was then rotated to minimize the intensity of the reflected light, i.e. until only parallel polarized light was reflecting on the cube. This method ensured that the polarizer was as horizontal as possible given the experimental setup.

The exit polarizer was set on the bench and rotated to minimize the intensity on the detector, i.e. to a position where its transmission axis was vertical. It was then rotated approximately to 90° of this orientation to obtain the maximum light intensity and set the resistance of the detector, before being set back to its crossed position.

The voltage was measured at the output of the detector for crossed and parallel polarizers to obtain the extinction ratio of the polarizers. It was found different combination of the direction the two sides of each polarizer faced slightly influenced the extinction ratio. The configuration selected in the end was the one that presented the best extinction ratio, close to 1:7000.

With crossed polarizers in this configuration, the voltage at the detector was measured to be 1.04mV. This is a factor 50 over the dark and noise levels, making them negligible in this application.

8.2.2.3 Waveplates

The two waveplates were supposed to be quarter-wave plates. There are various methods to calibrate waveplates [92, 93, 94, 95, 96, 97, 98] with various degrees of precision. We selected a method based on Fourier Transforms, as its precision increases with the number of measurement points and does not only depend on the precision of a few punctual intensity measurements as in several other methods.

To measure their exact retardance, we rotate each waveplate between the two polarizers positioned parallel to each other. The Mueller-Stokes calculus for this system gives for the output intensity:

$$I = I_0 \left(\frac{3}{4} + \frac{1}{4}\cos(\phi) + \frac{1}{4}(1 - \cos(\phi)) \cdot \cos(4\theta) \right) \tag{8.19}$$

where ϕ is the retardance of the waveplate and θ its orientation. We see that the intensity varies periodically with the angular position of the waveplate. A Fourier Transform on the measured intensity yields two coefficients f_0 and f_4 that correspond respectively to the amplitude of the constant intensity and to the amplitude of the periodic portion with a normalized frequency of 4. All the other coefficients are zero since only these two frequencies have non-null components. From these coefficients we directly deduce the retardance of the waveplate through equation 8.20:

$$\cos(\phi) = 2 \cdot \frac{f_0 - f_4}{f_0 + f_4} - 1 \tag{8.20}$$

Using this method, the retardances of the two waveplates were determined to be:

$$\begin{cases} \phi_G = \frac{\pi}{2} - \frac{\pi}{72.5} \\ \phi_A = \frac{\pi}{2} - \frac{\pi}{1987} \end{cases}$$

Figures 8.5 and 8.6 show the experimentally measured intensities versus the orientation of the waveplates, and the theoretical responses of a waveplate with the calculated retardance. The maxima and minima over a full rotation of the waveplates were at a constant level, a good indication that there is no noticeable diattenuation in the plates.

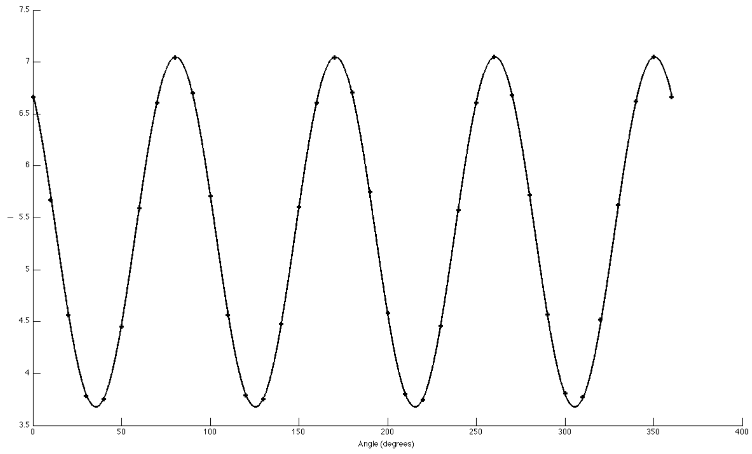

Figure 8.5: Comparison between the experimental intensity response of the first waveplate (squares) and the response of an ideal waveplate with the same estimated retardance (solid line). The intensities are in arbitrary units.

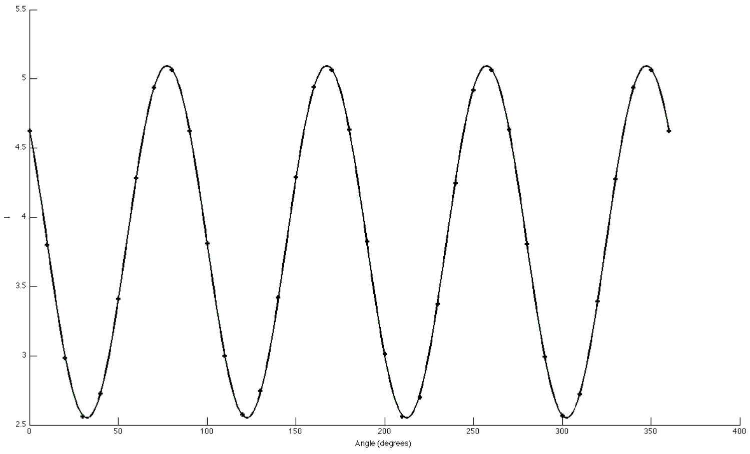

Figure 8.6: Comparison between the experimental intensity response of the second waveplate (squares) and the response of an ideal waveplate with the same estimated retardance (solid line). The intensities are in arbitrary units.

Something should be mentioned about the orientation of the two polarizers: they could also have been crossed, with less imprecision on their orientation since the operation involves a null-intensity measurement that is more precise than a maximum intensity measurement. But in this case the output intensity varies between "zero" and an unknown maximum, giving us no value with which to normalize the measured intensities. The value of the maximum could be obtained by measuring it when the two polarizers are parallel, but inserting the waveplate afterward would modify it by an unknown factor because of reflections on the faces of the element. In contrast, with the parallel polarizers the maximum intensity is always measured and the minimum intensity that we never directly measure is known since we know the extinction ratio of the polarizers.

Once the exact retardance of both waveplates had been determined, the two polarizers were once again crossed and the plates were placed in the polarimeter with their fast axes horizontal. The approximate position of the fast axis was indicated by a white dot on the side of each waveplate; it can alternately be determined by Tutton's test [99] or other methods [100, 101]. First the waveplate of the polarization generator was placed, and rotated to minimize the intensity on the detector so as to ensure that its fast axis was horizontal; this position was marked as the origin of rotation . The waveplate of the polarization analyzer was positioned in a similar manner.

8.2.3 Validation of the polarimeter: measurement of the matrix of the void

In order to validate the polarimeter as well as the error analysis performed above, we performed a series of measurement with no sample in the polarimeter in order to obtain the “matrix of the void” which should in theory be a 4x4 identity matrix. The measurement was performed in the dark, taking special care to remove all sources of stray light (to give an example, the 7 segments display on a voltage source almost 3 meters away and perpendicularly to the optical axis was enough to add a noticeable signal on the detector). Each waveplate was set at 11 different angular positions over 180°, resulting in a total of 121 measurement points.

Using these measurements, the reconstructed Mueller matrices, first without and then with the corrections for the non-ideal behaviour of the polarising elements, were found to be respectively:

$$\mathbf{M}_{nc} = \begin{bmatrix} 1 & -0.027 & -0.018 & 0.001 \\ 0.012 & 1.019 & 0.012 & -0.009 \\ 0.012 & -0.010 & 0.942 & -0.001 \\ 0 & -0.002 & 0.010 & 1.013 \end{bmatrix}$$

and:

$$\mathbf{M}_{c} = \begin{bmatrix} 1 & -0.005 & -0.018 & 0.001 \\ 0.013 & 0.997 & 0.012 & -0.009 \\ 0.012 & -0.010 & 1.008 & -0.001 \\ 0 & -0.002 & 0.010 & 1.013 \end{bmatrix}$$

where it is seen that the error after correction is lower than 1% on most of the terms.

Owing to the measurement method, the errors should be further reduced by taking more precise and numerous angle positions on the waveplates, a work that would require the automation of the measurement. One important source of error is the angular positioning of the waveplates (a 0.3° error can result in up to 2% of error on the diagonal coefficients [86]), which would be greatly reduced by using automated precision rotation stages. Other sources of errors (such as the non-planar rotation of optical elements, the non-strictly collinear nature of the beam, and many more) exist that we have considered small with regards to the waveplates positioning and retardance, and they would have to be checked to improve accuracy further.

Chapter 9

Experimental validation of the proposed piezo-optic pressure sensor

The full piezo-optic pressure sensor presented and modelized in Chapter 7 has not been realized because of a lack of both time and financial means to have the mold produced. Instead, the principle of the measurement method was validated by testing a pressure sensor in the configuration described in Chapter 6.

9.1 Description of the experimental pressure sensor

The sensor that was realized is a slightly modified version of the one pictured on figure 6.1 (a): the polarizers were directly included on the surface of the dielectric, and a space was left at the bottom of the metal cell to allow thermal dilatation and mitigate the temperature sensitivity as discussed before. This configuration is represented on figure 9.1.

The source and detectors are directly attached to the cell. The photodetector is a BPW34 large-area photodiode, and its photocurrent is amplified and read through a low-noise operational amplifier in transimpedance configuration. The light source is a SuperFlux LPWT-MD00 red (640nm) LED in a clear plastic casing alimented by a simple Zener diode + transistor current source.

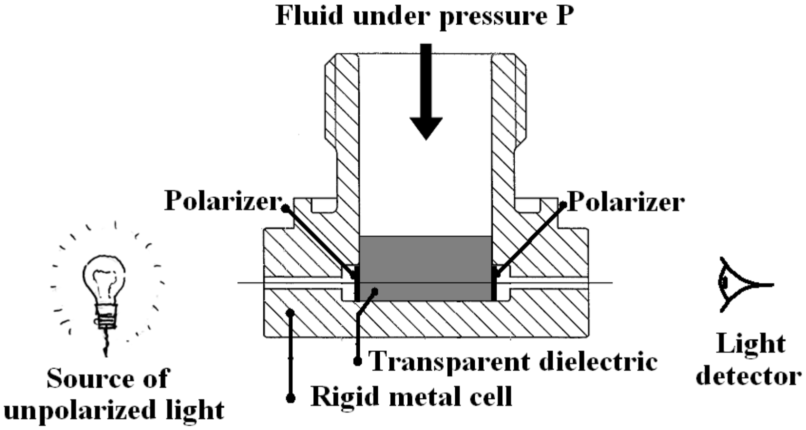

Figure 9.1: Schematic representation of the experimentally realized piezo-optic pressure sensor.

The polarizers were Polaroid plastic polarizers with a typical extinction ratio of 1:500, and two different dielectric materials were tested: a cylinder of clear commercial PMMA and a cylinder made from Sololast "GTS Pro" clear molding resin. In both cases a small flat section was cut on each side of the cylinder, and the polarizers were glued after alignment. Only then were the cylinder forced into the metal cell. The length of the optical path inside the polymer was in both case 1cm. Figure 9.2 illustrates the compactness of the finished sensor.

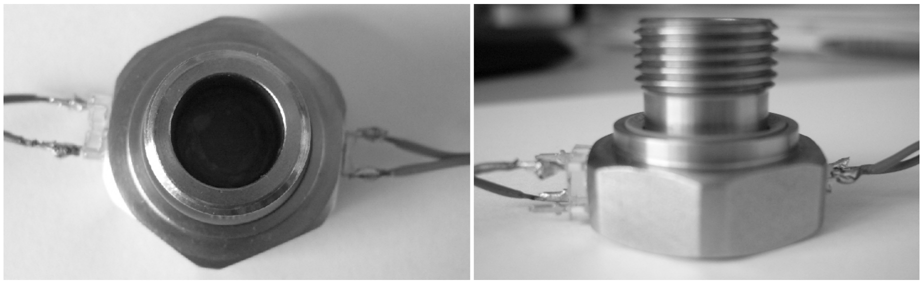

Figure 9.2: One instance of the realized piezo-optic pressure sensor, under two angles. The LED is seen on the right of the sensor and the photodetector on its left. In the picture on the left, the dark inner circle has a diameter of 1 centimeter.

9.2 Measurements

Pressure was applied to the sensor by pressurized oil driven by a pump, with an attached control manometer. The sensor was screwed in a test vessel. The setup is pictured on figure 9.3.

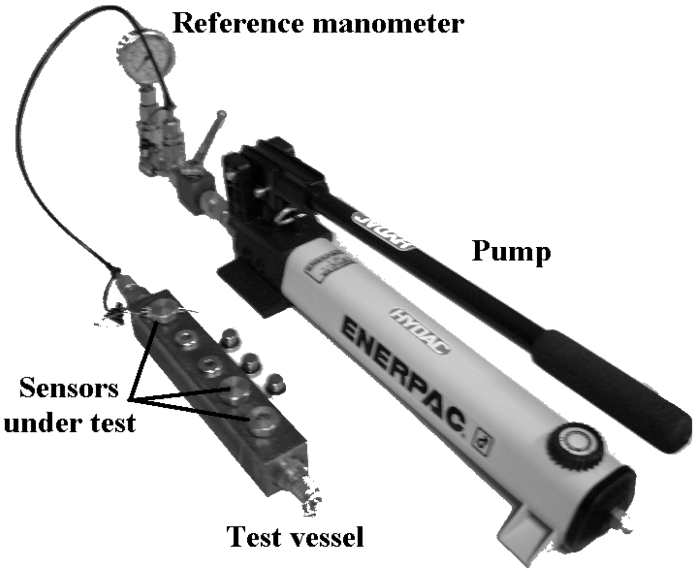

Figure 9.3: Pressure sensors testing setup. Oil under pressure circulates inside the pump and the test vessel.

Figure 9.4 presents sensor output voltages for pressures varying from atmospheric pressure to 60 bars. The pressure was not increased further for fear of leaks, though several series of measurements were carried out at this pressure without any problem. The repeatability of the measurement was to better than 1% of the measured pressure, only limited by the precision of the reference manometer and by the degree of control over the pressure allowed by the manual pump.

The theoretical fit yields a total measurable pressure (corresponding to a maximum phase difference of π) of $P_{max} \approx 74.6\ bars$ using this configuration. This corresponds to a piezo-optic coefficient $C \approx 4.3 \cdot 10^{-12}\ Pa^{-1}$, a value of the typical order of magnitude for hard glassy polymers [81, 53, 102, 70, 80, 54, 57, 55].

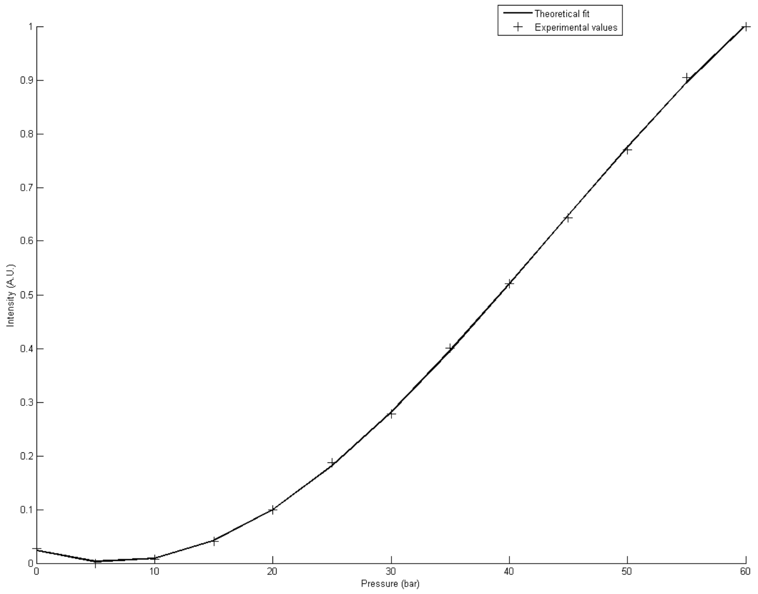

Figure 9.4: Sensor output voltage for relative pressures varying between 0 and 60 bars. Dielectric: polymer inclusion resin “GTS Pro”.

In the same configuration but with PMMA as the dielectric, we obtained $P_{max} \approx 88.6\ bars$ and a piezo-optic coefficient $C \approx 3.6 \cdot 10^{-12}\ Pa^{-1}$, well in the range of typical values found in the litterature [71, 81, 102, 103].

Several series of measurement were performed at different ambient temperatures without an apparent effect on the response of the transducer, in apparent contradiction with the order of magnitude for the temperature dependence of the piezo-optic coefficient we gave in Chapter 7. This could be due to the use of a different type of PMMA compared to the one used in reference [57] from which we extracted the values; the difference in piezo-optic coefficients is an indication that this is the case. Since no systematic study of the temperature dependence was carried out, no definite conclusion can be drawn.

These measurements are not a definite indication of the behavior of the transducer, but they serve to validate the concept of the optical measurement of pressure through the piezo-optic effect.

General Conclusion and Perspectives

The goal of this work was to propose an original method to measure high hydrostatic pressures using a low cost optical sensor.

In Part I of this document we presented the state of the pressure measurement field and stated the problem this work aimed at solving. In Chapters 1 and 2 we presented an overview of the main pressure sensing methods and the principles on which they are based. Chapter 2 focused on optical pressure sensors, most of which are based on the properties of optical fibers. Once the state of the optical pressure measurement field was clear, we discussed in Chapter 3 the advantages and inconveniences of each method with regards to a set of technological imperatives. We finally selected to develop the concept of a sensor based on the piezo-optic effect, i.e. on the measurement of stress-induced birefringence in a transparent dielectric.

In order to modelize a piezo-optic pressure sensor, we presented in Part II the tools that are used in the rest of the document. In chapter 4 we first reviewed the theory of polarization of light, from its physical origin to the more advanced Mueller-Stokes formalism. We then focused, in chapter 5, on the interaction of polarized light with matter: we described the effect of birefringence and presented the theory of the piezo-optic effect. Finally we described the effects on polarized light of total and partial reflections at an interface between two dielectrics. Both the piezo-optic effect and the reflections have been modelized in terms of their Mueller matrices to simplify the modelization of the sensors.

Once the theoretical tools had been presented, we applied them to the modelization of a pressure sensor in part III. Chapter 6 began by the presentation of the concept of a piezo-optic pressure sensor: polarized light interacts with a dielectric material subjected to an external directional force generated by the pressure to measure; the resulting modified state of polarization is then analyzed by a second polarizer and a photodetector. Some aspects of the sensor were optimized, while it's drawbacks and shortcomings were highlighted. In light of this analysis, we proposed a revised concept that addresses the identified issues. The improved proposal uses carefully oriented reflections to replace all polarizing elements, enabling simpler and cheaper production. In Chapter 7 we modelized the proposed sensor using the tools from Part II. The optical behavior of the sensor was described, and then analyzed in terms of sources of error. Geometrical errors were found to be negligible. Temperature effects were also found to be negligible except regarding two aspects: temperature dilatation and the temperature dependence of the piezo-optic coefficient. Two solutions to physically compensate for the thermal dilatation were proposed. Regarding the piezo-optic coefficients, only a careful choice of the dielectric material can ensure that they are not too sensitive to temperature.

Finally in Part IV we presented experimental validations of the concepts developed before. We built, calibrated and tested a Fourier Transform Mueller polarimeter; the different steps of the process were described. We also built a prototype of the piezo-optic pressure sensor using two different dielectric materials, PMMA and a polymer resin. The results were found to be in agreement with the piezo-optic coefficients found in the literature and the concept of the pressure sensor was validated.

To summarize the work presented in this document, we have identified an useful method to measure pressures and have presented in an unified manner the different theoretical tools required in the modelization of the sensor. We have then built upon the initial concept to improve and simplify the sensor. The resulting proposal was modelized and analyzed in terms of measurement errors, and solutions to compensate for these errors were proposed. Finally we have validated the principle of the sensor through the realization and the testing of a prototype device. We have also built a Mueller polarimeter that can be used to carry out extensive campaigns of measurements of the effect of temperature on the piezo-optic effect.

One of the first steps to continue this work would be the realization of a prototype that uses the improved geometry based on polarizing reflections, and a characterization of its behavior.

The next step would be to use the polarimeter to extensively determine the piezo-optic coefficient and its dependence to temperature of several materials. This is a crucial step needed in the realization of a sensor that will not be overly sensitive to temperature.

The proposed geometry could be extended to include a differential measurement of pressure where one path would, for zero pressure, contain right circularly polarized light and the other one left circularly polarized light. A differential measurement of intensity would then yield "zero" for no pressure while still maintaining the sensor in its maximum sensitivity range.

Finally, the range of pressures that can be measured could be greatly increased by using multiple wavelengths in the sensor. Since the stress-induced phase difference is inversely proportional to the wavelength, a shorter wavelength means a smaller maximum measurable pressure but a greater precision. By combining it with a longer wavelength, the "best of both worlds" could be obtained: the long wavelength light would give a coarse measurement of the pressure, enough to remove the ambiguity (due to the periodic nature of the response) on the pressure measured by the shorter wavelength which would in turn yield a more precise measurement. By using more than two wavelength, even greater freedom over the balance between the range and the precision of the measurement could be obtained, with the added benefit that once a dielectric with sympathetic physical characteristics has been found it could be used in a variety of sensors with only a modification of the light sources, and not of the geometry.

Bibliography

[1] P. Meyrueis M. Remouche, A. Chakari. Capteur de température intrinsèque à fibre optique à basse température (-195.8°c à 100°c). In *10ème Congrès International de Métrologie*, 2001.

[2] A. Chakari P. Meyrueis M. Remouche, R. Mokdad. Intrinsic integrated optical temperature sensor based on waveguide bend loss. *Optics and Laser Technology*, 39:1454–1460, 2007.

[3] M. Larashe A. Chakari P. Meyrueis M. Remouche, R. Mokdad. Intrinsic optical fiber temperature sensor operating by modulation of the local numerical aperture. *Optical Engineering*, 46:24401–15, 2007.

[4] M. Remouche. *Modélisation et caractérisation de la propagation de la lumière dans les guides dŽondes courbes et les fibres optiques courbées. Application à un capteur de températures à fibres optiques à modulation dŽamplitude.* PhD thesis, Université Louis Pasteur, 2001.

[5] M. Guilhem P. Pfeiffer S. Lecler A. Chakari A. Lebrun, B. Serio. Polarimetric single-mode fibre optic sensor for low level and low frequency vibration measurements. volume 7726, page 77262A. SPIE, 2010.

[6] N. Javahiraly. *Méthode dŽanalyse optique du module de rigidité. Application à un capteur photonique de position angulaire et de couple à modulation dŽamplitude et de polarisation.* PhD thesis, Université Louis Pasteur, 2002.

[7] S. Dufaut P. Meyrueis A. Chakari, N. Javahiraly. Etude de la biréfringence dŽune fibre optique monomode (tellium). application à un capteur à modulation de la polarisation pour la détection de la vibration de la pression sonore. In *Congrès MTOI*, 2001.

[8] H. Bertold. *Méthode d'exploitation d'un gyroscope à fibre optique pour la navigation autonome d'un véhicule.* PhD thesis, Université Louis Pasteur, 1996.

[9] N-E. Demagh. *Méthodes de métrologie des températures par fibres optiques.* PhD thesis, Université Louis Pasteur, 1986.

[10] M.T. Essemlali. *Metrologie à fibres optiques monomodes et commutateur holographique pour fibres optiques.* PhD thesis, Université Louis Pasteur, 1982.

[11] E. Gaumont. *Minimisation de lŽinfluence dŽune large fluctuation de température sur la polarisation dans une fibre optique monomode. Application : capteur polarimétrique à fibre optique pour la mesure dŽune position angulaire entre les températures* $T = 20^\circ K$ *et* $T = 450K$*.* PhD thesis, Université Louis Pasteur, 2000.

[12] W.E.K. Middleton. *The history of the barometer.* 1964.

[13] De Waard. *L'expérience barométrique.* Thouars, 1936.

[14] A. Beaulieu F. de Gandt. *Lóeuvre de Torricelli: science galiléenne et nouvelle géométrie.* 1989.

[15] A. Avogadro. Essai d'une maniere de determiner les masses relatives des molecules elementaires des corps, et les proportions selon lesquelles elles entrent dans ces combinaisons. *Journal de Physique*, 73:58–76, 1810.

[16] E. Jones. *Instrument Technology.* Butterworths, London, 1985.

[17] Z. Henry. *Instrumentation and Measurement for Environmental Sciences.* American society of agricultural engineers, St. Joseph, 1991.

[18] C. Huygens. Extrait d'une autre lettre de m. hugens touchant une nouvelle maniere de barometre, qu'il a inventée. *Le journal des sçavans*, 3:138–145, 1672.

[19] W. Boyes. *Instrumentation Reference Book, Fourth Edition.* Butterworth-Heinemann, Oxford, 2009.

[20] A.L. Window. *Strain Gauge Technology.* Springer, Berlin, 1992.

[21] G.B. Hocker. Fiber-optic sensing of pressure and temperature. *Applied Optics*, 19:1445–1448, 1979.

[22] M.E. Welland H.P. Hodson M. Jusheng W. Gualong, F. Yiton. Study on a novel optical pressure sensor. *ICEPT*, pages 195–200, 2003.

[23] A. Farhad Z. Yang. Intrinsic single-mode fiber-optic pressure sensor. *IEEE Photonics technology letters*, 13(11):1212–1214, novembre 2001.

[24] M. Abushagur H. Zhijian, A. Bouzid. Fiber optic pressure sensors. *IEEE*, pages 368–370, 1992.

[25] A. Wang Y. Zhu. Miniature fiber-optic pressure sensor. *IEEE Photonics technology letters*, 17:447–449, février 2005.

[26] J. Wojcik M. Beaulieu W.J. Bock, W. Urbanczyk. White-light interferometric fiber-optic pressure sensor. *IEEE transactions on instrumentation and measurements*, 44(3):694–697, juin 1995.

[27] S. Sekine T. Sato M. Ohkawa, T. Abe. Integrated optic micropressure sensor using ring resonator. *Electronics and Communications in Japan*, Vol. 79, No. 4:1–9, 1996.

[28] X. Fang X. Jin J. Lin A. Wang, S. He. Optical fiber pressure sensor based on photoelasticity and its application. *Journal of lightwave technology*, 10(10):1466–1472, octobre 1992.

[29] W.J. Bock. High-pressure polarimetric sensor using birefringent optical fibers. *IEEE*, pages 414–417, 1989.

[30] Y. Wang J. Lin C. Sun, L. Wang. Design of high-sensivity photoelastic optical fiber pressure sensor: A differentialapproach. *IEEE photonics technology letters*, 19(7):976–978, juillet 1997.

[31] W.J. Bock J. Chen. A novel fiber-optic pressure sensor operated at 1300-nm wavelength. *IEEE transactions on instrumentation and measurement*, 53(1):10–14, février 2004.

[32] J.W. Berthold. Historical review of microbend fiber-optic sensors. *Journal of Lightwave Technology*, 13-7:1193–1199, 1995.

[33] C. Lu L. Su, K.S. Chiang. Fiber bragg-grating incorporated microbend sensor for simultaneous mechanical parameter and temperature measurement. *Photonics Technology Letters, IEEE*, 17(12):2697 – 2699, dec. 2005.

[34] B. Culshaw D. Donlagic. Microbend sensor structure for use in distributed and quasi-distributed sensor systems based on selective launching and filtering of the modes in graded index multimode fiber. *Lightwave Technology, Journal of*, 17(10):1856 –1868, oct 1999.

[35] C. Lu L. Su, K.S. Chiang. Microbend-induced mode coupling in a graded-index multimode fiber. *Appl. Opt.*, 44(34):7394–7402, 2005.

[36] L. Thévenaz. Review and progress on distributed fibre sensing. *Optical Fiber Sensors*, page ThC1, 2006.

[37] H. Aben. *Photoelasticity of Glass.* Springer-Verlag, Berlin, 1993.

[38] E. Coker. *Treatise on Photoelasticity.* Cambridge University Press, Cambridge, 1957.

[39] M.M. Frocht. *Photoelasticity*, volume vol. 1. John Wiley & Sons, 1941.

[40] M.M. Frocht. *Photoelasticity*, volume vol. 2. John Wiley & Sons, 1941.

[41] M. Hetenyi. The fundamentals of three dimensional photoelasticity. *Journal of Applied Mechanics*, vol. 5:149–155, 1938.

[42] F. Jessop. *Photoelasticity. Principles & Methods.* Dover, Mineola, 1949.

[43] J.C. Kemp. Piezo-optical birefringence modulators: New use for a long-known effect. *JOURNAL OF THE OPTICAL SOCIETY OF AMERICA*, 59-8:950, 1969.

[44] J.H. Kong. *Electromagnetic Wave Theory.* EMW Publishing, Cambridge, 2005.

[45] M. Born. *Principles of Optics.* Cambridge University Press, Cambridge, 1999.

[46] E. Collett. *Polarized Light in Fiber Optics.* PolaWave Group, Lincroft, 2003.

[47] G. Ghosh. Dispersion-equation coefficients for the refractive index and birefringence of calcite and quartz crystals. *Optics Communications*, 163(1-3):95–102, 1999.

[48] S. Timoshenko. *Theory of Elasticity.* McGraw-Hill, New York, 1970.

[49] T. Narasimhamurty. *Photoelastic and Electro-Optic Properties of Crystals.* Plenum Press, New York, 1981.

[50] E. Collett. Mueller-stokes matrix formulation of fresnel's equations. *American Journal of Physics*, 39(5):517–528, 1971.

[51] L.D. Landau. *Course of Theoretical Physics (Volume 7): Theory of Elasticity.* Butterworth-Heinemann, Oxford, 1986.

[52] H. Yao. *Light-Emitting Diodes.* SPIE, Bellingham, 2001.

[53] S. Baumer. *Handbook of Plastic Optics.* Wiley-VCH Verlag GmbH, 2010.

[54] H. Mark. *Encyclopedia of Polymer Science and Technology, 12 Volume Set.* Wiley-Interscience, New York, 2004.

[55] G. Statkiewicz-Barabach W. Urbanczyk L. Khan D.J. Webb M. K. Szczurowski, T. Martynkien. Measurements of stress-optic coefficient in polymer optical fibers. *Opt. Lett.*, 35(12):2013–2015, 2010.

[56] A. Feldman R.M. Waxler, D. Horowitz. Optical and physical parameters of plexiglas 55 and lexan. *Appl. Opt.*, 18(1):101–104, 1979.

[57] C. Sanchez F. Meseguer. Piezobirefringence of pmma: Optical and mechanical relaxations and influence of temperature. *Journal of Materials Science*, 15:53–60, 1980.

[58] T.D. Callinan A.V. Tobolsky. Properties and structure of polymers. *Journal of The Electrochemical Society*, 107(10):243C–243C, 1960.

[59] E. Baer. *Engineering Design for Plastics.* R.E. Krieger Pub. Co, Malabar, 1964.

[60] E.H. Land. Some aspects of the development of sheet polarizers. *J. Opt. Soc. Am.*, 41(12):957–962, 1951.

[61] S.P. Talim R.J. King. Some aspects of polarizer performance. *Journal of Physics E: Scientific Instruments*, 4(2):93, 1971.

[62] R.A. Chipman S.-Y. Lu. Interpretation of mueller matrices based on polar decomposition. *J. Opt. Soc. Am. A*, 13(5):1106–1113, 1996.

[63] R. Ossikovski. Analysis of depolarizing mueller matrices through a symmetric decomposition. *J. Opt. Soc. Am. A*, 26(5):1109–1118, 2009.

[64] L. Prodh́omme. *Phys. Chem. Glasses*, 4:119, 1960.

[65] J. M. Cariou-L. Martin P. Michel, J. Dugas. Thermal variations of refractive index of pmma, polystyrene, and poly (4-methyl-1 -pentene). *Journal of Macromolecular Science, Part B: Physics*, 25-4:379–394, 1986.

[66] L. Martin P. Michel J.M. Cariou, J. Dugas. Refractive-index variations with temperature of pmma and polycarbonate. *Appl. Opt.*, 25(3):334–336, 1986.

[67] R.F. Boyer R. Simha. On a general relation involving the glass temperature and coefficients of expansion of polymers. *The Journal of Chemical Physics*, 37(5):1003–1007, 1962.

[68] O. Grümm W. Kuhm. *Kolloid Z.*, 101:248, 1942.

[69] L.R.G. Treolor. *The physics of Rubber Elasticity*. 1958.

[70] J. Bicerano. *Prediction of Polymer Properties*. Marcel Dekker, New York, 2002.

[71] D. Payne A. Barlow. The stress-optic effect in optical fibers. *Quantum Electronics, IEEE Journal of*, 19(5):834 – 839, may 1983.

[72] J. Jun H. Kim. Fiber optic voltage sensor based on the photoelastic effect in a single-mode optical fiber. *Optical Engineering*, 39(12):3281–3284, 2000.

[73] N. Sinha J. Pindera. On the studies of residual stresses in glass plates. *Experimental Mechanics*, 11:113–120, 1971. 10.1007/BF02328645.

[74] G. Rehage H.J. Kock. Photoelasticity and structure of pmma networks. *Colloid & Polymer Science*, 262:182–188, 1984. 10.1007/BF01458959.

[75] A. Peterlin. Mechanical properties of polymeric solids. *Annual Review of Materials Science*, 2(1):349–380, 1972.

[76] J.A. Jukes P.B. Bowden. The plastic flow of isotropic polymers. *Journal of Materials Science*, 7:52–63, 1972. 10.1007/BF00549550.

[77] A. Pegoretti S. Pandini. Time, temperature, and strain effects on viscoelastic poisson ratio of epoxy resins. *Polymer Engineering and Science*, 48:1434–1441, 2008.

[78] N. Cheremisinoff. *Polymer Mixing and Extrusion Technology.* M. Dekker, New York, 1987.

[79] K.L. Reifsnider C.A. Mahieux. Property modeling across transition temperatures in polymers: a robust stiffness-temperature model. *Polymer*, 42(7):3281 – 3291, 2001.

[80] D. Krevelen. *Properties of Polymers.* Elsevier, Amsterdam, 2003.

[81] M. Bass. *Handbook of Optics, Third Edition Volume I: Geometrical and Physical Optics, Polarized Light, Components and Instruments.* McGraw-Hill Professional, City, 2009.

[82] M.H. Smith. Optimization of a dual-rotating-retarder mueller matrix polarimeter. *Appl. Opt.*, 41(13):2488–2493, 2002.

[83] D.H. Goldstein. Mueller matrix dual-rotating retarder polarimeter. *Appl. Opt.*, 31(31):6676–6683, 1992.

[84] R.M.A. Azzam. Photopolarimetric measurement of the mueller matrix by fourier analysis of a single detected signal. *Opt. Lett.*, 2(6):148–150, 1978.

[85] L. Johann L. Broch, A.E. Naciri. Systematic errors for a mueller matrix dual rotating compensator ellipsometer. *Opt. Express*, 16(12):8814–8824, 2008.

[86] R.A. Chipman D.H. Goldstein. Error analysis of a mueller matrix polarimeter. *J. Opt. Soc. Am. A*, 7(4):693–700, 1990.

[87] P.S. Hauge. Mueller matrix ellipsometry with imperfect compensators. *J. Opt. Soc. Am.*, 68(11):1519–1528, 1978.

[88] S.-M.F. Nee. Error analysis for mueller matrix measurement. *J. Opt. Soc. Am. A*, 20(8):1651–1657, 2003.

[89] P. Brokaw. An i.c. amplifier userś guide to decoupling, grounding, and making things go right for a change. analog devices application note an-202.

[90] A. Rich. Shielding ang guarding: How to exclude interference-type noise - what to do and why to do it - a rational approach. Analog Device Application Note AN-347.

[91] R. Morrison. *Grounding and Shielding Techniques.* Wiley, New York, 1998.

[92] H.B. Perkins B.R. Grunstra. A method for the measurement of optical retardation angles near 90 degrees. *Appl. Opt.*, 5(4):585–587, 1966.

[93] D.L. Feucht D.A. Holmes. Formulas for using wave plates in ellipsometry. *J. Opt. Soc. Am.*, 57(4):466–471, 1967.

[94] H.G. Jerrard. The calibration of quarter-wave plates. *J. Opt. Soc. Am.*, 42(3):159–165, 1952.

[95] R.C. Plumb. Analysis of elliptically polarized light. *J. Opt. Soc. Am.*, 50(9):892, 1960.

[96] D.-C. Su L.-H. Shyu, C.-L. Chen. Method for measuring the retardation of a wave plate. *Appl. Opt.*, 32(22):4228–4230, 1993.

[97] W. Runwen L. Yao, Z. Zhiyao. Optical heterodyne measurement of the phase retardation of a quarter-wave plate. *Opt. Lett.*, 13(7):553–555, 1988.

[98] H.G. Jerrard. Optical compensators for measurement of elliptical polarization. *J. Opt. Soc. Am.*, 38(1):35–57, 1948.

[99] J. Strong. *Procedures in Experimental Physics.* Lindsay Pubns, City, 1986.

[100] C.-C. Hsu D.-C. Su. Method for determining the optical axis and (ne, no) of a birefringent crystal. *Appl. Opt.*, 41(19):3936–3940, 2002.

[101] D.-C. Su M.-H. Chiu, C.-D. Chen. Method for determining the fast axis and phase retardation of a wave plate. *J. Opt. Soc. Am. A*, 13(9):1924–1929, 1996.

[102] M. Weber. *Handbook of Optical Materials.* CRC Press, Boca Raton, 2003.

[103] R. Dändliker A. Bertholds. High-resolution photoelastic pressure sensor using low-birefringence fiber. *Appl. Opt.*, 25(3):340–343, 1986.

[104] J. Lin C. Sun, X. Yu. Two practical methods for improving the long-term stabiblity of the photoelasticoptical fiber pressure sensor. *IEEE transactions on instrumentation and measurement*, 49(4):776–778, août 2000.

[105] B.-S. Bae E.-S. Kang, T.-H. Lee. Measurement of the thermo-optic coefficients in sol-gel derived inorganic–organic hybrid material films. *Applied Physics Letters*, 81(8):1438–1440, 2002.

[106] S. Haussühl. *Physical Properties of Crystals: an Introduction.* Wiley-VCH, Weinheim, 2007.

[107] K.S. Vecchio F.C. Jiang A. Makradi J. Richeton, S. Ahzi. Modeling and validation of the large deformation inelastic response of amorphous polymers over a wide range of temperatures and strain rates. *International Journal of Solids and Structures*, 44(24):7938 – 7954, 2007.

Résumé long

Introduction

Les capteurs optiques connaissent depuis plusieurs années un succès croissant en milieu industriel et ce principalement depuis l'apparition commerciale de micro composants optique et électronique, et notamment de sources de lumières compactes, bon marché et fiables : les diodes électroluminescentes ou LED (Light Emitting Diode), les diodes laser et plus récemment les VCSELs.

Les technologies de l'optique sont exploitées dans plusieurs domaines industriels tels que le transfert de données (de la simple télécommande infrarouge jusqu'aux fibres optiques qui sont notamment à la base fonctionnelle de l'internet moderne) ou encore le stockage informatique (sur CDROM, DVDROM et maintenant Blu-Ray) ainsi que dans des systèmes de métrologie comme les mesures de distance. Mais ces technologies sont nettement moins présentes dans les systèmes de mesure à faible coût et à grande production (la seule exception notable étant peut-être les barrières de franchissement infrarouges et les souris optiques). En effet les systèmes de mesures électroniques, principalement des capteurs basés sur des techniques connues, éprouvées et utilisées depuis de nombreuses années remplissent ces fonctions. De ce fait les composants électroniques sont bon marché, les techniques de production (essentiellement d'assemblage) sont maitrisées, et les couts en recherche , développement et production sont très faibles.

Par opposition, les systèmes de mesures optiques sont relativement récents et il en résulte des composants plus chers et un temps de R&D plus important pour les dispositifs les incorporant. On peut aussi noter que ces produits sont en général plus délicats à gérer au niveau de la production de masse, et que leurs performances brutes sont souvent comparables à celles de leurs équivalents électroniques bien qu'ayant de grandes marges de progression. Elles cumulent par contre les avantages inhérents à l'optique photonique, à savoir principalement une insensibilité naturelle aux champs électriques et magnétiques intense ainsi qu'une précision atteignable, avec la recherche nécessaire pour celà, plus importante. Pour toutes ces raisons, même si la transition vers des mesures optiques dans les dispositifs produit en masse n'en est qu'à son début il est important pour une entreprise concevant des produits de mesure innovants d'acquérir des connaissances et un savoir-faire dans ce domaine qui sera sans aucun doute amené à prendre une place de plus en plus importante dans les branches de l'industrie concernée au cours les années à venir.

C'est dans ce contexte que la société Hydac, spécialiste international de la technique des fluides (mesure et contrôle), cherche à étudier la faisabilité technique et commerciale de la mesure de pressions hydrauliques utilisant des méthodes optiques. Dans ce but, elle s'est associée dans le cadre d'une convention CIFRE au Laboratoire des Système Photoniques qui possède un long savoir-faire dans le domaine des capteurs optiques, notamment pour ce qui est des capteurs à base de guide de lumière (principalement fibres optiques) dont les propriétés sont utilisées pour mesurer pression, température, champs électriques et magnétique, mais aussi vibrations sonores ou sismiques. Le LSP s'applique notamment dans ses collaborations avec ses partenaires industriels à répondre aux préjugés usuels qui veulent que les dispositifs optiques photoniques de mesure et de contrôle soient plus fragiles, plus chères et délicats à utiliser, et qu'ils soient finalement confinée aux laboratoires de recherche ou à de rares équipements à prix élevés (par exemple dans le domaine spatial). C'est en s'appuyant sur cette base de connaissances et ce savoir-faire que ce travail a été mené avec succès.

1 État de l'art

Dans cette partie du travail nous présentons un état de l'art et du marché commercial des capteurs de pression, puis nous nous intéressons aux capteurs optiques présents dans la littérature scientifique afin de situer notre étude dans son environnement industriel et scientifique. Nous présentons ensuite le cahier des charges imposé par la société HYDAC pour conclure que les technologies actuellement sur le marché ne sont pas satisfaisantes par rapport aux contraintes imposées. Suite à ce constat nous proposons un nouveau concept de transducteur piezo-optique adapté aux performances du cahier des charges et notamment à une production de masse.

Le choix du principe du capteur à utiliser dépend fortement de : la précision recherchée, des gammes et plages de pression, de l'hostilité de l'environnement et de bien d'autres facteurs, mais quelques tendances se retrouvent dans la majorité des technologies.

1.1 Principaux capteurs de pression hydraulique du commerce

La principale grandeur généralement mesurée par les capteurs de pression hydraulique est la force appliquée sur une surface calibrée par la pression à mesurer. Les méthodes courantes pour ce faire sont :

- les effets purement mécaniques : équilibres de liquides (baromètres à liquide comme le mercure par exemple), déflexion d'une aiguille par une membrane soumise à la pression (manomètre à aiguille), déformation d'un "tube" (tube de bourdon), etc,
- l'effet piezo-résistif : le transducteur est une fine membrane soumise à la pression. La déformation due à la force appliquée modifie sa résistance électrique qui est mesurée en général par un pont de Wheatstone. On utilise couramment de fines couches de silicium ou de divers métaux déposés en membranes d'épaisseur strictement controllée,
- l'effet piezo-électrique : les matériaux piezo-électriques, comme le quartz, génèrent une tension électrique quand ils sont soumis à une force,
- divers effets électriques comme une variation de capacitance ou d'inductance par déformation mécanique.
- Les méthodes optiques, détaillées ci-dessous

Il existe d'autres méthodes moins courantes pour des applications très spécifiques; elle sont de peu d'intérêt pour notre étude.

1.2 Le cas des capteurs optiques de pression hydraulique

Les capteurs optiques de pression se divisent en deux grandes catégories : capteurs extrinsèques où l'optique n'est pas au cœur du transducteur mais sert uniquement à mesurer l'évolution du transducteur lui même (par exemple pour mesurer le déplacement d'une membrane par interférométrie), et les capteurs intrinsèques où l'effet à mesurer est directement optique; c'est ce dernier cas qui nous intéresse. Tous les capteurs optiques existant de ce type sont des capteurs intrinsèques à fibre optique :

- Les capteurs à modulation d'amplitude : La grandeur physique à mesurer module directement l'intensité de la lumière traversant la fibre. C'est une méthode très simple à mettre en œuvre, car elle ne nécessite pas de matériel sophistiqué. La principale technique consiste à utiliser des microcourbures sur la fibre, courbures qui sont modifiées par une pression externe. Cette technologie n'existe pratiquement pas dans le commerce car elle nécessite des réglages et des précautions gérables facilement pour le moment uniquement en laboratoire.

- Les capteurs à modulation de phase : C'est le type de capteur intrinsèque à fibres optiques le plus précis. Ici l'effet physique à mesurer module par action sur le matériau de la fibre optique la phase de l'onde lumineuse se propageant dans cette fibre. Si l'on prend le cas de la pressions, une pression hydrostatique va comprimer la fibre et donc faire varier l'indice du cœur de cette fibre. Par conséquent, la propagation de l'onde lumineuse sera altérée. C'est le cas notamment de tous les capteurs interférométriques du type Mach-Zender.
- Les capteurs à modulation de longueur d'onde : la pression va influer sur le spectre de longueurs d'ondes qui peuvent se propager dans la fibre. C'est le cas des fibres à réseau de bragg par exemple, mais cette technique nécessite un outil d'analyse en longueur d'onde en général couteux et délicat à exploiter (sauf dans des cas simples) en sortie de fibre.
- Capteurs polarimétriques : l'état de polarisation de la lumière dans une fibre dépend de la biréfringence de celle-ci, qui peut être modifiée par un effort externe. C'est cette variation d'état de polarisation qui est détecté, principalement en utilisant des fibres à maintien de polarisation ou des fibres monomodes correctement caractérisées.

1.3 Cahier des charges du capteur de pression hydraustatique

Le cadre dans lequel doit rentrer le capteur étudié tel que spécifié par HYDAC est le suivant :

- être un capteur intrinsèque et donc simple
- être utilisable dans une gamme allant de 1 bar à 100 bars pour une mesure hydrostatique (relativement à la pression atmosphérique)
- disposer d'une précision sur la mesure de 1% de la plage de mesure
- rentrer dans la gamme de prix en matériaux bruts et main d'œuvre de la gamme actuelle de capteurs de pression Hydac sans demander de modification significative des moyens de production de cette société habituée à l'exploitation de procédés propres à l'industrie microélectronique.

Le point le plus critique que nous avons identifié à été le quatrième : toutes les technologies de capteur à base de fibre optique demandent des moyens de production particuliers (soudeuse à fibres, "graveur" de réseau de bragg, etc), une expertise qui est absente dans l'entreprise de la part de la main d'œuvre, et les composants à considérer peuvent être hors de la gamme de prix visée (spectromètres …).

Notre choix s'est donc porté sur une méthode polarimétrique n'utilisant pas de fibre optique mais un guide de lumière adapté qui deviendra biréfringent si il est soumis à une pression hydraulique. Le principal avantage de notre proposition est qu'un tel composant peut être directement moulé en matière plastique pour un coût très faible, en grandes quantités et qu'il pourra être facilement intégré au dispositif utilisant les procédés de la microélectronique. Le fonctionnement spécifique du capteur est présenté dans les sections qui suivent.

2 Etude théorique

Dans cette seconde partie du travail, il s'est tout d'abord agit d'analyser les outils théoriques existants pour traiter de la polarisation de la lumière ainsi que des effets d'une déformation physique sur les propriétés optiques des matériaux. Une fois les bases établies nous avons élaboré sur la base de ces concepts une première approche de la modélisation permettant de proposer une version conceptuelle du capteur piezo-optique que nous présentons.

Une fois les bases théoriques posées nous présentons le concept global du capteur ainsi que les contraintes de conception, de fabrication et d'exploitation qui nous guident. Nous optimisons le design du capteur que nous proposons en réponse à ces contraintes et nous présentons une version finale du capteur de pression. L'étape suivante est la modélisation théorique du comportement du capteur en utilisant les outils présentés précédemment couplés à une analyse par éléments finis des déformations mécaniques.

2.1 Polarisation de la lumière

La première partie de notre étude théorique présente le cadre classique de la théorie de la polarisation : nous étudions l'évolution dans un plan fixe de l'évolution temporelle du vecteur champ électrique d'une onde monochromatique plane. Les trois représentations classiques de la polarisation et les méthodes de calculs qui leur sont associées sont traitées pour être exploitables dans le cadre de nos objectifs :

- L'ellipse de polarisation, ellipse dessinée par le vecteur champ électrique. On distingue les cas dégénérés classiques : les polarisation circulaire droite et gauche, linéaires verticales horizontales et à plus ou moins 45°
- La représentation de Jones en vecteur 2x1 complexe et le formalisme des matrices de Jones qui lui est associé
- Les vecteurs de Stokes 4x1 qui permettent de représenter une lumière partiellement polarisée, et les matrices de transformation linéaires qui leurs sont associées : les matrices de Mueller

Sont également présentés les composants optiques classiques de l'étude de la polarisation, à savoir les lames à retard, les rotateurs et les diatténuateurs.

Enfin nous introduisons la « sphère de Poincaré » qui permet de représenter graphiquement l'action d'un élément optique polarisant soit sur une polarisation d'entrée donnée, en traçant un parcours sur la sphère, soit d'une polarisation quelconque en présentant la déformation de la sphère.

2.2 Présentation de l'effet piezo-optique et de son exploitation dans le capteur proposé

Dans cette section nous considérons le modèle simple de Hook pour les petites déformations élastiques des matériaux. Nous relions ensuite ces déformations à la variation d'indice qu'elles provoquent dans un matériau transparent (et donc leur effet créateur de biréfringence) au travers des coefficients piezo-optiques de Pockels et plus simplement du "coefficient elasto-optique" d'un matériau. Nous étudions également l'effet de la température sur la biréfringence induite par pression.

Nous présentons ensuite le cas particulier, qui est utilisé dans le dispositif proposé, de l'évolution polarimétrique d'une lumière réfléchie à une interface notamment en terme d'effets de la pression et de la température.

Finalement le comportement simple d'un système constitué en série d'une source de lumière, d'un polariseur, d'un cube transparent soumis à une force, d'un second polariseur et enfin d'un photodétecteur est étudié en guise de validation de l'étude conceptuelle présentée dans le chapitre.

2.3 Architecture du capteur piezo-optique de pression hydaulique que nous proposons

Cette architecture repose sur l'étude théorique précédente et est adaptée pour une mesure de pression hydrostatique mais présente quelques inconvénients que nous sommes amenés à gérer.

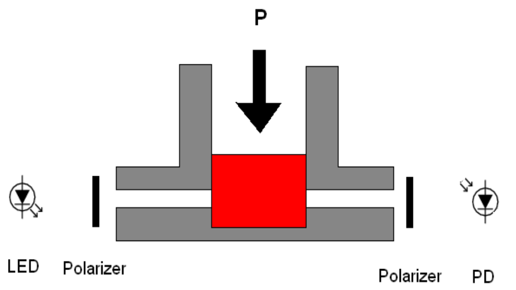

Dessin 2: Principe de base

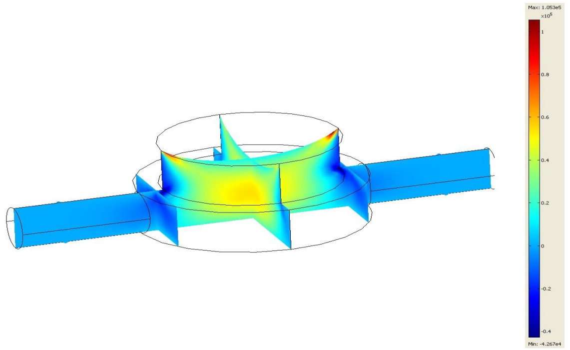

Dessin 1: Exemple de déformation mécanique due à la pression

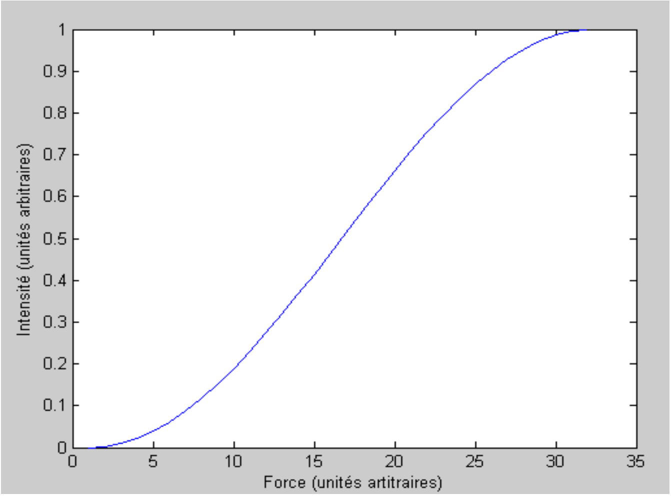

Dessin 3: Réponse à une force appliquée

Cette architecture est particulièrement sensible à la température et sa précision est fortement limitée par la qualité des polariseurs qui ne peuvent, pour l'application envisagée, qu'être de piètre qualité. Cette configuration est loin d'être idéale comme illustré par sa réponse à la pression ci-dessous; elle doit donc être améliorée.

La réponse basique est sinusoïdale et à pression "nulle" (atmosphérique) nous nous trouvons proche du zero. Dans le cas d'un capteur bas coût la réponse doit être le plus linéaire possible pour éviter d'avoir à intégrer une électronique de correction trop complexe ce qui n'est le cas ici que pour une très faible étendue de variation de la pression; mais dans ce cas la dynamique du capteur est extrêmement faible, comme le montre l'écrasement de la courbe autour de zéro.

Le point de mesure idéal se situe bien entendu en milieu de courbe : la réponse est quasi-linaire sur une grande plage ,et la dynamique y est maximale. Cela correspond à un état de polarisation circulaire que nous allons donc chercher à obtenir dans un processus d'optimisation.

Nous proposons donc la solution optimisée représentée par l'architecture de la figure 4 :

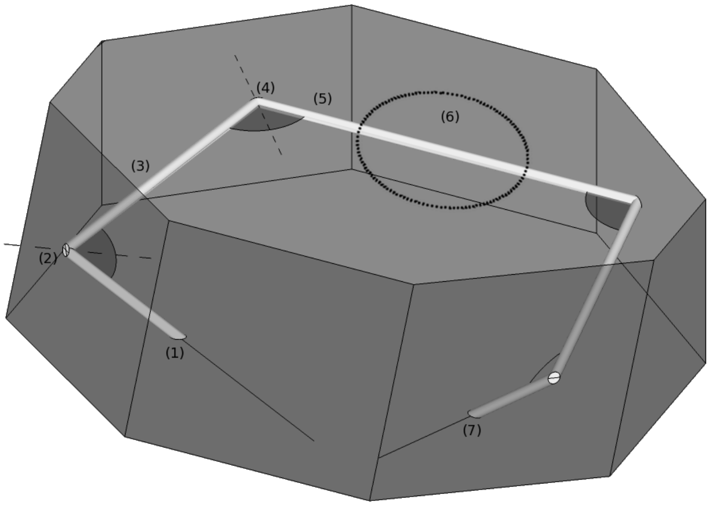

Dessin 4: Design optimisé

Le fonctionnement du transducteur opérant selon ce schéma de concept est le suivant :

- une lumière non polarisée arrive à une interface à l'angle de brewster et ressort très fortement polarisée (bien au delà de la qualité que peut fournir un polariseur à bas coût). Le principe est exposé sur le dessin 5
- le faisceau subit une réflexion totale interne qui oriente son axe de polarisation pour pour maximum de sensibilité à la pression, cf dessins 6 et 7
- il traverse la cellule rendue biréfringente par effet de la pression
- une réflexion transforme ensuite la polarisation de manière à ce que si la cellule n'est pas biréfringente l'on obtienne une polarisation circulaire
- une dernière réflexion à l'angle de brewster se comporte comme un second polariseur de haute qualité malgré un cout très faible

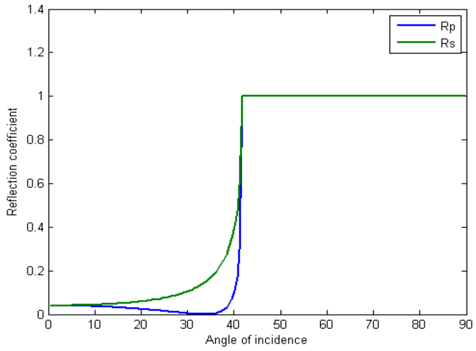

Dessin 6: Angle de Brewster

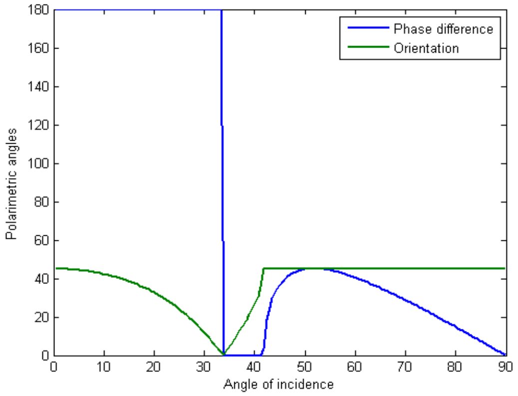

Dessin 5: Évolution des paramètres elliptiques après réflexion

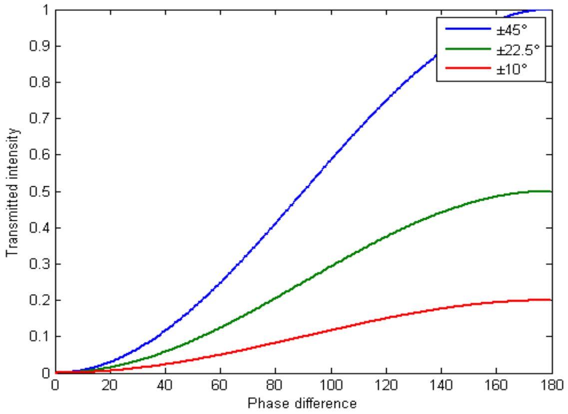

Dessin 7: Sensibilité à l'orientation de la polarisation

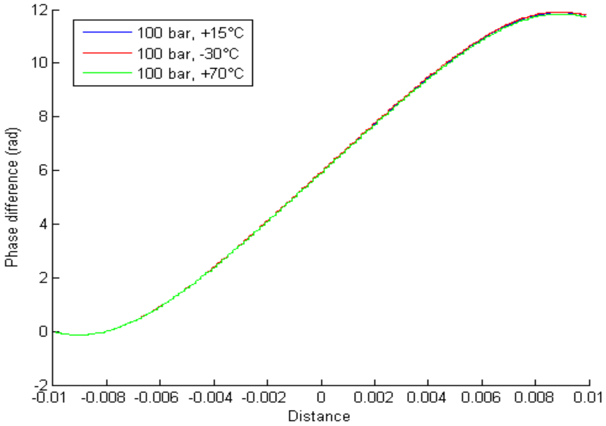

Dessin 8: Effet de la température sur le déphasage pour une pression donnée

Ce design règle les problèmes de coût (car il est en polymère injecté), de qualité des polariseurs ainsi que de dynamique du capteur. De plus il assure une bonne linéarité autour de zéro. Il a également l'avantage de ne comporter que peu d'éléments puisque l'on supprime les polariseurs et par là même l'erreur de positionnement de leurs axes. Il s'agit d'un système monolithique qui peut donc être moulé par injection en grande quantité et à coût très faible. Enfin, une simulation tenant compte de tous les paramètres montre qu'une auto-compensation physique due à la symétrie du système minimise la dépendance à la température puisqu'une variation de plus de 100°C correspond à environ 0,2% d'écart au maximum à la courbe de réponse à température ambiante ce qui élimine la nécessité d'une correction thermique.

Un calcul de tolérancement et de propagation d'erreur montre que l'on peut obtenir une précision de 0,5% - 1% de la valeur mesurée pour une erreur sur les angles (et donc sur le moule) de 1% ce qui est tout à fait compatible avec les technologies d'injection de polymères en production.

3 Validation expérimentale

Après l'étude théorique du système proposé, il s'agit de comparer les résultats de calculs et de simulation au comportement réel des matériaux.

Une grande partie de notre travail doctoral expérimental a consisté en la conception, la réalisation puis la caractérisation d'un instrument de mesure polarimétrique : le polarimètre de Mueller. Ce polarimètre peut ensuite être utilisé pour caractériser la réponse polarimétrique de différents matériaux transparents soumis à des pressions et températures différentes et valider les différents éléments du capteur final tel que proposé ci-dessus.

3.1 Polarimètre de Mueller

Un polarimètre de Mueller a été conçu et réalisé. Il a été réalisé selon le modèle : source – polariseur – lame quart d'onde – espace échantillon – lame quart d'onde – polariseur – détecteur. Afin de minimiser les effets polarimétriques des ouvertures diaphragmantes se situant le long du chemin optique, le détecteur est constitué d'une lentille d'ouverture très faible, et donc de grande profondeur de champs, qui image une zone au centre de l'espace échantillon sur une photodiode.

Ce polarimètre est utilisé en mode transformée de Fourier : après avoir choisi un pas, pour chaque angle de la lame quart-d'onde d'entrée l'intensité de sortie est mesurée pour n positions de la quart d'onde de sortie, et de même pour chaque angle d'entrée possible. La table de mesure résultante subit une transformée de Fourier 2D et les coefficients résultants permettent de déterminer les différents coefficients de la matrice de Mueller de l'échantillon.

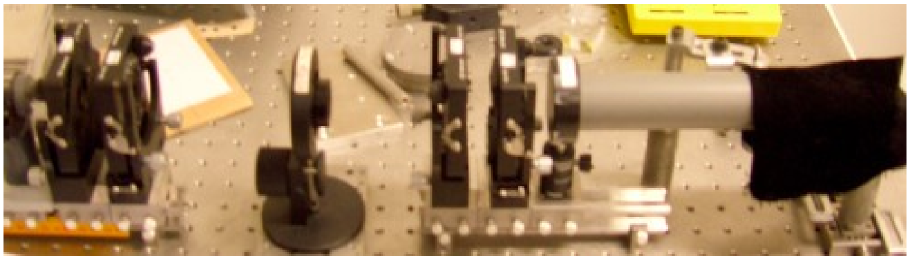

Dessin 9: Polarimètre de Mueller

Différents éléments extérieurs au capteur que nous proposons ont été caractérisés, dont principalement la linéarité du détecteur, son seuil de bruit, le taux d'extinction des polariseurs et les retards effectifs des deux lames quart d'onde. Le détecteur utilisé présente une large plage de linéarité, les polariseurs ont un taux d'extinction d'environ 1:7000 et les lames à retard présentent des retards respectifs de $\pi/2-\pi/72{,}5$ et $\pi/2-\pi/1987$; ces valeurs ont été intégrées dans l'algorithme de reconstruction de la matrice de Mueller.

Au final la polarimètre permet d'obtenir des mesures d'une précision approchant les 2% d'erreur maximale sur les coefficients de Mueller. Les différentes étapes de calibration et deux mesures d'échantillons sont présentées sur les images ci-dessous.

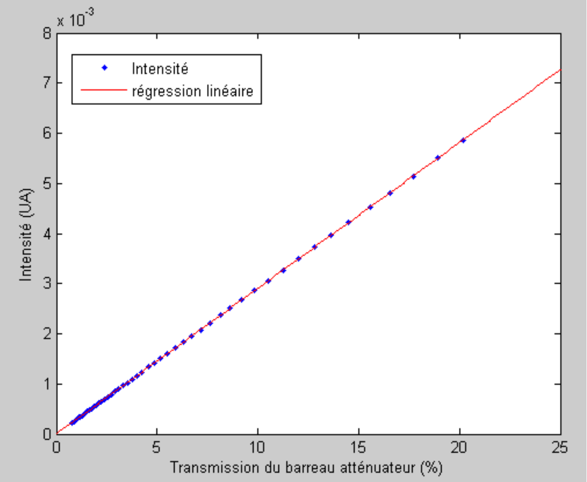

Dessin 11: Caractérisation de la linéarité de la photodiode

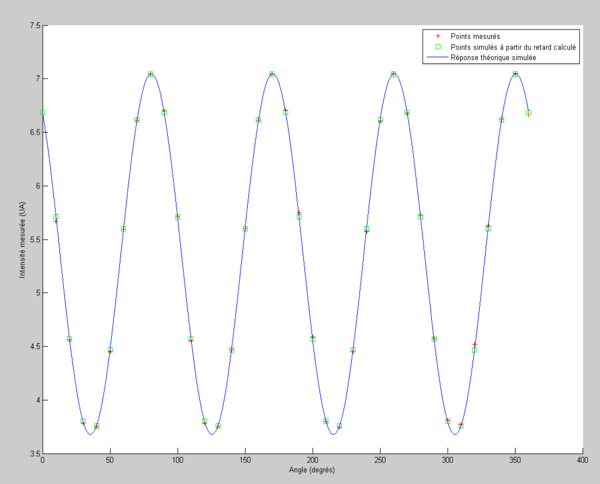

Dessin 10: Détermination du retard de la quart d'onde d'entrée

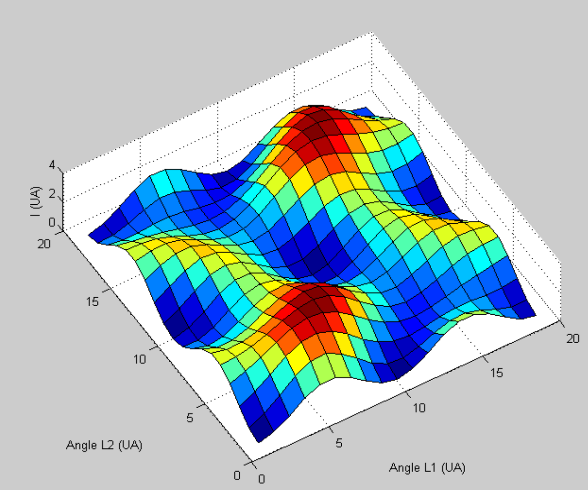

Dessin 12: Mesure de la matrice du vide pour calibration

3.2 Validation expérimentale du capteur piezo-optique proposé

Une version simplifiée du capteur piezo-optique que nous proposons, décrite dans la partie théorique du travail, a été réalisée et testée sur un banc de mesure de pression hydrostatique. La version pre-industrielle du capteur ne sera pas réalisée puisque cette étape n'est pas comprises dans notre plan de travail, mais ses différentes composantes aient été validées individuellement ce qui est l'une des étapes les plus importantes.

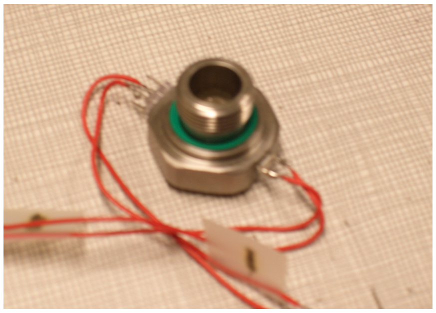

Dessin 14: Capteur piezo-optique de pression

Dessin 13: Banc de test de capteurs : pompe avec manomètre de référence et bloc de test

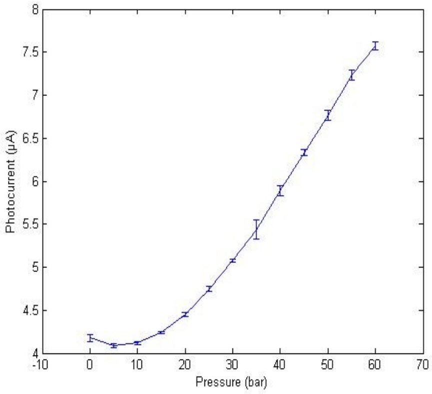

Dessin 15: Courbe de réponse expérimentale avec barres d'erreur

Conclusion

Pour conclure, nous récapitulons les résultats produits au cour de cette étude doctorale menée sous financement CIFRE en partenariat avec la société HYDAC. À partir d'un état de l'art commercial et scientifique des capteurs de pression hydrostatiques ainsi que d'un cahier des charges établi par HYDAC un nouveau concept de transducteur piezo-optique de pression pour les mesures hydrauliques a été proposé. Les principaux avantages de ce capteur sont sa robustesse, sa simplicité de fabrication et son faible coût au vu des performances qu'il peut atteindre. Le capteur proposé est modélisé et analysé en utilisant les outils classiques de l'étude de la polarisation puis sa sensibilité à différentes sources d'erreurs potentielles est prise en compte. D'un point de vue expérimental un polarimètre de Mueller a été réalisé, calibré et testé. Une version simplifiée du capteur de pression hydraulique proposé a été fabriquée est testée. Différentes perspectives s'ouvrent pour poursuivre ce travail. D'un point de vue matériaux il serait important d'étudier l'effet du vieillissement du milieu transparent sur les performances du capteur, ainsi que de compenser plus avant les effets des variations de température afin d'améliorer la précision intrinsèque du capteur. L'étude de ces points pourrait amener à l'élaboration d'un processus d'auto-calibration du capteur. Un autre facteur clé pour l'amélioration de la précision atteignable serait le développement plus avant du dispositif de détection de la polarisation tout en maintenant un coût et une complexité du capteur minimale.

ANNEX

Requirement Specification Pressure Sensor 100 bar

1. EMC Requirements

No.	tests required?		Brief description
	yes	no	
1.1		**X**	Immunity to voltage spikes on power supply lines
1.2	**X**		Immunity to voltage spikes on signal, data and control lines
1.3		**X**	Emission of spikes on supply, signal, data and control lines
1.4		**X**	Measurement of conducted interference from electromechanical components
1.5		**X**	Measurement of conducted interference from electronic components
1.6		**X**	Measurement of transient emissions with the TEM cell
1.7		**X**	Measurement of transient emissions with the stripline
1.8		**X**	Measurement of transient emissions with the current probe.
1.9	**X**		Immunity of interference with the TEM cell / stripline Extended requirements for this component: Immunity to interference 100 V/m
1.10	**X**		Immunity to Interference with the stripline from 1 to 1000 MHz Extended requirements for this component: Immunity to interference: till 100 V/m Non-destructive range: till 200 V/m
1.11		**X**	Immunity to interference according to the BCI method
1.12		**X**	Immunity to interference in the anechoic chamber for system setups
1.14	**X**		Immunity to interference in the mobile radio areas
1.15	**X**		Immunity to electrostatic discharge (ESD)
1.16		**X**	Immunity of components to ripple of the vehicle electrical system
1.17		**X**	Progression of low-frequency attenuation for audio systems
1.18		**X**	Clocked voltages and currents on the vehicle electrical system
1.19	**X**		Ground offset between ground-pin and metal housing

2. Electrical Requirements

		Symbol	**Min.**	**Typ.**	**Max.**	**Unit**

2.1	**temperatures**					
2.1.1	Room temperature	ϑ_R	18	23	28	° C
2.1.2	Operation temperature	ϑ_{OP}	-40		135	° C
2.2	**Pressure ranges**		0		?	
2.2.1	**Measuring range**	p_R	0		100	bar
2.2.2	Non-destructive range	p_{nd}	150 (or 1,5x of p_{MAX})			bar
2.2.3	burst pressure	p_{burst}	600 (or 6x of p_{Max})			bar
2.2.4.	**Dynamic pressure test**	p_{dyn}	10^7 pulse* (2 Hz) at 150 bar ±5%			
2.3	**Power supply**					
2.3.1	Operation supply voltage	U_S	4.7	5	5.3	V
2.3.2	Non-destructive supply voltage max. 10 min.	U_{ndS}	-14		16	V
2.3.3	Supply current at U_S	I_S			10	mA
2.3.4	supply current at U_{ndS} beyond U_S	I_{ndS}			18	mA

2.4 **Output signal** The behavior of the output signal is ratiometric to supply voltage.

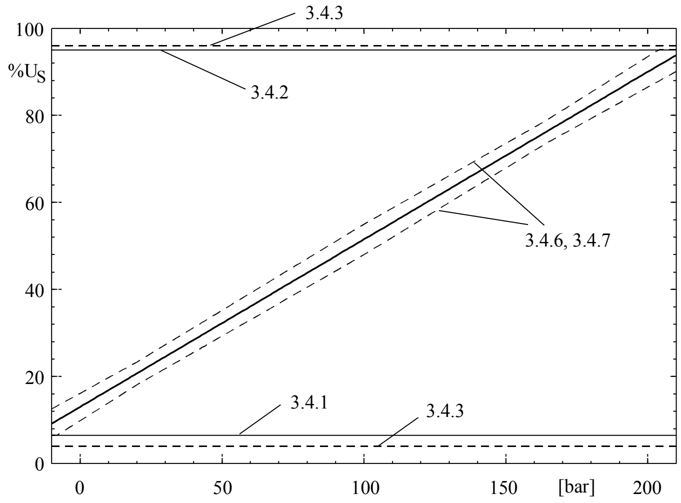

2.4.1	low saturation voltage	$U_{O\,lo}$	6.5			%U_S
2.4.2	high saturation voltage	$U_{O\,hi}$			95,0	%U_S
2.4.3	Output voltage, if failure mode	$U_{O\,fail}$	96,0		4,0	%U_S
2.4.4	Offsetvoltage					

2.4.4.1	- as-delivered condition	$U_{off(del)}$	10.5	13,0	15.5	$\%U_S$
2.4.4.2	- total	$U_{off(tot)}$	10,0	13,0	16,0	$\%U_S$
2.4.4.3	- depends on ϑ_{OP}	$u_{off(\vartheta OP)}$	0.0016	0.0073	0.013	$\%U_S/°C$
2.4.4.4	Rate of change of offset	v_{off}			±1,0	$\%U_S$ /s
2.4.5	Sensitivity	u_{sens}	0,355	0,385	0,415	$\%U_S$ /bar
2.4.6	Total error at room temperature 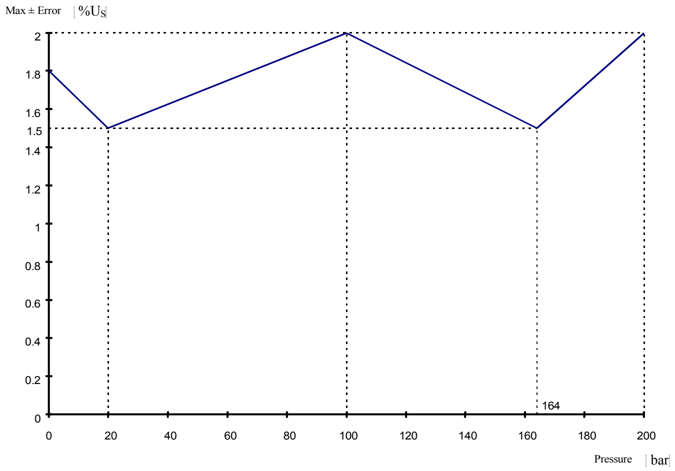					
2.4.7	Temperatureinfluence on the total error 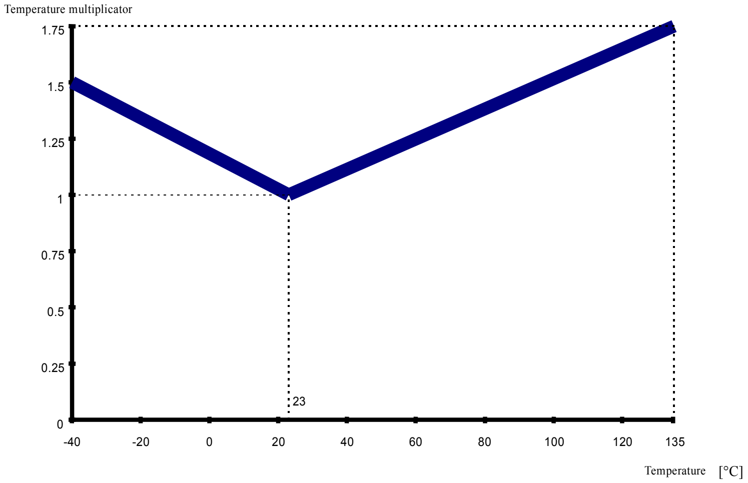					
2.4.8	r.m.s. noise voltage	U_{noise}			10	mV
2.4.9	Output driver current	I_O	0.8		5.0	mA
2.4.10	Output impedance	Z_O	110	120	130	Ω
2.4.11	Nominal load resistor to ground	R_{LN}	47.5	50	52.5	kΩ

2.4.12	Nominal load capacitance	C_{LN}	0.5	1	1.5	nF
2.4.13	Max. load capacitance	$C_{L\,max}$			20	nF
2.5	**Dynamics**					
2.5.1	Nominal frequency	f_N	0	0	0	Hz
2.5.2	Upper cut-off frequency	f_{hi}	25			Hz
2.5.3	Response time	$t_{response}$			10	ms
2.5.4	Resonant frequency	f_{res}	800			Hz
2.5.5	Time until availability	t_{avail}			200	ms
2.5.6	Turn off time	$t_{turnoff}$			20	ms

3. Explanation

	Symbol	Definitions
3.2		**Pressure** **Values are relativpressure**
3.2.1	p_R	**Measuring range** **specification has to be fulfilled**
3.2.2	p_{nd}	Non-destructive range specification has to be fulfilled, beyond p_R no change of the output.
3.2.3	p_{burst}	burst pressure No leakage, sensor does not has to fulfil the specification after returning to p_R
3.3.2	U_{ndS}	Non-destructive supply voltage beyond U_S has to be $U_O = U_{O\,fail}$ After returning to U_S within 10 min the spec has to be fulfilled
3.4	U_O	Output signal No oscillation if the device is defect
3.4.1	$U_{O\,lo}$	low saturation voltage At the working sensor U_O must not fall below $U_{O\,lo}$
3.4.2	$U_{O\,hi}$	high saturation voltage At the working sensor U_O must not exceed $U_{O\,hi}$
3.4.3	$U_{O\,fail}$	Output voltage, if failure mode if failure mode, U_O has to be less than $U_{O\,fail\,max}$ ore more than $U_{O\,fail\,min}$ Failures are for instance: Open supply or ground short between any lines
3.4.4.1	$U_{off(del)}$	Offsetvoltage at 0 bar and ϑ_R as-delivered condition
3.4.4.2	$U_{off(tot)}$	Offsetvoltage at 0 bar over ϑ_{OP} and lifetime
3.4.4.3	$u_{off(\vartheta OP)}$	depends on ϑ_{OP} Influence of the temperature on the offset
3.4.4.4	v_{off}	Drift velocity of offset At changes of the enviromental conditions

3.4.5	u_{sens}	Sensitivity The relation between the change of output value to change of input value including linearity error at 0 Hz
3.4.8	U_{noise}	r.m.s. noise voltage Measured r.m.s. value (root mean square) at frequency range from $f_{lo(typ)}$ to $f_{hi(typ)}$
3.4.9	I_O	Output driver current output long-time short-circuit proof Sensor fulfils specification after short-circuit
3.4.13	$C_{L\ max}$	Max. load capacitance The maximum allowed capacitive load between output and ground without stability problems of the sensor
3.5		Dynamic working range from static input till f_{hi}
3.5.3	$t_{response}$	Response time Maximum time needed to change from 0 % to 90 % or 100 % to 10 % of its final output value after an applied step pressure input from 0 bar to $p_{R\ max}$ or from $p_{R\ max}$ to 0 bar
3.5.4	f_{res}	Resonant frequency Resonant phenomenons may only occur above f_{res}
3.5.5	t_{avail}	Time until availability Time needed after U_N is connected to the sensor until the sensor meets the specification
3.5.6	$t_{turnoff}$	Turn off time Time needed after the supply voltage is reduced from U_N to 0.1V (time ≤ 0.1s) until $U_{off(\vartheta R)}$ has reached 0.25V

4. Price	Aim for production costs (benchmark for competitive pressure sensors 2005)
70.000 Sensors	< 10,25 EUR/Sennsor
130.000 Sensors	< 10,12 EUR/Sennsor
150.000 Sensors	< 9,81 EUR/Sennsor
200.000 Sensors	< 8,30 EUR/Sennsor

* Dynamic Pulse form